Nonlinear resonance and excitability in interconnected systems

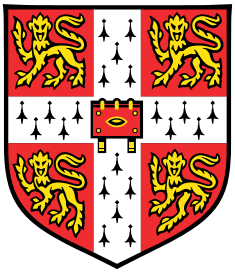

Giuseppe Ilario Cirillo

Supervisor: Prof. R. Sepulchre

Department of Engineering
University of Cambridge

This dissertation is submitted for the degree of
Doctor of Philosophy

Sidney Sussex College

October 2019

Declaration

I hereby declare that except where specific reference is made to the work of others, the contents of this dissertation are original and have not been submitted in whole or in part for consideration for any other degree or qualification in this, or any other university. This dissertation is my own work and contains nothing which is the outcome of work done in collaboration with others, except as specified in the text and Acknowledgements. This dissertation contains fewer than 65,000 words including appendices, bibliography, footnotes, tables and equations and has fewer than 150 figures.

Giuseppe Ilario Cirillo
October 2019

Abstract

Title: Nonlinear resonance and excitability in interconnected systems
Author: Giuseppe Ilario Cirillo

Engineering design amounts to develop components and interconnect them to obtain a desired behaviour. While in the context of equilibrium dynamics there is a well-developed theory that can account for robustness and optimality in this process, we still lack a corresponding methodology for nonequilibrium dynamics and in particular oscillatory behaviours. With the aim of fostering such a theory, this thesis studies two basic interconnections in the contexts of nonlinear resonance and excitability, two phenomena with the potential of encompassing a large number of applications.

The first interconnection is considered in the context of vibration absorption. It corresponds to coupling two Duffing oscillators, the prototypical example of nonlinear resonator. Of primary interest is the frequency response of the system, which quantifies the behaviour in presence of harmonic forces. The analysis focuses on how isolated families of solutions appear and merge with a main one. Using singularity theory it is possible to organise these solutions in the space of parameters and delimit their presence through numerical methods.

The second interconnection studied in this dissertation appears in the context of excitable circuits. Combining a fast excitable system and a slower oscillatory system that share a similar structure naturally leads to bursting. The resulting system has a slow-fast structure that can be leveraged in the analysis. The first step of this analysis is a novel slow-fast model of bistability between a rest state and a spiking attractor. Following this, the analysis moves to the complete interconnection, and in particular on how it can generate different patterns of bursting activity.

Acknowledgements

This thesis is the result of several years of work and it would not have been possible without the involvement and support of a number of people.

First, I would like to express my sincere gratitude to my supervisor, Prof. Rodolphe Sepulchre, for his guidance and help during these years. His ideas have shaped my work, without them this dissertation would not exist.

Before arriving in Cambridge I spent a year at the University of Liège in the Space Structures and Systems Laboratory. I would like to thank all its members for the welcoming and stimulating atmosphere I found. I am specially in debt with Prof. Gaëtan Kerschen, head of the laboratory, and Dr. Giuseppe Habib, a former member. The collaboration with them has continued in the following years and its results form part of this dissertation.

On arrival in Cambridge I found an equivalent welcoming and stimulating atmosphere, thanks the members of the Control Group, past and present. I would like to thank in particular Thiago Burghi, Alessandro Morelli, Luka Ribar and Tomas van Pottelbergh. We arrived in the Control Group at the same time and in these years we have shared fruitful discussions and supported each other in different ways.

I am always in debt with my family: my mother, my father and my brother, and my friends in Italy. They have always supported and encouraged me, no matter the distance.

Last but not least, my years in Cambridge would not have been possible without the financial support of a number of organisations. The scholarship I received in these years was funded by Qulacomm Inc., while the Engineering and Physical Sciences Research Council covered other academic expenses (RG80792). I also received funding from the European Research Council under the Advanced ERC Grant Agreement Switchlet n.670645 for expenses related to conferences as well as my maintenance in the last few months of my PhD.

Table of contents

List of figures

Chapter 1

Motivations and scope of the thesis

From multistability in mechanical and electrical circuits to oscillations in living organisms and chaotic motions in fluids we are surrounded with dynamical systems showing fascinating and complex behaviours that go beyond equilibrium dynamics. The past century has witnessed a large part of research in the applied sciences dedicated to these more complex phenomena. Inspired by this richness and these efforts, there is an ever-increasing interest in exploiting the potential of these phenomena to achieve new horizons with human-made systems.

The efforts undertaken in micro and nanoelectromechanical engineering [64, 78] are an example of this. The extremely small dimensions involved in these systems make the appearance of nonlinear effects readily observed [11], making them a perfect ground to exploit nonequilibrium dynamics. Prominent in this field is the use of resonant systems, leading to the necessity of methodologies for the design of nonlinear resonators.

Another important source of applications lies at the intersection between biology and engineering. Among the many possibilities, close to the themes of this thesis is the interaction between robotics and neuroscience. In these fields there is a growing interest in developing artificial systems that can interact with the nervous system of living organisms or replicate its performance. Two prominent examples of engineering applications in this context are the attempts toward robotic prostheses that can interface with the central nervous system [2], and the developments of agile robots that can move autonomously, with designs often inspired by biological systems [7]. Excitability is a fundamental property of the elements found in neuronal systems, highlighting the need for tools and theories to study and design interconnections between excitable elements.

Despite the broad range of applications and large variety of phenomena, theoretical studies are most often framed in the context of dynamical systems theory. Granted, this encompasses a large variety of tools. Yet, also thanks to the incredible growth of the field in the past century, it is what comes closer to a unifying framework to understand non-equilibrium phenomena of interest in engineering and the applied sciences in general.

But while dynamical systems theory gives the tools to characterise and classify different phenomena, from a design prospective there is also the need of tools and techniques to realise them. Realising a system requires designing its elementary components and interconnecting them to generate new behaviours. A resonant system is obtained by connecting two elements that store energy (elastic and kinetic in a mass-spring-damper system, electrical and magnetic in an RLC circuit); an excitable system is realised from a fast source of positive feedback and a slow source of negative feedback (an instantaneous active element and a slow passive element in an electrical circuit, a fast excitatory current and a slow inhibitory current in a biological membrane). This calls for a theory to predict and design the behaviour of a system starting from its elementary components, an interconnection theory. An interconnection theory that takes into account uncertainties and costs is the essence of systems and control theory.

In the past decades systems theory has made significant progress in understanding questions of stability, robustness and optimality in the context of equilibrium dynamics. Largely, this can be seen as an effort to go from descriptive characterisations of these properties to constructive procedures for the design of stable systems by interconnection [58]. A central motivation of this thesis is that undertaking similar efforts in the context of phenomena away from equilibrium could be extremely advantageous, and lead to theories that can be used in designs that tackle problems like the ones mentioned above in relation to robotics.

The first step in this direction is arguably a theory for oscillations and multistability. Example of recent advances in that context include the efforts to extend differential analysis beyond contractions [26, 27] and the use of describing-function methods to design central pattern generators [48]. Here we complement these efforts from a different viewpoint. Starting from applications in which equilibrium theory is not enough, we study interconnections of elementary systems that lead to nontrivial behaviour, with particular attention to design questions.

To do this we consider two domains that historically have driven the central questions of systems and control theory: mechanical and electrical systems. In these domains we study nonlinear resonance and excitability, given their potential in different applications. While the systems we chose have an importance of their own, we think of them as a fundamental first step towards an interconnection theory: They correspond to interconnections of elementary systems that are well understood in isolation but generate nontrivial behaviours once interconnected.

1.1 Outline and contributions

Before entering in the details of the different interconnections treated in this thesis, the next chapter summarises the fundamental examples of nonlinear resonance and excitability. We consider the Duffing oscillator as the archetype nonlinear resonator. The key characteristic of its frequency response is that the resonant frequency depends on the amplitude of the

input force. In the context of excitability the fundamental example is the FitzHugh-Nagumo model. We use this model to ground our understanding of the action potential generation and the related appearance of relaxation oscillations. The model is closely related to the van der Pol oscillator, the canonical exampled of self-sustained oscillations and an interesting connection between two types of oscillations: quasiharmonic and relaxation oscillations. We think of these systems as the basic building blocks of the interconnections studied in the following chapters: They are the elementary systems that we seek to interconnect to create novel dynamical properties.

Following these preliminaries, chapter 3 studies the interconnection of two Duffing oscillators in the context of vibration absorption. This interconnection models an absorber attached to a main structure. The main focus of the analysis is on family of periodic solutions that are detached from the main branch of the frequency response. These isolated branches are called *detached resonance curves*. Their presence in parameter space can be characterised using singularity theory. Through this characterisation it is possible to delimit the appearance of these solutions in the space of design parameters, a first step towards an improved design of the absorber. Results of this chapter were developed in collaboration with the Space Structures and Systems Lab (S3L) led by Prof. Gaëtan Kerschen and in particular with Dr. Giuseppe Habib. They appeared in [8].

The following chapter moves from mechanical systems to electrical circuits. The main focus is on developing a theory of bursting from the interconnection of excitable elements. Chapter 4 makes a first step studying how to generate a system in which a stable equilibrium (resting state) coexists with a stable fast oscillation (spiking state). The mechanisms underlying this bistability have only recently been approached in the context of slow-fast systems, despite its importance in several examples of bursting oscillations, a topic amply studied in neuronal dynamics. Following up on previous work, the chapter studies a classical model of excitability augmented with a source of slow of positive feedback, closely mimicking how this structure is realised in biological membranes. Results of this chapter were presented at the SIAM Conference on Applications of Dynamical Systems (DS19) and have been submitted for publication (a preprint is available [9]).

The final contribution of this thesis is in chapter 5. Interconnecting two of the elementary systems of chapter 2 provides a design methodology for bursting systems. After recalling how a similar structure is found in different published models of neuronal activity, the chapter focuses on how modulating properties of a subsystem produces different patterns usually studied in isolation. In our view this is a simple instance of the more important question of how a system can be modulated between different behaviours, a topic of growing importance in the neurophysiology community. A preliminary version of the same ideas was used to study hyperpolarisation-induced bursting, a poster summarising the results was presented at the 4th International Conference on Mathematical Neuroscience (ICMNS).

Chapter 2

Preliminaries: nonlinear resonance and excitability

In this preliminary chapter we revisit the canonical mathematical models of nonlinear resonance and excitability: the Duffing oscillator and the FitzHugh-Nagumo model. We see these as the elementary systems that appear in these contexts, making them the natural starting point to realise more complex behaviours and phenomena. They also represent two distinct types of oscillations: quasiharmonic and relaxation oscillations.

The first class of oscillations appears in weakly-damped weakly-nonlinear systems. We consider the Duffing oscillator in this regime.

The second class of oscillations appears in the context of strongly dissipative systems with time-scale separation, the key property used in the analysis of the FitzHugh-Nagumo model.

These two types of oscillations appear as distinct limits of the van der Pol oscillator, probably the best-known model of self-sustained oscillations. We review its structure and the corresponding limits in passing from one type of oscillation to the other.

Throughout the chapter we also give examples of concrete realisations of these elementary systems, whose development often went hand in hand with the theoretical analyses.

2.1 Nonlinear resonance

Resonant systems are characterised by high-amplitude response to periodic input in a selected range of frequencies. The simplest and most well-known example of resonant system is the weakly-damped harmonic oscillator

$$\ddot{y} + 2\zeta\nu\dot{y} + \nu^2 y = u \tag{2.1}$$

where ν is the natural frequency and ζ the damping ratio. It is not restrictive to assume $\nu = 1$, since this is obtained using the dimensionless time $\tau = \nu t$. This equation admits

realisations in many domains of interest in engineering, two common examples being a mass-spring-damper system and an RLC circuit.

Restricting our attention to harmonic inputs $u = f\cos(\omega t)$ yields

$$\ddot{y} + 2\zeta\dot{y} + y = f\cos(\omega t) \tag{2.2}$$

The easiest way to study this equation is to use linearity to reduce to the case $u = f\exp(\mathrm{j}\omega t)$. Using the ansatz $y = w\exp(\mathrm{j}\omega t)$ yields

$$w(-\omega^2 + 2\zeta\mathrm{j}\omega + 1)\exp(\mathrm{j}\omega t) = f\exp(\mathrm{j}\omega t) \tag{2.3}$$

which leads to the frequency response

$$\frac{w}{f} = \frac{1}{(\mathrm{j}\omega)^2 + 2\zeta\mathrm{j}\omega + 1} \tag{2.4}$$

For small ζ the amplitude of the frequency response (2.4) has a peak near the natural frequency $\nu = 1$. As ζ tends to 0 the value of this peak tends to infinity and its position moves closer to 1, the natural frequency.

The reason while the simple harmonic oscillator is so prominent in oscillatory phenomena is twofold. On the one hand, every linear system can be decomposed in independent modes with the model above corresponding to one resonant mode. On the other hand, considering a small-oscillation regime, a resonant system can be linearised, leading to a description in terms of damped harmonic oscillators.

Although this line of thinking has been the essence of vibration mechanics for a long time, applications in which the nonlinear regime is of interest are becoming more prominent, ranging from nano/microelectromechanical systems [64] to structural dynamics [95]. The entry point for most of them is the study of the Duffing oscillator, which often serves as the nonlinear counterpart of the harmonic oscillator.

2.1.1 The Duffing oscillator

Examples of nonlinear oscillations and resonances have been studied since the early 1800s [60]. Two notable examples appear in the work of Helmholtz [99] and Rayleigh [89]. However, it is George Duffing who is often accredited [60] with the first systematic study of the response of a nonlinear system to periodic inputs. Motivated by applications in mechanical engineering Duffing studied the effect of adding a nonlinear spring to a damped harmonic oscillator in his monograph *Forced oscillations with variable natural frequency and their technical significance* [20]. While he considered both quadratic and cubic springs, his name is most

often associated with the latter case

$$\ddot{y} + 2\zeta\dot{y} + y + \alpha y^3 = u \tag{2.5}$$

This, thanks also to Duffing's work, has become the prototypical example of nonlinear resonant system.

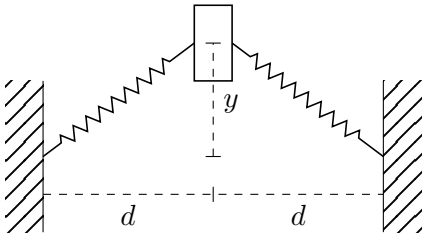

Figure 2.1 Simple realisation of a Duffing oscillator.

As the harmonic oscillator can be used to model several physical systems, the same is true for the Duffing oscillator; the reason is similar, while linearising a nonlinear characteristic leads to a linear spring, retaining few more terms of a Taylor expansion often leads to an equation of the form (2.5). A simple example is the system shown in figure 2.1, consisting of a mass constrained to a line with two (linear) springs connected transversally. Assuming springs of same constant k and rest length d_0, and using y and d defined in figure 2.1, the force developed by each spring is

$$F_s = k\left(\sqrt{d^2 + y^2} - d_0\right) \tag{2.6}$$

The resulting force along the free direction is

$$F = 2\frac{y}{\sqrt{d^2 + y^2}}F_s = 2ky\left(1 - \frac{d_0}{d^2 + y^2}\right) \tag{2.7}$$

If $d > d_0$ and the displacement y is not too large, a third order Taylor expansions of (2.7) leads to a cubic approximation of the force as in (2.5).

While in the example above the coefficient of the nonlinearity is positive, also the case of negative constant can be of interest. This case is rarely meaningful for all values of y, since it leads to unbounded trajectories. However, when the dynamics is restricted to a neighbourhood of the origin it can be used to approximate other systems. A standard example is the mathematical pendulum: A third-order Taylor expansion of its restoring force leads to (2.5) with α negative.

Although not studied in this dissertation, another popular choice of parameters corresponds to a double-well potential. This is obtained using a negative linear spring with a positive

cubic one. Qualitatively, its behaviour is similar to the one of the system in figure 2.1 when $d_0 > d$, making the origin unstable.

In [5] several other examples of physical realisations are reported. It is of particular interest to mention how those related to structural dynamics are derived. They are obtained considering nonlinear effects during the vibration of beams and cables. Starting from the continuous description of theses structures in terms of partial differential equations, the model is approximated with a discrete system by projecting the motion onto a finite number of linear modes. If only one mode is sufficient for the problem at hand, the resulting system has one degree of freedom. Often, this can be approximated using (2.5). The same line of reasoning leads to model two structures as two simple Duffing oscillators, an approach that motivates the use of two Duffing oscillators to model a main structure and a vibration absorber in the next chapter.

2.1.2 Frequency response of a Duffing oscillator

As for the harmonic oscillator, we will be interested in the response of (2.5) to harmonic forcing $u = f\cos(\omega t)$

$$\ddot{y} + 2\zeta\dot{y} + y + \alpha y^3 = f\cos(\omega t) = \frac{f}{2}(\exp(\mathrm{j}\omega t) + \exp(-\mathrm{j}\omega t)) \tag{2.8}$$

Solutions of this equation are usually studied using perturbation techniques. These require the introduction of a small parameter ε used to obtain approximate solutions. In the case of (2.8) the model is mostly studied in the weakly-nonlinear regime, which fits well with the idea that the cubic restoring force comes from a Taylor expansion. This regime arises from imposing small force and small nonlinearity: $f = \varepsilon f'$, $\alpha = \varepsilon\alpha'$. It is also common to assume small damping, $\zeta = \varepsilon\zeta'$, given that this is necessary to observe resonant behaviour. This is the canonical starting point for perturbation techniques applied to the Duffing oscillator. Among them, averaging has received particular attention [85].

In this thesis we are interested in frequency responses of resonant systems. A simple way to approximate them is the harmonic-balance method. In terms of steady-state solutions this leads to similar results as perturbation techniques [42] but usually amounts to less effort. In its simplest form harmonic balance corresponds to assume

$$y = w\exp(\mathrm{j}\omega t) + \overline{w}\exp(-\mathrm{j}\omega t) \tag{2.9}$$

Inserting this expression in the equation of motion (2.5) and considering the coefficient of the first harmonics leads to

$$\begin{aligned} 3a^3\alpha - a\omega^2 + a &= \frac{f}{2}\cos(\phi) \\ 2\zeta a\omega &= -\frac{f}{2}\sin(\phi) \end{aligned} \tag{2.10}$$

where $w = a\exp(\mathrm{j}\phi)$. This pair of equations can be solved numerically to obtain the frequency responses in figure 2.2.

In contrast to the linear case, the frequency response depends on the input amplitude f. Moreover, the frequency at which the response reaches maximum amplitude is not fixed and multiple solutions can coexist for the same value of ω. Depending on the value of α we can distinguish two cases. If $\alpha < 0$ the spring has a softening characteristic, since it becomes

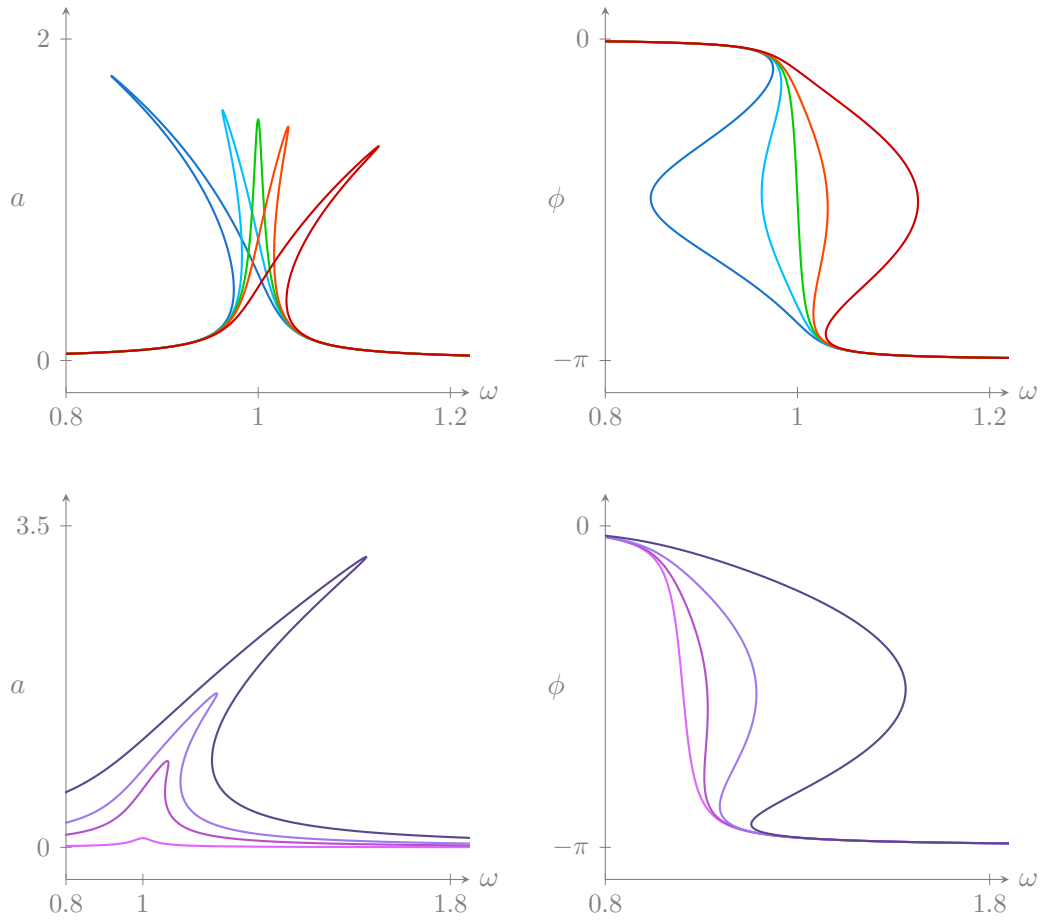

Figure 2.2 Frequency responses of a Duffing oscillator (first-order approximations). Left: amplitude. Right: phase. Top: $f = .03$, $c = .01$, $\alpha = -.03$, $\alpha = -.01$, $\alpha = 0$, $\alpha = .01$, $\alpha = .05$. Bottom: $\alpha = .05$, $c = .05$, $f = .01$, $f = .1$, $f = .2$, $f = .5$.

softer as the displacement increases (the ratio force/displacement decreases). In this case high-amplitude motion and multistability are found for frequencies that are lower than $\omega = 1$, the natural frequency of the linearised system. Similarly, the case $\alpha > 0$ is called hardening, with high-amplitude oscillations and multistability found at higher frequency. As one would expect, and as shown in figure 2.2, these effects increase with the amplitude of forcing.

Reducing (2.10) to a single equation for the amplitude a it is possible to obtain a qualitative understanding of the frequency response of the Duffing oscillator. This reduction can be achieved squaring and summing the two equations. Substituting $A = a^2$, $F = f^2$ and $\Omega = \omega^2$ in the result yields

$$9A^3\alpha^2 + A^2\left(-6\Omega\alpha + 6\alpha\right) + A\left(\Omega^2 + \Omega c^2 - 2\Omega + 1\right) = \frac{F}{2} \tag{2.11}$$

This scalar equation can be studied with the methods presented in the next chapter. The main outcome of this analysis is a classification of the behaviour in two distinct regimes: One in which the frequency response is monovalued, the other in which multiple responses for the same frequency are possible. A similar analysis was developed by Holmes and Rand [47], who characterised in a similar way the parameter space of (2.5) using averaging and catastrophe theory.

2.2 Intermezzo: The van der Pol oscillator

As the Duffing oscillator is the canonical example of nonlinear resonance, the van der Pol oscillator is the canonical example of self-sustained oscillations. In the context of this thesis it also represents a continuous bridge between quasiharmonic oscillations studied in mechanics and relaxation oscillations studied in neurodynamics.

The Duffing oscillator does not exhibit oscillatory solutions in absence of periodic forcing. In contrast, self-sustained oscillations are observed in the van der Pol oscillator thanks to a

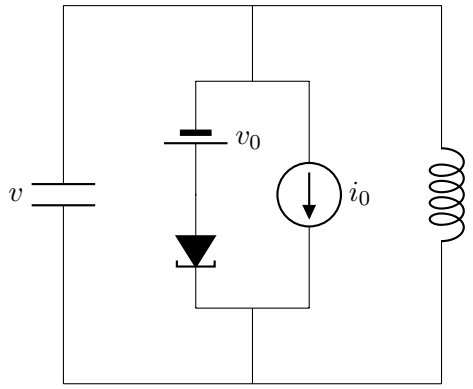

Figure 2.3 Simple realisation of a van der Pol oscillator.

nonlinear damping term that can deliver energy to the system

$$\ddot{y} + \mu(y^2 - 1)\dot{y} + y = u \tag{2.12}$$

Van der Pol introduced this equation while studying circuits that contain triodes. Since the appearance of semiconductor technology it is common to realise this oscillator using a tunnel diode instead, as shown in figure 2.3 (more recent and reliable realisations are based on operational amplifiers).

This oscillator can exhibit both quasiharmonic oscillations and relaxation oscillations, as already noted by van der Pol when he coined the latter term [96]. The parameter μ controls the type of oscillations.

The case $\mu \ll 1$ corresponds to quasiharmonic oscillations. Since for $\mu = 0$ one recovers the harmonic oscillator, it is natural to see trajectories of (2.12) as perturbations of the cycles obtained at $\mu = 0$, as done for example using averaging techniques [85] (if only the limit cycle is of interest harmonic balance is a convenient alternative).

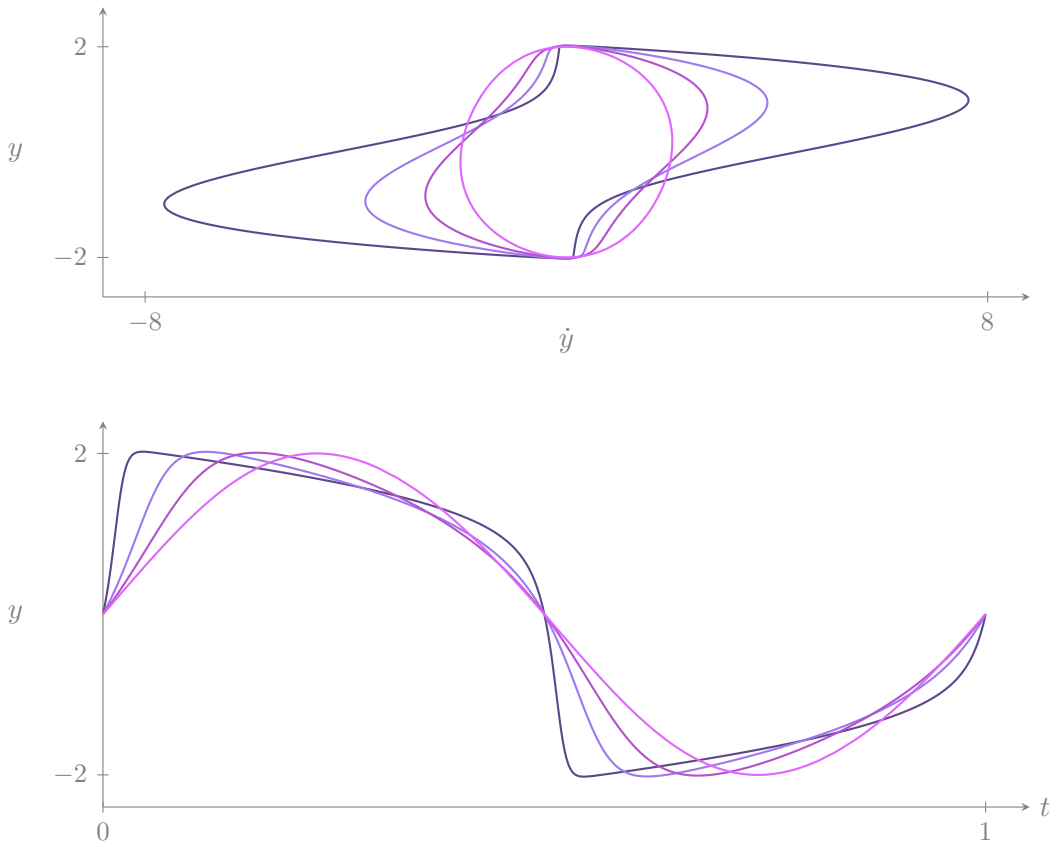

Figure 2.4 Different limit cycles in the van der Pol oscillator (— $\mu = .1$, — $\mu = 1$, — $\mu = 2$, — $\mu = 5$)). Top: phase space $\dot{y}$-y. Bottom: time trajectories (period normalised between 0 and 1).

Relaxation oscillations will be described in more detail in the next section. They are obtained in (2.12) when $\mu \gg 1$. In this case it is convenient to rewrite the equations using the so-called Liénard transform

$$v = y \qquad w = y - \frac{y^3}{3} - \frac{\dot{y}}{\mu} \tag{2.13}$$

which leads to the state-space form

$$\begin{aligned} \dot{v} &= \mu(v - \frac{v^3}{3} - w) \\ \dot{w} &= (v - u)/\mu \end{aligned} \tag{2.14}$$

The substitution of v for y in (2.13) leads to the canonical labelling of the variables used for the FitzHugh-Nagumo model and reminds us that in most realisations y corresponds to a voltage. Indeed, deriving the equation directly from the circuit in figure 2.3 leads to a from similar to (2.14), where v is the voltage across the capacitor and w the current through the inductor.

Periodic trajectories obtained for different values of μ are shown in figure 2.4. For small μ the trajectory describes (nearly) a circle in the $\dot{y}$-y plane, with the time trace being almost sinusoidal. As μ increases the trajectory deviates from a circle and alternates between fast and slow phases. The system shows slow-fast behaviour.

2.3 Excitability

Most biological cells maintain a difference of electrical potential across their membrane. When a small current is injected through the membrane, the cell responds passively, with a small voltage deviation. But beyond a certain threshold, some cells respond with a large voltage excursion, called an action potential or spike. This excursion is often stereotyped and independent from the details of the applied current. Cells with this property are called excitable. Prominent examples in this category are neurons and muscle cells.

As already noted by van der Pol [97], electrical properties of excitable membranes share similarities with his model of self-sustained oscillations, especially in the case of large μ. Indeed, FitzHugh [25] analysed a modified version of the van der Pol oscillator with the objective to give a qualitative description of the action potential and a mathematical model of excitability. This model is now known as the FitzHugh-Nagumo model.

FitzHugh's work was based on the model developed by Hodgkin and Huxley [46] during their seminal work on the giant axon of the squid. In that work they produced the first biophysical description of the action potential and laid the foundations for the formalism that we now use to model excitable membranes.

In the following we start from the simplified description of the action potential due to FitzHugh and later review the formalism developed by Hodgkin and Huxley.

2.3.1 The FitzHugh-Nagumo model

The model studied by FitzHugh [25] and implemented by Nagumo and co-workers [71] corresponds to a modified version of the van der Pol equation* (also known as Bonhoeffer-van der Pol model)

$$\begin{aligned} \varepsilon \dot{v} &= i - \frac{v^3}{3} + v - w \\ \dot{w} &= v - aw \end{aligned} \tag{2.15}$$

In these equations a is assumed positive and such that the two curves $i = \frac{v^3}{3} + v - w$ and $v - aw = 0$ have a unique intersection for all values of i.

Following the implementation of the van der Pol oscillator, it is not hard to give a circuit implementation for these equations. The dynamics of v

$$\varepsilon \dot{v} + \frac{v^3}{3} - v + w = i \tag{2.16}$$

corresponds to a current balance: An externally applied current (i) is equal to the sum of the current through a capacitor ($\varepsilon \dot{v}$), the current through a passive branch (w) and the current through an element with a cubic i-v characteristic ($v^3/3 - v$). This latter element is realised in figure 2.3 with a tunnel diode, a battery and a current source. The dynamics of w is a balance of voltages on the corresponding branch

$$\dot{w} + aw = v \tag{2.17}$$

The total voltage (v) is the sum of the voltages across an inductor ($\dot{w}$) and a resistor (aw) connected in series. This last element is not present in the van der Pol oscillator shown in figure 2.3.

Compared to the van der Pol equation of the previous section also the external input is different. In (2.15) the input is an externally applied current, similarly to what happens in excitable cells. In the work of van der Pol, the triode circuit was instead driven by an external electromagnetic field.

The key to analyse (2.15) is to exploit its slow-fast structure determined by the small constant ε. We postpone a more complete introduction to this theory to chapter 4 and limit ourselves to a qualitative description here.

*FitzHugh in his work used a different sign convention for w and had an additional term in the dynamics of w, these differences do not alter the dynamics of v.

Due to time-scale separation at most points on the v-w plane we have $\dot{v} \gg \dot{w}$, so that the dynamics is dominated by the fast equation

$$\varepsilon \dot{v} = i - \frac{v^3}{3} + v - w \tag{2.18}$$

with w (nearly) constant. This is true until a trajectory arrives to a point that makes the right hand side of (2.18) of order ε, which happens in an ε-neighbourhood of the curve

$$w = i - v^3 + v \tag{2.19}$$

This equation corresponds to fixed point of the fast dynamics (2.18) and defines the so-called critical manifold of the system.

The fast dynamics (2.18) is shown on the left of figure 2.5. Depending on the value of w and i there are one, two or three fixed points. Correspondingly, the critical manifold is divided in three branches, separated by the two fold points at $v = \pm 1$. The external branches correspond to stable fixed points and are attractive, whereas the middle branch corresponds to unstable fixed points and is repulsive.

The right part of the same figure shows the phase plane with the trajectory of one action potential. The dynamics away from an ε-neighbourhood of the critical manifold is dominated by the fast dynamics (2.18) and trajectories quickly converge towards one of the two stable branches. Once in an ε-neighbourhood of one of these branches the trajectory remains close

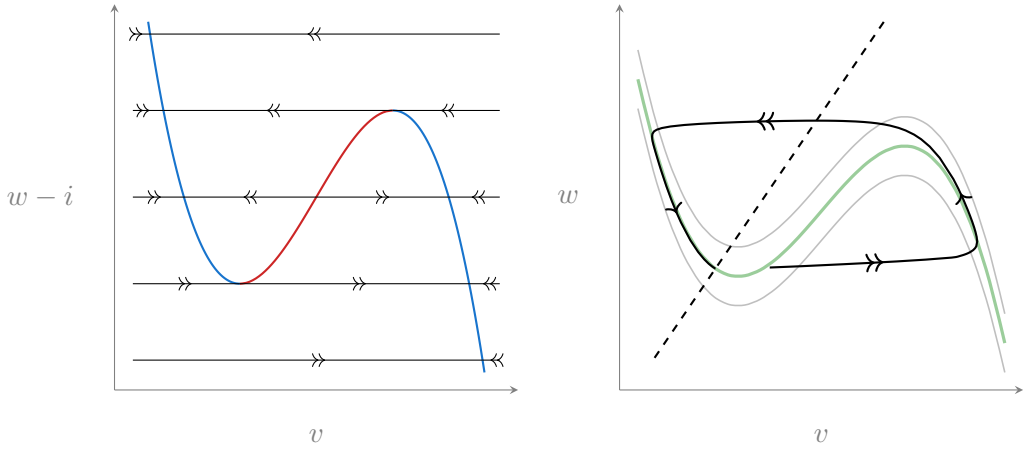

Figure 2.5 Dynamics of the FitzHugh-Nagumo model. Left: bistable fast dynamics, two branches of stable fixed points (——) are separated by a branch of unstable ones (——). Right: geometric construction of the action potential, near the critical manifold (——) trajectories follow the slow dynamics (2.20), determined by the slow nullcline (- - -); away from an ε-neighbourhood of the critical manifolds trajectories follows the fast dynamics (2.18). The trajectory shown (——) corresponds to an action potential, fast parts are marked by a double arrow, slow parts by a single one.

to the critical manifold. The behaviour near the critical manifold is slow and approximately dictated by the slow dynamics

$$\begin{aligned} 0 &= i - v^3 + v - w \\ \dot{w} &= v - aw \end{aligned} \tag{2.20}$$

The variable w increases along a trajectory if $v - aw > 0$, corresponding to points below the w-nullcline $v - aw = 0$, while it decreases in the opposite case. The only point on the critical manifold at which $v - aw = 0$ corresponds to a fixed point of the system.

There are two possibilities near a stable branch of the critical manifold*. If no fixed point is present on that branch the trajectory slides along the manifold until it reaches a fold. In a neighbourhood of a fold the slow drift leads outside the ε-neighbourhood of the critical manifold where the dynamics follows the slow system (2.20), and the trajectory is attracted by the other stable branch following the fast dynamics. If there is a fixed point on a stable branch then it is attractive for the slow dynamics (2.20), and trajectories close to that branch asymptotically converge to the stable fixed point.

Geometrically, a single action potential corresponds to a trajectory that goes once around the critical manifold with alternating fast and slow parts as shown in figure 2.5. For i low enough there is one fixed point on the stable branch at lower voltages, corresponding to a rest state. Applying a short impulse of current increases the value of v; if this brings the system to a point that is attracted by the high-voltage branch of the critical manifold then the trajectory generates an action potential, i.e. it follows a path similar to the one in figure 2.5. Two properties are easily derived from this construction: The shape of the action potential is largely independent of the input and it is determined by the geometry of the critical manifold. The action potential is all or none, once the unstable branch is passed the only possibility is to complete a full action potential†.

Depending on the value of i, the intersection between the critical manifold and the slow nullcline can lie on a stable or unstable branch. In the former case the dynamics tends to the corresponding fixed point, while in the latter the trajectory periodically jumps between the two stable branches of the critical manifold, generating a relaxation oscillation that corresponds to a train of action potentials.

Figure 2.6 illustrates the time trajectories corresponding to both cases. Starting from rest a short impulse generates a spike, while a steady value of applied current induces tonic spiking.

*Ignoring the boundary case of a fixed point on a fold.

†This second property is true only in the singular limit $\varepsilon = 0$. For $\varepsilon > 0$ there is a continuum of trajectories that go from a small cycle around the fixed point to a fully developed action potential. These trajectories are limited to such a small set of initial conditions that for most purposes the action potential can be considered an all-or-none phenomenon.

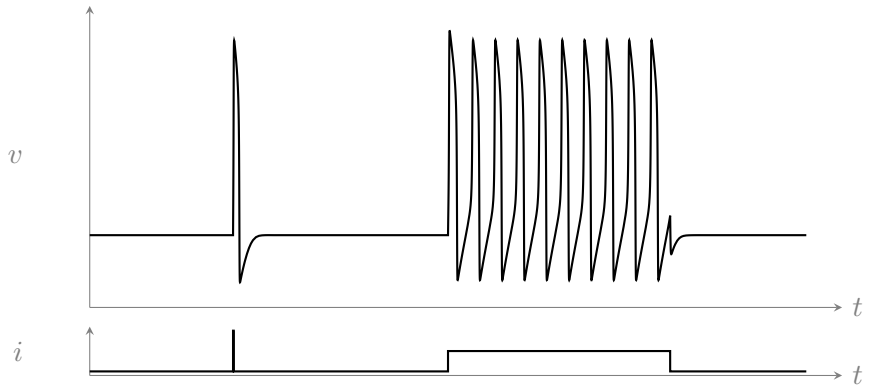

Figure 2.6 Time trajectories of FitzHugh-Nagumo model. A small pulse generates a spike, a steady current generates continuous spiking corresponding to a relaxation oscillation.

The transition between rest and spiking corresponds (in the singular limit $\varepsilon = 0$) to the slow nullcline intersecting the critical manifold at a fold point. This situation leads to canard trajectories, i.e. trajectories that lie on both stable and unstable branches of a critical manifold. For $\varepsilon > 0$ but small enough these trajectories give rise to a canard explosion [61]. Without going into detail, this phenomenon is interesting in the context of neuronal dynamics, and for the FitzHugh-Nagumo model in particular, because it explains the appearance of large oscillations near a Hopf bifurcation. This bifurcation marks the transition between rest and spiking in the FitzHugh-Nagumo model. Due to the presence of a canard explosion, when i is increased in (2.15) and the Hopf bifurcation is crossed, the amplitude of the limit cycle rapidly grows in a small range of values of i, leading to a limit cycle that corresponds to a sequence of fully-formed action potentials. A natural question in this context is how small ε needs to be to observe this type of phenomenon. While the general theory developed in [61] only guarantees its presence if ε is small enough, quantitative results are possible, which depends on geometric properties of the vector field [14].

2.3.2 Hodgkin-Huxley model

The FitzHugh-Nagumo model and its slow-fast analysis form the basis of our understanding of the action potential. However, its relation to the processes underlying electrical activity of biological membranes is only qualitative. The quantitative theory is based on the work of Hodgkin and Huxley on the giant axon of the squid [46]. Through a series of experiments they arrived at a model composed of three currents, corresponding to the three branches of an equivalent circuit as the one shown in figure 2.7.

We now associate these different currents to different types of ion channels, proteins scattered across the membrane that allow the passage of selective ionic species. We will not enter in the biophysical details, which have since been clarified [43, 52], but restrict ourselves to the description as an equivalent circuit.

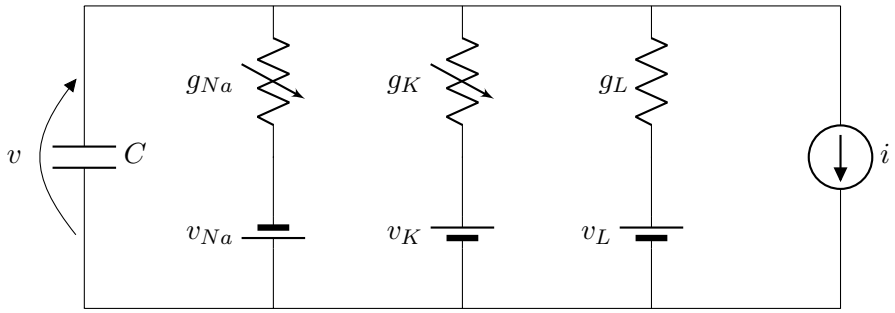

Figure 2.7 Equivalent circuit for the Hodgkin-Huxley model.

Each channel is characterised by a conductance and a reverse potential with the corresponding current given by

$$i_x = g_x(v - v_x) \tag{2.21}$$

The membrane itself acts as a capacitor, resulting in the following balance of currents

$$C\dot{v} + \sum_x i_x = i \tag{2.22}$$

where i is an externally applied current*.

At rest the voltage inside the cell is about 70 mV lower than outside. Following the modern convention the membrane potential is taken as the difference between internal and external potential. Positive currents have the effect of reducing this voltage and correspond to positive ions moving from the inside to the outside of the cell. The reversal potential of a current corresponds to the voltage at which no ion passes through the corresponding channels, the current through the branch is zero. If $v > v_x$ then current x is positive (its effect is to reduce the membrane potential), while if $v < v_x$ it is negative. Most currents found in biological models have a well-defined sign in the range of voltages in which a cell operates. In the Hodgkin-Huxley model one current corresponds to movement of positive ions of sodium (i_{Na}), typically from the outside to the inside of cells (inward current). A second branch of the circuit models a potassium current (i_K), with positive ions going from the inside to the outside (outward current). A third smaller current, termed leak (i_l), carries a mixture of ions, among which the most prominent is chlorine.

One of the key insights of Hodgkin and Huxley was to realise that conductances of ion channels are not necessarily constant but can vary with time and depend on other variables†. In the squid's giant axon sodium and potassium currents have this property, while the leak

*A constant current can also model the presence of ionic pumps that exchange ions between the interior and exterior of a cell in a nearly constant manner (at least in the time-scales of interest).

†In the Hodgkin-Huxley model conductances depend only on the membrane potential. However, examples of conductances depending on other quantities are common in other cells, a prominent example are potassium conductances that depend on calcium concentration.

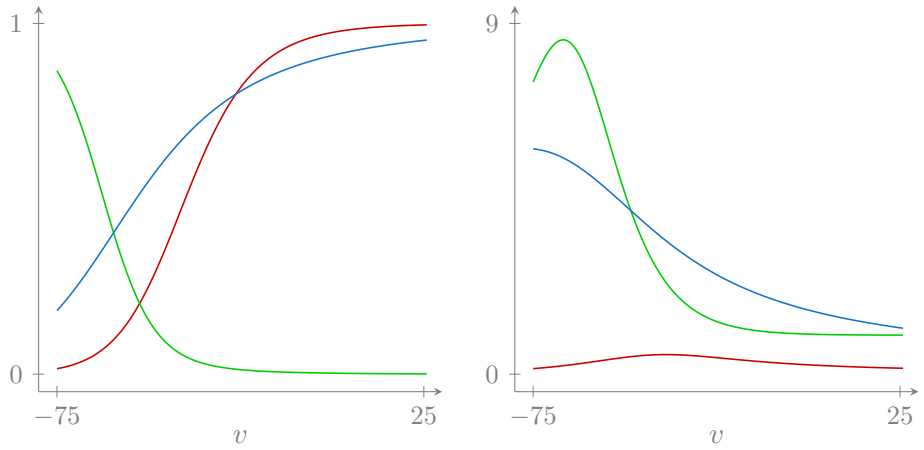

Figure 2.8 Activation functions and time constants Hodgkin-Huxley model (— m, — h, — n).

conductance is constant. What Hodgkin and Huxley noted is that these two conductances depend on the voltage across the membrane. They introduced auxiliary variables to describe this dependence

$$g_{Na} = \bar{g}_{Na} m^3 h \qquad g_K = \bar{g}_K n^4 \tag{2.23}$$

The constants $\bar{g}_{Na}$ and $\bar{g}_K$ are known as maximal conductances, they correspond to the maximum values that a conductance can reach. The variables m, h and n are dynamic variables called gating variables. They take values between zero and one and follow a dynamics of the form

$$\tau_x(v)\dot{x} = x_\infty(v) - x \tag{2.24}$$

The function $x_\infty(v)$ is the steady-state value of the variable x when the voltage is held constant. The function $\tau_x(v)$ is the time constant with which the dynamics converges to this value. Figure 2.8 shows these two functions for the three gating variables of the Hodgkin-Huxley model. Looking at that figure one notices that $m_\infty(v)$ and $n_\infty(v)$ increase as v increases (activation variables), whereas $h_\infty(v)$ decreases (inactivation variable). Since the sodium current tends to increase the membrane voltage, we see that m corresponds to an autocatalytic process: Increasing v increases m that increases i_{Na}, which in turn increases v even more generating a positive feedback loop. On the contrary the other two variables have a restorative effect: When v increases their net effect is to oppose this change, generating a negative feedback loop.

Key to the generation of an action potential is how these two processes are combined. Looking at the time constants in figure 2.8 we see that m is faster than h and n (especially for low voltages, in the so-called subthreshold regime), and comparable to v. This observation,

combined with the fact that during the action potential $h+n \approx .85$, led FitzHugh to study his simplified model. In that simplification the fast positive feedback effect of m is captured by the (instantaneous) linear term in the static i-v characteristic $v^3 - v$; the slow negative feedback of h and n is represented by w. Rinzel [82] went a step further. Fixing m to its steady-state value $m_\infty(v)$ and combining h and n in a unique variable, he obtained a two-dimensional model that approximates the dynamics of the full four-dimensional Hodgkin-Huxley model and has the same geometry of the FitzHugh-Nagumo model.

An alternative approach to reduce the Hodgkin-Huxley model to a planar one was proposed by Abbott and Kepler in [1], and later generalized in [54] to arbitrary conductance-based models. In their work, rather than restricting h and n to a linear relation, they imposed the constrains

$$h \approx h_\infty(u) \qquad n \approx n_\infty(u) \tag{2.25}$$

where u is a new (slow) potential. Starting from the Hodgkin-Huxley model and (2.25) it is possible to derive dynamic equations for v and u, resulting in a planar model. This model is similar, in geometric structure and dynamics, to the ones obtained by FitzHugh and Rinzel.

While all these models aim to study the generation of action potentials in neurons, other works have focused on their behaviour in the so-called subthreshold regime: The range of voltage values in which a neuron does not generate action potentials, but acts as a passive circuit. Mauro et al in [67] noticed how in this regime it is possible to observe decaying oscillations, typical of RLC circuit, despite the absence of inductors in the equivalent circuit. They explained this phenomenon by noting that linearising the ion channels effectively leads to an equivalent inductance (or capacitance), and referred to it as a phenomenological inductance. To distinguish this phenomenon from a truly nonlinear one, membranes in this regimes have been termed *quasi-active* [57].

Chapter 3

Detached resonance curves in the nonlinear tuned vibration absorber

In the previous chapter we described the simplest example of nonlinear resonance: the Duffing oscillator. While in many cases the dynamics of a complicated structure can be confidently modelled by a single degree of freedom there are cases in which this is not possible. In fact, in some applications interaction between distinct degrees of freedom is sought; for example when designing vibration absorbers, additional elements attached to a primary structure to reduce the amplitude of oscillations.

In this chapter we study an example of such design: The nonlinear tuned vibration absorber introduced in [37]. Primary structure and absorber are modelled as two harmonic oscillators with a cubic spring, resulting in two coupled Duffing oscillators. The main phenomenon studied in this chapter is the appearance of detached family of solutions in the frequency response. Since these solutions correspond to high-amplitude vibrations of the primary structure their appearance limits the benefits of using the absorber. Singularity theory organises the geometric structure of these solutions through a degenerate singularity: the asymmetric cusp. Starting from it the presence of these solutions can be studied numerically with respect to design parameters, a first step towards an improved design.

3.1 Introduction

Vibration absorption is one of the classical applications of resonance dating back to the pioneering work of Frahm [28] and Den Hartog [12]. While this classical work, rooted in linear vibration theory, has been successfully used in many applications, the demand for lighter and better-performing structures is pushing these techniques to their limits. The presence of nonlinearities in virtually any real system limits the regimes in which these solutions can be used, leading to conservative designs.

Motivated by this, recent years have seen an increasing interest in mitigating vibrations in presence of nonlinearities. Although considering nonlinear effects allows phenomena without a linear counterpart, such as the appearance of self-sustained oscillations, this chapter focuses on the specific case of oscillations induced by a periodic external force. A first distinction in this context is between absorbers that target a specific range of frequencies and those that have a more broadband character, attenuating multiple resonances at the same time.

A prominent example of this latter case is the nonlinear energy sink (NES) [95], an absorber whose elastic characteristic does not have a linear component. The fundamental property of the NES is its ability to unidirectionally channel vibrational energy from a primary structure, even in the presence of multiple resonances [55]. A limitation of this device is its inability to respond to a wide range of amplitudes: There is a threshold in input energy below which the NES does not induce significant dissipation [95].

An alternative approach is to build upon the linear theory of vibration absorbers and target a wide range of amplitudes in a specific frequency range. This is the philosophy underlying the nonlinear tuned vibration absorber (NLTVA) studied in this chapter. In this design the characteristic of the absorber has the same functional form of the primary structure. In our study we take the latter as a Duffing oscillator with hardening nonlinearity, leading to the interconnection of two Duffing oscillators, as in the first design proposed for the NLTVA [37]. Since then the absorber has been generalised to a primary structure with arbitrary polynomial characteristics [39]. Moreover, similar solutions have also been proposed to mitigate limit cycle oscillations [38] and chatter in machine tools [40].

While the original design showed good performances beyond the linear regime, for high-amplitude forcing detached families of solutions appear in the frequency response. These detached resonance curves (DRCs) are a classical topic of research. They have been observed and studied since the 60s in both mechanical and electrical systems. After a period of relatively low interest they have recently regained momentum, especially in the mechanical engineering community. A comprehensive review of the topic and its history is available in [36].

The presence of such solutions in the context of vibration absorption is detrimental since it limits the range of excitations in which the absorber is effective. Detached resonance curves have been studied in this context by numerical methods [15, 35]. A common theme in those works is that DRCs are associated with degenerate bifurcation. It is therefore natural to appeal to techniques from singularity theory, as developed in [33] (singularity theory with a distinguished parameter) to characterise and study them.

By relying on this theory it is possible to identify an organising centre for the phenomena: A degenerate bifurcation that organises the presence of DRCs in parameter space, the asymmetric cusp. Less degenerate singularity in its unfolding correspond to appearance and merging of DRCs. Moreover, this characterisation can be used to study numerically these curves and delimit their presence in the space of design parameters of the NLTVA.

3.2 Nominal response of the nonlinear tuned vibration absorber

The interconnection studied in this chapter is shown in figure 3.1. It corresponds to a nonlinear tuned vibration absorber (NLTVA) connected to a primary structure as proposed in [37]. The corresponding equations of motion are

$$M\ddot{y} + C\dot{y} + Ky + f_{nl}(y) = gf\cos(\omega t),$$

$$M = \begin{pmatrix} m_1 & 0 \\ 0 & m_2 \end{pmatrix} \quad K = \begin{pmatrix} k_1 + k_2 & -k_2 \\ -k_2 & k_2 \end{pmatrix} \quad C = \begin{pmatrix} c_1 + c_2 & -c_2 \\ -c_2 & c_2 \end{pmatrix} \tag{3.1}$$

$$f_{nl}(y) = \begin{pmatrix} k_{nl1}y_1^3 + k_{nl2}(y_1 - y_2)^3 \\ k_{nl2}(y_2 - y_1)^3 \end{pmatrix} \quad g = \begin{pmatrix} 1 \\ 0 \end{pmatrix}$$

where the components of $y = (y_1,\, y_2)$ are the displacements of the two masses in figure 3.1. For design purposes parameters of the main structure (m_1, k_1, c_1, k_{nl1}) and mass of the absorber (m_2) are assumed fixed, while all other parameters can be chosen to minimise the amplitude of oscillations of the main structure (y_1).

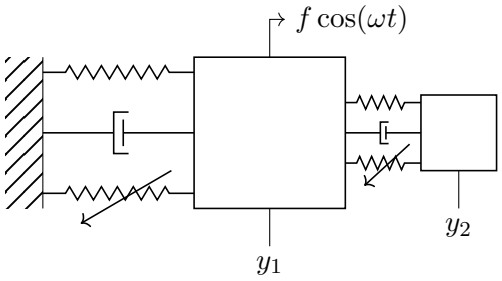

Figure 3.1 Nonlinear tuned vibration absorber attached to a primary structure.

The NLTVA extends the analogous linear design developed by Den Hartog [12], who proposed to realise the absorber so that the frequency response of the interconnected system has two peaks of equal height*. In designing their nonlinear absorber in [37], Habib and coworkers used the same principle, extending Den Hartog's equal-peak method to the nonlinear case. Specifically, they proposed to use for the linear part the values obtained from the linear design and chose the coefficient of the nonlinear spring to enforce the equal-peak condition outside the linear regime. Using a one-harmonic approximation for the frequency response

*The procedure uses the fact that for fixed linear stiffness the frequency response passes through two fixed points. Den Hartog proposed to choose the linear stiffness so that these two fixed points are at the same height and to select the damping coefficient to have horizontal tangent through one of the fixed points. More details can be found in [12].

they obtained the following formulae

$$
\begin{aligned}
k_2 &= \frac{8rk_1\left[16+23r+9r^2+2(2+r)\sqrt{4+3r}\,\right]}{3(1+r)^2(64+80r+27r^2)} \\
c_2 &= \sqrt{\frac{k_2 r(8+9r-4\sqrt{4+3r})}{4(1+r)}} \\
k_{nl2} &= \frac{2r^2 k_{nl1}}{1+4r}
\end{aligned}
\tag{3.2}
$$

where $r = m_2/m_1$ is the mass ratio.

Using dimensionless time and positions (3.1) can be rewritten in the form

$$
\begin{aligned}
\ddot{y}_1 + y_1 + \mu_1\dot{y}_1 + y_1^3 + k(y_1-y_2) + \alpha(y_1-y_2)^3 + \mu_2(\dot{y}_1-\dot{y}_2) &= f\cos(\omega t) \\
r\ddot{y}_2 + k(y_2-y_1) + \alpha(y_2-y_1)^3 + \mu_2(\dot{y}_2-\dot{y}_1) &= 0
\end{aligned}
\tag{3.3}
$$

where y, f and ω now denote dimensionless quantities. Following [37] we consider the nominal values $r = .05$ and $\mu_1 = 0.002$, resulting in the following values for the other parameters

$$
k = 0.0454 \qquad \mu_2 = 0.0128 \qquad \alpha = 0.0042 \tag{3.4}
$$

Figure 3.2 shows different frequency responses of the system obtained varying the forcing amplitude f. These responses, as all the following ones, are shown with axes linearly scaled. They were computed using a shooting algorithm similar to the one used in [72] for the computation of nonlinear normal modes.

The figure makes it clear that for low amplitudes (case a, b and c) the design is effective in that it maintains two peaks of equal height despite the presence of nonlinear effects. However, as the forcing amplitude increases a DRC appears (case d), which eventually merges with the main family of solutions (case e). This DRC corresponds to large-amplitude oscillations that make the absorber less effective in this regime.

This adverse dynamics was investigated using numerical continuation of periodic solutions and their bifurcations in [15]. Here that analysis is complemented with the viewpoint of singularity theory [33]. In the same spirit of [102, 105] for forced Hopf bifurcations, we can identify frequency responses with bifurcation diagrams. The starting point is to reduce the frequency response of (3.1) to a scalar equation*. As in the previous chapter for the Duffing oscillator, this can be achieved using the harmonic-balance method retaining only one harmonic, as detailed in appendix 3.A. The outcome is an equation of the form

$$
g(x, \omega, f, k, \alpha, \mu_2) = 0 \tag{3.5}
$$

*This passage is not necessary since both analytically and numerically the analysis can be carried out through local (Lyapunov-Schmidt) reductions [33, 34]. The availability of a global reduction allows the use of simpler techniques.

whose solutions correspond to periodic motions of (3.1). In the terminology of [33] the relative displacement $x = y_1 - y_2$ is the state variable, the frequency ω is the bifurcation (distinguished) parameter and other parameters correspond to unfolding parameters. In the following we use (3.5) to approximate the frequency response, and verify our results through numerical computations.

Figure 3.2 summarises the type of information obtained applying singularity theory. At low forcing amplitudes the response resembles that of a linear system (case a). Increasing f parts of it become bistable (case b and c) in regions delimited by two fold points. The appearance of these two folds correspond to a degenerate singularity, a hysteresis point (▲). The other types of singularities encountered increasing further the forcing amplitude characterise the presence of a DRC. An isola singularity (●) corresponds to the appearance of an isolated family of solutions (case d), while a simple bifurcation (♦) corresponds to its merging with the main branch of solutions (case e). Thus, singularity theory allows us to identify transitions between qualitatively different frequency responses, with in particular isola and simple bifurcation delimiting the presence of DRCs.

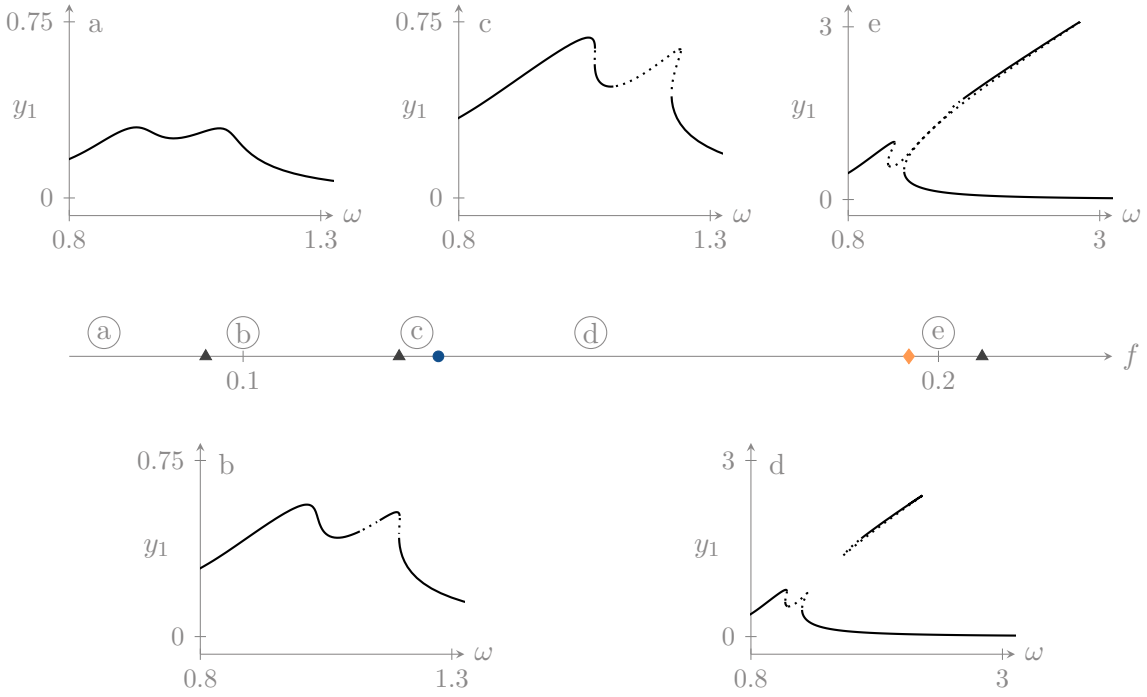

Figure 3.2 Frequency responses of an NLTVA attached to a main structure. Transitions between different diagrams correspond to different singularities (▲ hysteresis, ● isola, ♦ simple bifurcation). Excerpts illustrate the different types of frequency responses, the effect of the last hysteresis is not shown as it is minimal. Continuous lines correspond to stable solutions, dotted lines to unstable solutions. a) $f = 0.05$, b) $f = 0.1$, c) $f = 0.125$, d) $f = 0.15$, e) $f = 0.2$.

We remark that parts of the frequency response in figure 3.2 are unstable due to the presence of quasiperiodic motions. Notably, in cases b and c this motion is the only stable one in an interval of frequencies. These types of solutions were investigated numerically in [15] where further details are available. Unfortunately, they do not directly fit in the framework used in this chapter and will not be considered in the following. Extending the current developments to include these types of solutions is a natural direction for future works.

3.3 Singularities of codimension one and transition set

Before studying the NLTVA and its DRCs in detail, this section and the next one review the basic elements of the theory underlying the developments in this chapter. Further technical details are available in [33].

Singularity theory (with one distinguished parameter) studies bifurcation problems corresponding to a scalar equation*

$$g(x, \omega, \mu) = 0 \tag{3.6}$$

The variable $x \in \mathbb{R}$ is called state variable, $\omega \in \mathbb{R}$ is the bifurcation parameter (the frequency in the present work) and $\mu \in \mathbb{R}^k$ are additional (unfolding) parameters. On a first instance these additional parameters are thought as fixed and the set of solutions of (3.6) in the x-ω space is the bifurcation diagram (corresponding to a frequency response in our case).

Singularities correspond to special points on the bifurcation diagram at which x cannot be expressed as a smooth function of ω. For this to be the case the implicit function theorem has to fail, leading to the conditions at a singularity†

$$g = 0 \qquad \frac{\partial g}{\partial x} = 0 \tag{3.7}$$

A fold (or limit point) is the least degenerate singularity. These points appear when other than (3.7) also the following (nondegeneracy) conditions are verified

$$\frac{\partial g}{\partial \omega} \neq 0 \qquad \frac{\partial^2 g}{\partial x^2} \neq 0 \tag{3.8}$$

*The theory generalises to square systems, in which there are n equations and $x \in \mathbb{R}^n$. We will not need such a generalisation in the following.

†In the following we often write functions without arguments to simplify expressions. In those cases it is understood that all functions are evaluated at the same point. For example (3.7) corresponds to a point (x_0, ω_0) on a bifurcation diagram at which $g(x_0, \omega_0, \mu) = 0$ and $\partial g/\partial x(x_0, \omega_0, \mu) = 0$ (a bifurcation diagram is obtained for μ fixed).

If this is the case the diagram is locally equivalent to one of those obtained from

$$\pm x^2 \pm \omega = 0 \tag{3.9}$$

Equivalence means that a bifurcation problem (3.6) verifying (3.7) and (3.8) can locally be transformed in (3.9) through a change of coordinates. Fixing the class of changes of coordinates allowed defines a way to identify different bifurcation diagrams as qualitatively the same and leads to the key notion of persistence.

3.3.1 Persistent and nonpersistent diagrams

Formally, given two bifurcation problems $g(x,\omega) = 0$ and $f(x,\omega) = 0$, equivalence between the two is based on the relation

$$f(x,\omega) = S(x,\omega)g(\phi_x(x,\omega), \phi_\omega(\omega)) \tag{3.10}$$

where $\Phi(x,\omega) = (\phi_x(x,\omega), \phi_\omega(\omega))$ is a diffeomorphism and $S(x,\omega)$ is a smooth function*. In [33] also $S(x,\omega) > 0$, $\frac{\partial \phi_x}{\partial x} > 0$ and $\frac{d\phi_\omega}{d\omega} > 0$ are required to assure that stability and orientation of the diagram are preserved. Starting from (3.10) it is possible to define two different but related notions of equivalence: global and local. As the name suggests, the first one considers functions which are globally defined, with x and ω varying in a fixed set $U \times L$. In this case (3.10) has to additionally preserve this domain. In the case of local equivalence the functions involved are supposed to be defined only in a neighbourhood of a point, commonly taken as the origin. More precisely, instead of functions *germs* are considered. These are defined as equivalence classes of functions that coincide on a neighbourhood of the origin. The precise definitions are not important here since more technical aspects of the theory are not needed in the following. It is only necessary to distinguish local results from global ones. In the first category fall the classifications of singularities and related perturbations of sections 3.3.2 and 3.4, which cover most of the results used in this chapter. The only exception is the theorem about persistence on a bounded domain at the end of the current section, which uses the global notion of equivalence instead.

The notion of equivalence naturally leads to the notion of persistence: A diagram is said to be persistent if any sufficiently small perturbation results in an equivalent diagram, it is nonpersistent otherwise. Persistent diagrams are robust to small enough perturbations, they are the ones that are commonly observed in numerical simulations and experiments. Referring to the previous section, all the frequency responses shown are persistent. Moreover, all the responses that correspond to values of f between two consecutive singularities in figure 3.2 are equivalent. This gives a more precise idea of how singularity theory can be used to analyse

*In some cases the requirement of smooth equivalence is too stringent and all these functions are only required to be continuous. This happens in more degenerate cases than the ones we study so we do not need this more general notion.

forced oscillations: It provides the tools to divide the parameter space in different zones characterised by a unique (up to equivalence) response. A noteworthy result in this direction is [33, Ch.3 Thm.10.1], which lists all possible sources of nonpersistence for a parametrised family of diagrams $g(x, \omega, \mu)$ where $\mu \in W$, with $W \subset \mathbb{R}^k$ a disk. Specifically, there are three sources of nonpersistence (that can occur in the interior of the domain considered), corresponding to three sets:

i) simple bifurcation and isola points,

$$\mathscr{B} = \left\{ \mu \in \mathbb{R}^k : \exists (x, \omega) \in \mathbb{R} \times \mathbb{R},\ g = \frac{\partial g}{\partial x} = \frac{\partial g}{\partial \omega} = 0 \text{ at } (x, \omega, \mu) \right\}$$

ii) hysteresis points,

$$\mathscr{H} = \left\{ \mu \in \mathbb{R}^k : \exists (x, \omega) \in \mathbb{R} \times \mathbb{R},\ g = \frac{\partial g}{\partial x} = \frac{\partial^2 g}{\partial x^2} = 0 \text{ at } (x, \omega, \mu) \right\}$$

iii) double limit points,

$$\mathscr{D} = \left\{ \mu \in \mathbb{R}^k : \exists (x_1, x_2, \omega) \in \mathbb{R} \times \mathbb{R} \times \mathbb{R},\ x_1 \neq x_2,\ g = \frac{\partial g}{\partial x} = 0 \text{ at } (x_i, \omega, \mu),\ i = 1, 2 \right\}$$

Based on these the *transition set* is defined as $\Sigma = \mathscr{B} \cup \mathscr{H} \cup \mathscr{D}$; diagrams obtained for μ in the same connected component of $W \setminus \Sigma$ are equivalent*.

The conditions defining $\mathscr{H}$ and $\mathscr{B}$ correspond to codimension one singularities, defined in the next section. Crossing one of these sets usually leads to the transitions shown there, apart from exceptional cases in which more degenerate singularities are present. The set $\mathscr{D}$ is partially different from the other two: It corresponds to a nonlocal phenomenon, the occurrence of two limit points for the same value of ω, as shown figure 3.3.

3.3.2 Singularities of codimension one

Having defined the notion of persistence one can ask whether a singular point is persistent, i.e. if it is preserved by small perturbations. As already remarked only limit points are persistent, all other singularities delimit transitions between nonequivalent diagrams. Singularity theory divides singularities based on the notion of equivalence and classifies local perturbations of nonpersistent ones.

Singularities are characterised by two groups of algebraic conditions on the derivatives of (3.6) at a point. *Defining conditions* correspond to derivatives of (3.6) being equal to

*Strictly speaking there are other sources of nonpersistence in a bounded domain $U \times L$. These are related to how the diagram meets the boundary of the domain and are discussed in [33, Ch.3 §10]. These are unlikely to be important in the current setting and therefore ignored.

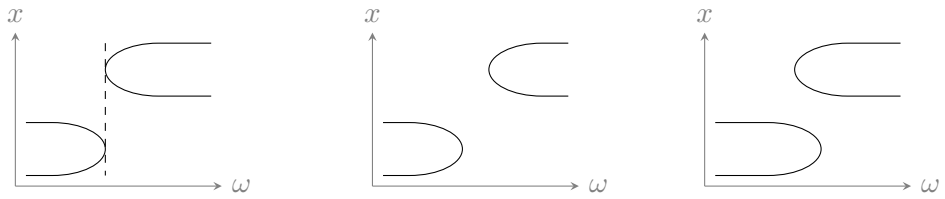

(a) Unperturbed diagram. (b) Perturbed diagrams.

Figure 3.3 The double limit point and its perturbations. At the singularity two fold points on different branches coincide. A perturbation can remove this coincidence and lead to either the two branches being in different ω intervals (left perturbation) or the coexistence of the two branches for some values of ω (right perturbation).

zero and always include (3.7); *nondegeneracy conditions* correspond (in the simpler cases) to derivatives of (3.6) being different from zero.

In section 3.2 we encountered three singularities in figure 3.2. These are the least degenerate after the limit point: hysteresis, isola and simple bifurcation.

The hysteresis is the singularity that underlies the passage from monostability to bistability. It can already be found in the frequency response of the Duffing oscillator at the boundary between these two regimes. Algebraically it is characterised by the defining conditions

$$g = \frac{\partial g}{\partial x} = \frac{\partial^2 g}{\partial x^2} = 0 \tag{3.11}$$

and the nondegeneracy conditions

$$\frac{\partial g}{\partial \omega} \neq 0 \qquad \frac{\partial^3 g}{\partial x^3} \neq 0 \tag{3.12}$$

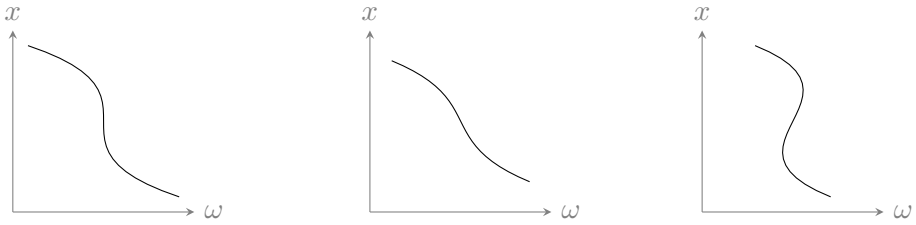

(a) Unperturbed diagram. (b) Perturbed diagrams.

Figure 3.4 The hysteresis and its perturbations. At the singularity the diagram has a point with vertical tangent. A perturbation can remove this point and lead to either a monotonic curve (left perturbation) or the coexistence of mulitple branches separated by folds (right perturbation).

Geometrically it corresponds to points at which the diagram has vertical tangent, as in figure 3.4a. When perturbed, this nonpersistent diagram can only result in one of the two diagrams in figure 3.4b.

The second example of nonpersistent singularity is the isola, characterised by the conditions

$$g = \frac{\partial g}{\partial x} = \frac{\partial g}{\partial \omega} = 0 \qquad \frac{\partial^2 g}{\partial x^2} \neq 0 \qquad \det(d^2 g) > 0 \tag{3.13}$$

where $d^2 g$ is the Hessian matrix of g with respect to x and ω. In figure 3.2 it corresponds to the transition between cases c and d, when a DRC appears. The bifurcation diagram of an isola corresponds to an isolated solution as in figure 3.5a. Perturbing this nonpersistent diagram can only result in two outcomes, no solutions or a closed branch of solutions, both shown in figure 3.5b.

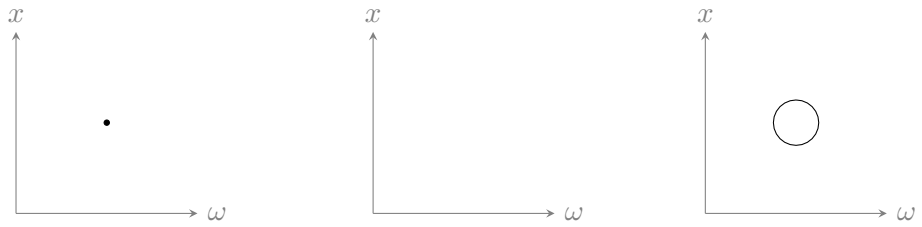

(a) Unperturbed diagram. (b) Perturbed diagrams.

Figure 3.5 The isola and its perturbations. The singularity corresponds to an isolated solution. A perturbation can either remove it, leaving no solutions in a neighbourhood (left perturbation), or lead to a closed curve of solutions (right perturbation).

The third example of nonpersistent singularity is the simple bifurcation point (or transcritical bifurcation). This corresponds to the centre of X-shaped diagrams, as in figure 3.6a, and it is characterised by

$$g = \frac{\partial g}{\partial x} = \frac{\partial g}{\partial \omega} = 0 \qquad \frac{\partial^2 g}{\partial x^2} \neq 0 \qquad \det(d^2 g) < 0 \tag{3.14}$$

The corresponding perturbations are shown in figure 3.6b. Comparing with figure 3.2 one sees that this is the local phenomenon underlying merging of a DRC with a main branch.

The three singularities above account for all the codimension one singularities. The codimension of a singularity can be thought of as a measure of its complexity; it corresponds to the number of defining conditions that characterise it beyond the two conditions (3.7). Using this concept singularities can be classified. All singularities up to codimension three are presented in [33, Ch.4], while in [56] the classification is extended up to codimension seven.

The codimension coincides also with the number of parameters necessary to obtain all the possible perturbations of a given singularity, i.e. the number of parameters in a universal

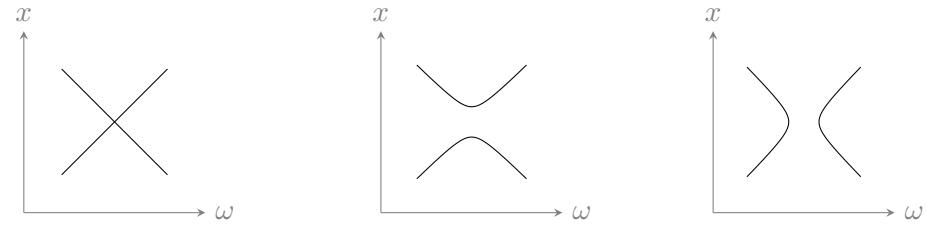

(a) Unperturbed diagram. (b) Perturbed diagrams.

Figure 3.6 The simple bifurcation and its perturbations. At the singularity four branches of solutions meet, forming an X-shaped diagram. A perturbation can break this diagram in two, leaving two branches separated in the x coordinate (left perturbation) or in the ω coordinate (right perturbation).

unfolding. Without entering into details, for which we refer to [33, Ch.3], a universal unfolding is the technical tool used to enumerate the persistent diagrams that can be obtained by small perturbations of a singular one, as in the case of figures 3.4 to 3.6.

3.3.3 Numerical computation

The knowledge of all the possible sources of nonpersistence and their algebraic characterisations can be used as a base for algorithms that explore the parameter space of a system. Methods based on this idea appeared in the context of chemical reactions in [3, 4]. Ideally, one could compute the transition set Σ to obtain a rather complete picture of the possible frequency responses. An approach to do this, along the lines of standard techniques used in this context, starts by reducing the problem of computing a frequency response to the solution of a set of nonlinear equations in x and ω, for example through harmonic balance. Once this is done, it is common to compute solutions using continuation techniques and to use bordering techniques* to detect and continue bifurcations [34]. The same ideas can be used to detect and track singularities [34, Ch.7]. The conditions defining the sets $\mathscr{B}$ and $\mathscr{H}$ correspond to the presence of a singularity, while those defining $\mathscr{D}$ correspond to the occurrence of two fold points for the same value of ω, allowing the computation of the transition set.

In the following we do not need the full power of this machinery. Since we can approximate the frequency response with only one equation, we can use directly their defining conditions to detect and track singularities†.

As a simple illustration of the ideas outlined above figure 3.7 shows the result of continuing the singularities found in figure 3.2 varying μ_2. In this figure crossing one of the three lines

*Bordering is a common technique to construct functions that become zero at bifurcations and singularities. These are known as test functions and can be used in continuation algorithms to identify and track singularities. In several cases these functions can be obtained as components of the solution vector of a linear system, which is formed adding colums and rows (a border) to the jacobian matrix of the system.

†Numerical solution of the equations was carried out in python using the package SciPy [53].

in the hysteresis set $\mathscr{H}$ results in the generation (or merging) of two fold points. More interesting for the following developments are the sets $\mathscr{B}$ and $\mathscr{B}'$. These correspond to simple bifurcations and isola singularities and delimit the parameter values for which a DRC is present.

We mention that some more quantitative aspects of the response are not captured by this analysis. For example, frequency responses corresponding to higher values of μ_2 contain a unique resonance peak, but are equivalent to those found for lower values of μ_2 and f, which contain two peaks. While the fact that the amplitude corresponding to two hysteresis points grows and exceeds the limits considered in figure suggests a strong change, the disappearance of one resonance peak cannot be inferred directly.

3.4 A cusp singularity organises detached resonance curve

A central insight in singularity theory is that more degenerate singularities organise transitions between parameter regions with a lower order of degeneracy. For example, distinct regions containing fold points in figure 3.2 are separated by few codimension-one singularities. The same approach can be repeated with singularities of higher codimension.

This idea can be exploited to analyse detached resonance curves of the NLTVA. Figure 3.2 indicates that presence of a DRC is delimited by an isola (●) and a simple bifurcation (♦). In

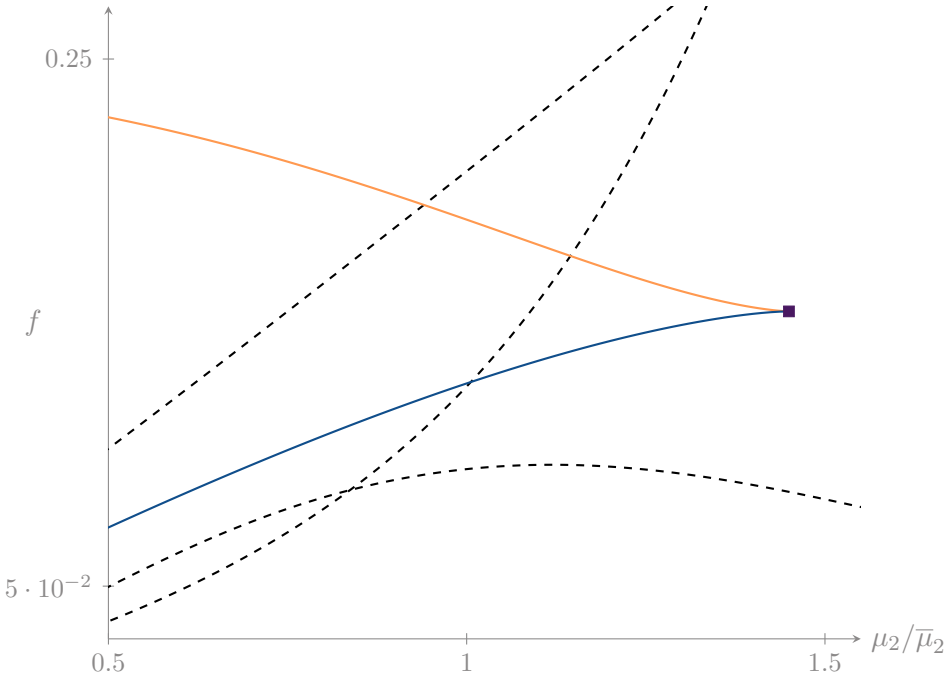

Figure 3.7 Transition set for an NLTVA attached to a Duffing oscillator ($\overline{\mu}_2$ nominal value). The parameter space is divided into different zones by hysteresis, isolas and simple bifurcations (- - - hysteresis ($\mathscr{H}$), — isola ($\mathscr{B}'$), — simple bifurcation ($\mathscr{B}$)).

turn, figure 3.7 reveals that the sets $\mathscr{B}$ and $\mathscr{B}'$ merge for $\mu_2^* = 1.449\overline{\mu}_2$ ($\overline{\mu}_2$ nominal value) and that no DRC exists for $\mu_2 > \mu_2^*$. The value of μ_2^* is in good agreement with the one found in [15] ($\approx 1.44\overline{\mu}_2$) considering that here only one harmonic is retained. This critical point is a singularity of codimension two: the *asymmetric cusp*.

3.4.1 The asymmetric cusp

The defining conditions of the asymmetric cusp are

$$g = \frac{\partial g}{\partial x} = \frac{\partial g}{\partial \omega} = \det(d^2 g) = 0 \tag{3.15}$$

while its nondegeneracy conditions are

$$\frac{\partial^2 g}{\partial x^2} \neq 0 \qquad \frac{\partial^3 g}{\partial v^3} \neq 0 \tag{3.16}$$

where $\frac{\partial}{\partial v}$ is the directional derivative with respect to a zero eigenvector v of $d^2 g$, the Hessian of $g(x, \omega)$.

Figure 3.8a shows the (nonpersistent) diagram corresponding to the normal form of this singularity

$$g(x, \omega) = x^2 + \omega^3 = 0 \tag{3.17}$$

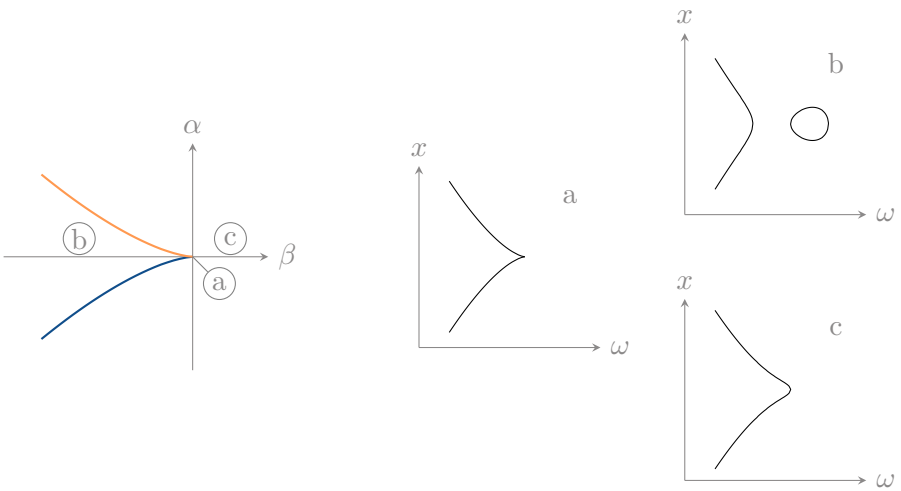

Figure 3.8 The asymmetric cusp and its persistent perturbations. Left: transition set in the parameter space of the universal unfolding (— isolas, — simple bifurcations). Right: bifurcation diagrams: a) unperturbed, b-c) persistent perturbations..

while figure 3.8b and c illustrate the persistent diagrams of a universal unfolding

$$G(x, \omega, \alpha, \beta) = x^2 + \omega^3 + \alpha + \beta\omega = 0 \tag{3.18}$$

The transition set in figure 3.8 is easily recognised in figure 3.7. Indeed, whenever an asymmetric cusp is found, singularity theory predicts a line of simple bifurcation points and a line of isola points delimiting the presence of a separate branch of solutions. In the context of forced oscillations these delimit the presence of DRCs.

3.5 DRCs in parameter space

3.5.1 Delimiting the presence of a DRC

Starting from figure 3.7 and specifically the asymmetric cusp (■), it is possible to delimit the presence of a DRC when design parameters are varied. Points corresponding to this singularity describe a line in the α-μ_2-f space. In figure 3.7 increasing μ_2 reduces the range of values of f for which a DRC is present, until the asymmetric cusp is encountered at μ_2^*. This is intuitively expected as large damping destroys resonance phenomena. Similarly, starting from a point on the line of asymmetric cusp in the α-μ_2-f space and decreasing μ_2 generates the two branches of the transition set associated with the unfolding of an asymmetric cusp: a family of isolas and one of simple bifurcations. As shown in the 3D plot of figure 3.9 these delimit a DRC.

The analysis is continued in the lower part of figure 3.9. Projecting the line of asymmetric cusps onto the α-μ_2 plane the zone in which a DRC is present can be delimited for different values of k, forming a surface in the α-μ_2-k space. The bottom plot in figure 3.9 shows these lines of asymmetric cusps for few values of k, to each of them correspond a 3D plot similar to the one shown for the nominal value of k. Hence, through this figure it is possible to determine the values of α, k and μ_2 for which a DRC is present in the frequency response.

3.5.2 Design of a fifth-order spring

Since detached resonance curves might restrict the application range of a nonlinear vibration absorber a natural question is how to design systems that avoid them. In the present context a natural choice is the addition of a fifth order spring to the absorber. The rationale behind this choice is that a fifth order spring does not influence the response for low values of f. This allows us to reuse the parameters (3.2) designed in [37], while influencing the response for higher forcing amplitudes when the absorber's performances are reduced due to the presence of DRCs.

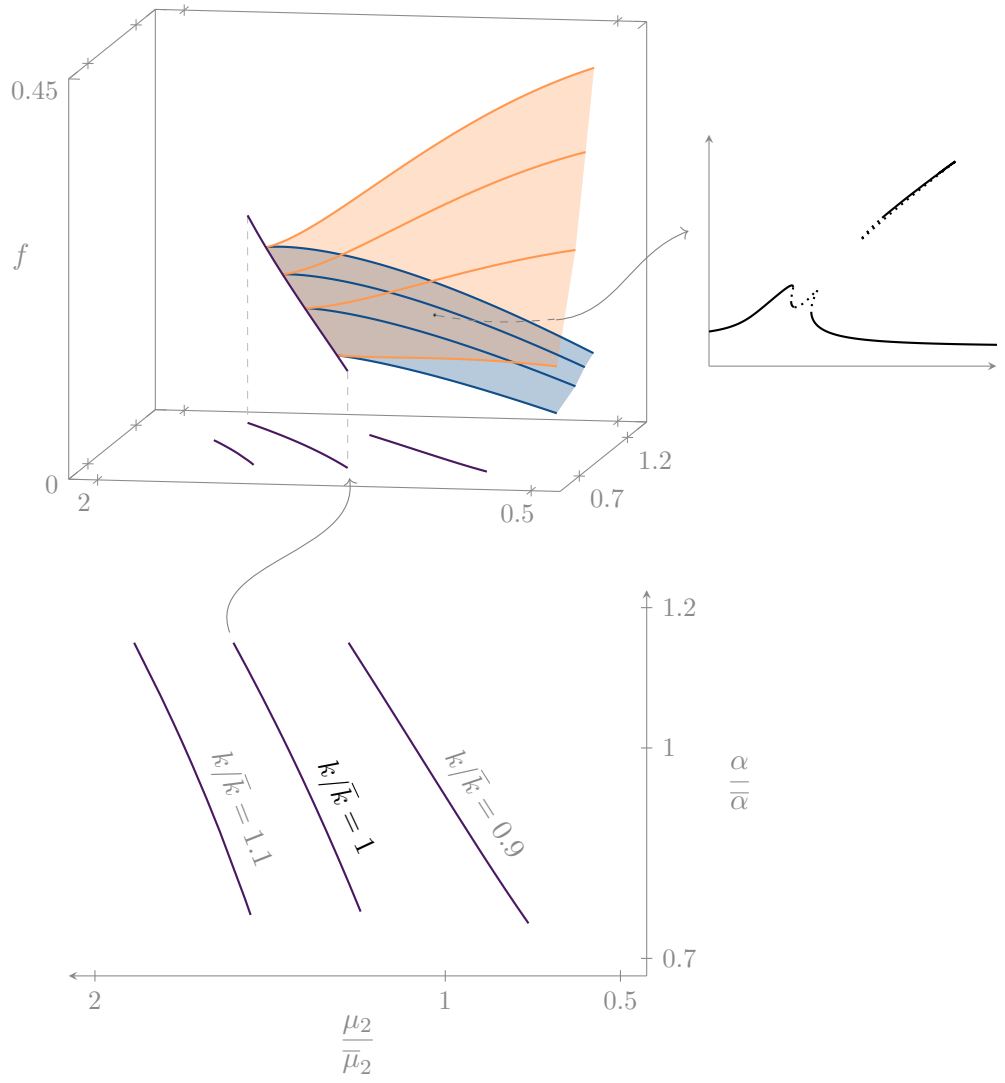

Figure 3.9 Characters of DRCs in parameter space: The bottom plot shows lines of asymmetric cusps in the μ_2-α plane for different values of k; each line determines the boundary in parameter space of the region where a DRC is present, as shown in the upper plots (— asymmetric cusp, — isola, — simple bifurcation).

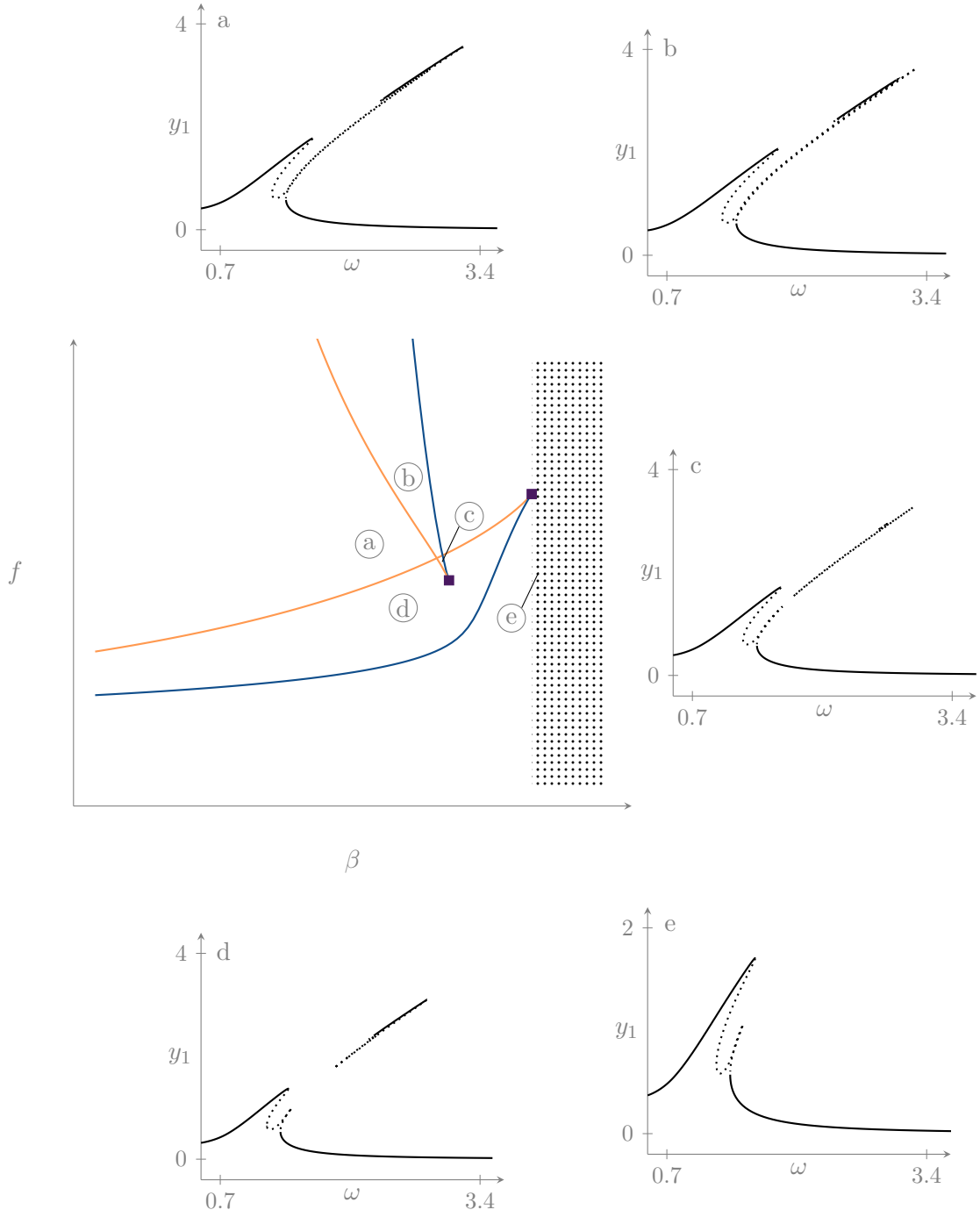

Figure 3.10 Effect of a fifth order spring on appearance and merging of DRCs: Two asymmetric cusps at $\beta \approx 10^{-4}$ and $\beta \approx 1.2\,10^{-4}$. The dotted area corresponds to a zone in which no DRC is present. a) $\beta = 8\,10^{-5}$, $f = .34$; b) $\beta = 9\,10^{-5}$, $f = .41$; d) $\beta = 9.75\,10^{-5}$, $f = .32$; e) $\beta = 9\,10^{-5}$, $f = .25$; f) $\beta = 13\,10^{-5}$, $f = .3$.

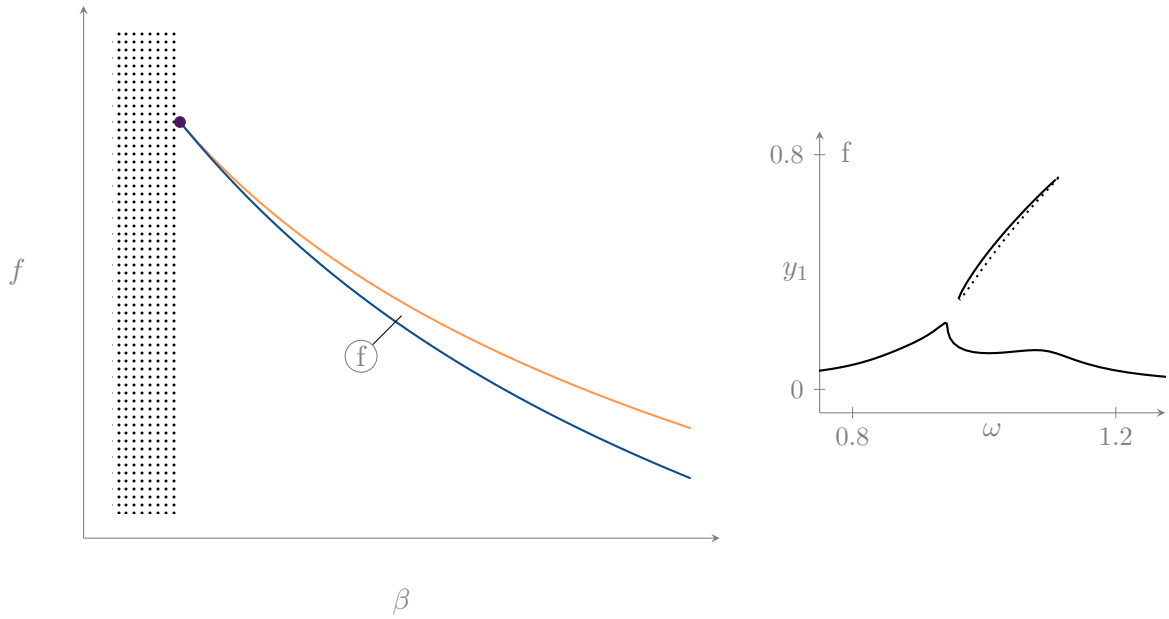

Figure 3.11 Effect of a fifth order spring on appearance and merging of DRCs: Asymmetric cusp at $\beta = 3.7\,10^{-2}$ and corresponding DRC in the response. The dotted area corresponds to a zone in which no DRC is present.

We revisit the analysis of the previous sections with the modified nonlinearity

$$f_{nl}(y) = \begin{pmatrix} y_1^3 + \alpha(y_1 - y_2)^3 + \beta(y_1 - y_2)^5 \\ \alpha(y_2 - y_1)^3 + \beta(y_2 - y_1)^5 \end{pmatrix} \tag{3.19}$$

The influence of the fifth-order spring is illustrated in figures 3.10 and 3.11. The analysis reveals three regions in which DRCs are present, each organised by an asymmetric cusp.

For design purposes a significant outcome is that no DRC exists for $\beta > \beta_2 \approx 1.2\,10^{-4}$. A new asymmetric cusp appears at $\beta = \beta_3 \approx 3.7\,10^{-2}$ (figure 3.11), providing a range of parameter $[\beta_2, \beta_3]$ where the model is free of DRCs.

Figure 3.10 also shows the presence of another asymmetric cusp at $\beta_1 \approx 10^{-4}$ and corresponding DRC for $\beta < \beta_1$. For completeness figure 3.12 shows this other DRC in the response of the second mass where it is more visible.

We remark that, although the computations of singularities relyed on the first-order approximation derived in appendix 3.A, the frequency responses showed were all computed using a shooting algorithm similar to the one described in [72]. These figures confirm the presence of the boundaries between the different frequency responses reported above and show that results of this chapter approximate well the behaviour of the equations.

A natural improvement is to use directly more accurate approximations to perform similar analyses. The fact that numerical techniques to identify and track singularities are already available [34, Ch. 7] makes this a concrete possibility. Moreover, these numerical techniques

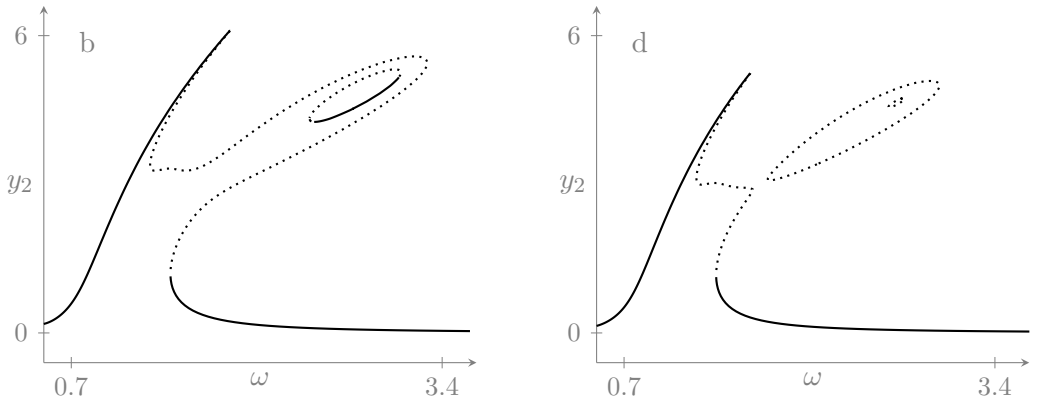

Figure 3.12 New DRC due to a fifth order spring, responses of the second mass in cases b and d of figure 3.10.

are at their essence the same ones commonly used by researcher in structural dynamics (continuation and bordering), something that should facilitate their integration with already developed tools.

3.6 Conclusions

This chapter studied the interconnection of two Duffing oscillators in the context of vibration absorption. The focus of the analysis was on appearance and merging of detached resonance curves and their characterisation in terms of isolas, simple bifurcations and asymmetric cusps. The latter provides a full characterisation of the geometry of these solutions in parameter space. Starting from it it is possible to quantitatively investigate the presence of these curves with respect to design parameters.

In the context of this thesis we think of this system as the simplest example of a resonance phenomenon obtained through interconnection. Under this viewpoint, the last part of this chapter is an attempt to characterise the effect that one the two subsystems (the absorber) has on the final interconnection. The choice of this subsystem is of course not casual, but rather dictated by the problem. In the next two chapters, and in particular in chapter 5, we undertake similar efforts in the context of excitable systems. Although techniques and phenomena will differ, the final objective will be the same, to understand how modifying a subsystem influences the behaviour of the resulting interconnection.

Appendix

3.A Reduction of first-order harmonic balance to a scalar equation

In this section, starting from a one-harmonic approximation of (3.1) (with a fifth-order spring), we arrive to a single equation that approximates the frequency response of the system. The equations of motion (in dimensionless form) are

$$M\ddot{y} + C\dot{y} + Ky + f_{nl}(y) = g\frac{f}{2}(\exp(\mathrm{j}\omega t) + \exp(-\mathrm{j}\omega t))$$

$$M = \begin{pmatrix} 1 & 0 \\ 0 & r \end{pmatrix} \qquad K = \begin{pmatrix} 1+k & -k \\ -k & k \end{pmatrix} \qquad C = \begin{pmatrix} \mu_1+\mu_2 & -\mu_2 \\ -\mu_2 & \mu_2 \end{pmatrix} \tag{3.20}$$

$$f_{nl}(y) = \begin{pmatrix} y_1^3 + \alpha(y_1-y_2)^3 + \beta(y_1-y_2)^5 \\ \alpha(y_2-y_1)^3 + \beta(y_2-y_1)^5 \end{pmatrix} \qquad g = \begin{pmatrix} 1 \\ 0 \end{pmatrix}$$

Defining

$$q = Ly \qquad L = \begin{pmatrix} 1 & 0 \\ 1 & -1 \end{pmatrix} \tag{3.21}$$

the equations of motion are rewritten as

$$L^T ML\ddot{q} + L^T CL\dot{q} + L^T KLq + L^T f_{nl}(Lq) = L^T g\frac{f}{2}(\exp(\mathrm{j}\omega t) + \exp(-\mathrm{j}\omega t)) \tag{3.22}$$

$$\begin{aligned} (1+r)\ddot{q}_1 - r\ddot{q}_2 + q_1 + \mu_1\dot{q}_1 + q_1^3 &= \frac{f}{2}(\exp(\mathrm{j}\omega t) + \exp(-\mathrm{j}\omega t)) \\ -r\ddot{q}_1 + r\ddot{q}_2 + kq_2 + \mu_2\dot{q}_2 + \alpha q_2^3 + \beta q_2^5 &= 0 \end{aligned} \tag{3.23}$$

Setting $q_1 = w_1 \exp(\mathrm{j}\omega t) + \overline{w_1}\exp(-\mathrm{j}\omega t)$, $q_2 = w_2\exp(\mathrm{j}\omega t) + \overline{w_2}\exp(-\mathrm{j}\omega t)$ and injecting in (3.23) yields for the first harmonic

$$g_1(w_1, w_2) := \quad -\omega^2(1+r)w_1 + \omega^2 r w_2 + w_1 + \mathrm{j}\mu_1\omega w_1 + 3w_1^2\overline{w_1} \quad = \frac{f}{2} \tag{3.24}$$

$$g_2(w_1, w_2) := \omega^2 r w_1 - \omega^2 r w_2 + k w_2 + \mathrm{j}\mu_2\omega w_2 + 3\alpha w_2^2\overline{w_2} + 10\beta w_2^3\overline{w_2}^2 = 0 \tag{3.25}$$

Equation (3.25) can be solved for w_1, yielding

$$w_1 = \psi(w_2) := w_2 - \frac{k}{\omega^2 r}w_2 - \mathrm{j}\frac{\mu_2}{\omega r}w_2 - \frac{3\alpha}{\omega^2 r}w_2^2\overline{w_2} - \frac{10\beta}{\omega^2 r}w_2^3\overline{w_2}^2 \tag{3.26}$$

The functions $g_1(w_1, w_2)$ and $\psi(w_2)$ verify, for $\theta \in \mathbb{R}$

$$\begin{aligned} g_1(\exp(\mathrm{j}\theta)w_1, \exp(\mathrm{j}\theta)w_2) &= \exp(\mathrm{j}\theta)g_1(w_1, w_2) \\ \psi(\exp(\mathrm{j}\theta)w_2) &= \exp(\mathrm{j}\theta)\psi(w_2). \end{aligned} \tag{3.27}$$

Thus for the equation obtained by substituting (3.26) in (3.24)

$$g_1(\psi(w_2), w_2) = \frac{f}{2} \tag{3.28}$$

a similar property holds, i.e. for all $\theta \in \mathbb{R}$

$$g_1(\psi(\exp(\mathrm{j}\theta)w_2), \exp(\mathrm{j}\theta)w_2) = g_1(\exp(\mathrm{j}\theta)\psi(w_2), \exp(\mathrm{j}\theta)w_2) = \exp(\mathrm{j}\theta)g_1(\psi(w_2), w_2) \tag{3.29}$$

Substituting $w_2 = x\exp(\mathrm{j}\phi)$ in (3.28), multiplying by $\exp(-\mathrm{j}\phi)$ and using (3.29) yields

$$g_1(\psi(x), x) = \frac{f}{2}\exp(-\mathrm{j}\phi) \tag{3.30}$$

where x and f are real variables but g_1 is complex-valued. Taking the square of the absolute value of both sides of (3.30) results in a real equation

$$g := |g_1(\psi(x), x))|^2 - \tfrac{1}{4}f^2 \tag{3.31}$$

whose solutions correspond to solutions of (3.24) and (3.25).

Furthermore, due to the structure of the g_i

$$\begin{aligned} g_1 &= w_1 h_1(|w_1|^2) + \omega^2 r w_2 \\ g_2 &= w_2 h_2(|w_2|^2) + \omega^2 r w_1 \end{aligned} \tag{3.32}$$

the resulting equation (3.31) depends quadratically on x and f, thus it is possible to substitute $X = x^2$ and $F = f^2$.

Setting $\beta = 0$ yields the frequency response of the system without fifth-order spring.

Chapter 4

The geometry of rest-spike bistability

The coexistence of a rest state with a spiking attractor is often a building block of bursting oscillations. While the latter have received a great deal of attention from the neurodynamics community, the mechanisms underlying rest-spike bistability in slow-fast systems have been explored less.

In the FitzHugh-Nagumo model fast positive feedback leads to bistability in the fast time-scale. Similarly, a slow source of positive feedback can be used in conjunction with the motif of excitability to obtain bistability between a fixed point and a limit cycle. While similar ideas appear in few other models in the literature, the objective of this chapter is to capture this process in a distinct dynamic variable, leading to a model with two slow variables.

This is achieved adding a slow inward current to a classical model of excitability, the Morris-Lecar model. The resulting model has a slow-fast structure similar to the one found in biological systems. Analysing it with geometric singular perturbation theory uncovers the geometry underlying this type of bistability.

4.1 Introduction

After the action potential, bursting [10] is probably the first type of pattern one comes across when studying electrical activity of excitable membranes. Its generation often rests on the coexistence of a fixed point with a spiking attractor when appropriate variables are held fixed [21, 51]. Despite this, the study of the mechanisms underlying this bistability in the context of slow-fast systems has received little attention.

In the neurodynamics literature we are aware of only two published models that aim at this. The first one was proposed by Hindmarsh and Rose [44] in their classical work on low-frequency spiking. The second one is the more recent transcritical model [19] proposed

as a two-dimensional reduction of the Hodgkin-Huxley model with a slow inward (calcium) current added.

Both models are planar with one fast and one slow variable and can be analysed with phase-portrait techniques similar to those used for the FitzHugh-Nagumo model in chapter 2. In that case the slow variable acts exclusively as a recovery variable, slowly counteracting changes in the voltage. On the contrary, in the two slow-fast model that show rest-spike bistability, the slow variable can also be a source of positive feedback.

In the Hindmarsh-Rose model this is obtained making the slow nullcline in the FitzHugh-Nagumo model nonmonotonic (quadratic). This change does not alter the cubic-shaped critical manifold but leads to multiple fixed points on it. One of them is stable and coexists with a spiking attractor in a range of input currents.

The transcritical model, instead, realises the slow positive feedback changing how the slow variable enters the fast dynamics: with a quadratic term rather than a linear one. The resulting phase portrait is quite different from the classical one studied by FitzHugh. Following [19], a subsequent analysis in [29] showed the key role of a transcritical bifurcation in shaping the critical manifold of this model.

Both models can be analysed graphically to explain the dynamical mechanisms underlying this bistability but do not fully capture the physiology of the phenomenon. The present chapter aims at filling this gap, studying a model that is simple enough to allow a geometric analysis but at the same time closer to the structure of excitable cells.

Our starting point is the model developed by Morris and Lecar [70]. This model follows the formalism established by Hodgkin and Huxley [46], combining an instantaneous inward current with a slow outward current. These correspond to the basic elements of the classical FitzHugh-Nagumo model, making the geometry of the two models essentially the same. In this sense the Morris-Lecar model combines the physiological interpretation of the Hodgkin-Huxley model with the mathematical tractability of the FitzHugh-Nagumo circuit.

Augmenting the Morris-Lecar model with a slow source of positive feedback, corresponding to a slowly-activating inward current, results in a model that is conductance based and shows rest-spike bistability. This slow-fast system can be analysed using geometric singular perturbation theory. The fast dynamics is one dimensional and shares the bistable dynamics common to excitable models, whereas the slow dynamics is two-dimensional and can be analysed comprehensively. This generalised picture offers a number of advantages. From a physiological viewpoint, it is not only more interpretable but also more realistic. This is because the kinetics of slow inward and slow outward currents often differ significantly from each other in actual neurons. From a mathematical viewpoint, it also offers a more coherent picture. The critical manifold is N-shaped, as commonly found in conductance-based models due to bistability in the fast time-scale. Slow variables determine the slow dynamics but their different roles do not influence the geometric structure of the critical manifold.

4.2 A Model of Rest-Spike Bistability

The model studied in this chapter is defined by*

$$\begin{aligned} \varepsilon \dot{v} &= i - i_{ion}(v,n,p) \\ \dot{n} &= -n + S_n(v) \\ \tau \dot{p} &= -p + S_p(v) \end{aligned} \tag{4.1}$$

where ε is a small parameter representing two distinct time-scales. The total ionic current is the sum of a leak current and three voltage-gated currents:

$$\begin{aligned} i_{ion} &= g_l(v - v_l) + S_m(v)(v-1) + n(v+1) + p(v-1) \\ &= c(v) + c_n(v)n + c_p(v)p \end{aligned} \tag{4.2}$$

while $S_x(v)$ are activation functions of the form

$$S_x = \frac{g_x}{2}\left(\tanh\left(\frac{v - a_x}{b_x}\right) + 1\right) \tag{4.3}$$

The parameters $v_- = -1 < v_l < v_+ = +1$ can be thought of as reversal potentials. In the absence of an external current i, the voltage range $[-1, 1]$ is positively invariant. The currents $S_m(v)(v-1)$ and $p(v-1)$ are then negative (inward currents) whereas the current $n(v+1)$ is positive (outward current). The variables n and p are gating variables that model the slow activation of the two currents $p(v-1)$ and $n(v+1)$. The inward current $S_m(v)(v-1)$ has instantaneous activation, a standard simplification for currents that activate in the fast time-scale.

The main qualitative difference with respect to the Morris-Lecar model is the slow inward current $p(v-1)$. In the absence of this term, the model is two-dimensional and has a phase portrait similar to the classical FitzHugh-Nagumo model. With this additional slow inward current, both continuous spiking and rest coexist for the same value of applied current, as shown by the simulation in figure 4.1 (numerical values of the parameters are in appendix 4.B).

Through geometric singular perturbation theory [22, 41, 63] it is possible to study the slow-fast system (4.1) in the limit of ε tending to zero. The singular limit of this model is the differential-algebraic system

$$\begin{aligned} i &= i_{ion}(v,n,p) \\ \dot{n} &= -n + S_n(v) \\ \tau \dot{p} &= -p + S_p(v) \end{aligned} \tag{4.4}$$

*Compared to the Morris-Lecar model we normalize voltage so that reversal potentials are between 1 and -1 and assume that activation variables have time constants independent from v.

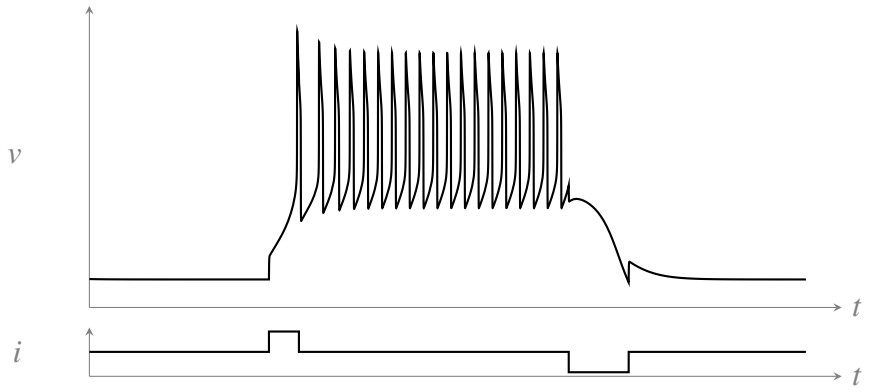

Figure 4.1 Rest-spike bistability in the model (4.1).

which we call slow dynamics or reduced system. After rescaling time, the same limit leads to the layer (or fast) dynamics

$$\begin{aligned} \dot{v} &= i - i_{ion}(v,n,p) \\ \dot{n} &= 0 \\ \dot{p} &= 0 \end{aligned} \tag{4.5}$$

Fixed points of this system correspond to the critical manifold $\mathcal{C}_0$

$$i_{ion}(v,n,p) = i \tag{4.6}$$

to which the slow dynamics (4.4) is constrained. Normally-hyperbolic compact subsets of $\mathcal{C}_0$ persist as invariant manifolds of (4.1) for ε small enough. These manifolds are not necessarily unique but in the following we assume one family of perturbations $\mathcal{C}_\varepsilon$ fixed and call them slow manifolds.

Perturbations of subsets of $\mathcal{C}_0$ maintain their type of stability with corresponding (local) stable and unstable manifolds. These admit invariant foliations, with each point on the critical manifold acting as base for a fibre. Invariance of the foliation can be interpreted as points on each fibre "shadowing" the corresponding base point, in forward time for points on the stable manifold and backward time for those on the unstable one. Points on C_ε follow a slow dynamics that is a regular perturbation of the reduced system (4.4).

A point x on the critical manifold is normally hyperbolic if it is a hyperbolic fixed point of the layer dynamics. If this is the case, as $\varepsilon \to 0$ the fibres based at x tend to its stable and unstable manifolds in the layer dynamics. In the case of (4.1) the layer dynamics (4.5) is one dimensional, so that hyperbolic fixed points are either attractive or repulsive, with their invariant manifolds corresponding to lines with n and p constant.

For the parameter values considered here (appendix 4.B) the critical manifold can be divided in three normally-hyperbolic branches. These are separated by two lines of folds $\mathcal{F}_l$

and $\mathcal{F}_h$, which verify

$$\frac{\partial i_{ion}}{\partial v} = \frac{dc}{dv}(v) + n + p = 0 \tag{4.7}$$

These two lines of folds are connected by an unstable branch $\mathcal{S}_r$. The other branches, $\mathcal{S}_a^-$ and $\mathcal{S}_a^+$, are both stable. Figure 4.2 shows the typical shape of the critical manifold for fixed i.

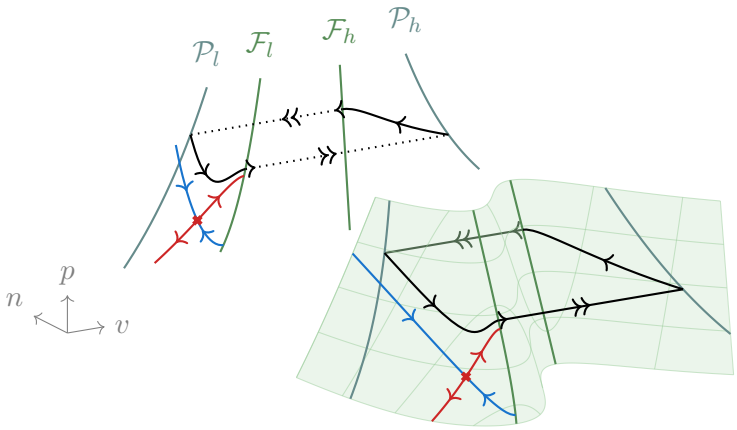

Figure 4.2 Reduced dynamics (4.5) on the critical manifold (4.4) and its projection onto the v-p plane, together with the lines of folds $\mathcal{F}_l$, $\mathcal{F}_h$ and their projections $\mathcal{P}_l$, $\mathcal{P}_h$. A saddle point and its stable (—) and unstable (—) manifolds in the reduced system are shown on the critical manifold. The black trajectory is a singular relaxation oscillation composed of two slow parts (single arrow) connected by two trajectories along fast fibres (double arrow, dotted in the projection).

Around any point not on the lines of folds, the critical manifold can be parametrised with the slow variables n and p. This parametrisation, however, does not extend to the whole manifold due to the presence of folds. Following [91, 92, 101], we can use v and p to overcome this problem. This parametrisation corresponds to the solution $n(v, p, i)$ of (4.6) and is valid in the interval $v \in (-1, 1)$ (in fact $v \in (-1, \infty)$). Geometrically, using v and p as coordinates corresponds to project manifold and slow dynamics onto the v-p plane as shown in figure 4.2.

The reduced dynamics in these coordinates is obtained differentiating the constraint in (4.4) and substituting $n(v, p, i)$. This leads to two equations of the form

$$\begin{aligned} \frac{\partial i_{ion}}{\partial v}\dot{v} &= -\frac{\partial i_{ion}}{\partial n}\dot{n} - \frac{\partial i_{ion}}{\partial p}\dot{p} \\ \tau\dot{p} &= -p + S_p(v) \end{aligned} \tag{4.8}$$

The first equation becomes singular on the lines of folds $\frac{\partial i_{ion}}{\partial v} = 0$. Multiplication by $\frac{\partial i_{ion}}{\partial v}$ recovers a regular differential equation

$$\begin{aligned} \dot{v} &= -\frac{\partial i_{ion}}{\partial n}\dot{n} - \frac{\partial i_{ion}}{\partial p}\dot{p} \\ \tau\dot{p} &= \frac{\partial i_{ion}}{\partial v}(-p + S_p(v)) \end{aligned} \tag{4.9}$$

The original system (4.8) and the desingularised one (4.9) share the same trajectories with different time parametrisations. In particular, in (4.9) time is reversed on the unstable branch $\frac{\partial i_{ion}}{\partial v} < 0$ and new fixed points can appear on the lines of folds. These are called folded singularities and verify

$$\frac{\partial i_{ion}}{\partial v} = 0 \qquad \frac{\partial i_{ion}}{\partial n}\dot{n} + \frac{\partial i_{ion}}{\partial p}\dot{p} = 0 \tag{4.10}$$

Away from the lines of folds the two systems (4.8) and (4.9) are largely equivalent but important differences occur in the neighbourhood of $\mathcal{F}_l$ and $\mathcal{F}_h$. Moreover, near these lines the perturbed dynamics is no longer constrained by normal hyperbolicity and cannot be obtained as a regular perturbation of the reduced system (4.8).

Different dynamical phenomena are possible near lines of folds. The least degenerate situation occurs when the desingularised vector field has no zeros:

$$\frac{\partial i_{ion}}{\partial n}\dot{n} + \frac{\partial i_{ion}}{\partial p}\dot{p} \neq 0 \tag{4.11}$$

Under this assumption the desingularised vector field (4.9) can point either to the unstable branch or the stable one. Assuming the additional nondegeneracy condition

$$\frac{\partial^2 i_{ion}}{\partial v^2} \neq 0 \tag{4.12}$$

the first case corresponds to jump points; at them the reduced system (4.8) admits two solutions backward in time but none forward. For $\varepsilon > 0$ the stable branch of $\mathcal{C}_\varepsilon$ near these points can be continued using the flow [92]. Doing so shows that trajectories on the slow manifold pass the folds and reach points in state space where the fast dynamics (4.5) dominates. Under its influence the trajectory reaches a fibre contained in the stable manifold of the other stable branch of C_ε.

Condition (4.11) corresponds to the vector field (4.1) being transverse to the critical manifold (4.6), a condition that is violated at folded singularities. These are fixed points of the desingularised system (4.9) but not necessarily of the reduced dynamics (4.8). Depending on the type of fixed point they can correspond to the singular limit of canard trajectories, i.e. intersections between stable and unstable branches of the slow manifold [91]. Along lines of

folds the desingularised vector field can change direction only at these points, so that the boundary of the set of jump points is composed of folded singularities [101].

4.3 Reduced Dynamics

This section studies the reduced system (4.8) numerically, highlighting its persistence properties for small $\varepsilon > 0$.

Fixed points of the system can be parametrised by v through the steady-state i-v curve

$$i_s(v) = i_{ion}(v, S_n(v), S_p(v)) \tag{4.13}$$

This is shown in figure 4.6 and is an S-shaped curve, with two folds separating three families of fixed points $\mathcal{X}_l$, $\mathcal{X}_m$ and $\mathcal{X}_h$; $\mathcal{X}_l$ corresponds to low voltages, $\mathcal{X}_m$ to intermediate voltages and $\mathcal{X}_h$ to high voltages. For fixed i, we denote points in each family with corresponding lower-case letters x_l, x_m and x_h. In addition to these three fixed points, the desingularised dynamics (4.9) has a folded focus $x_f \in \mathcal{F}_l$. This does not lead to canard trajectories [91] and only delimits jump points on $\mathcal{F}_l$.

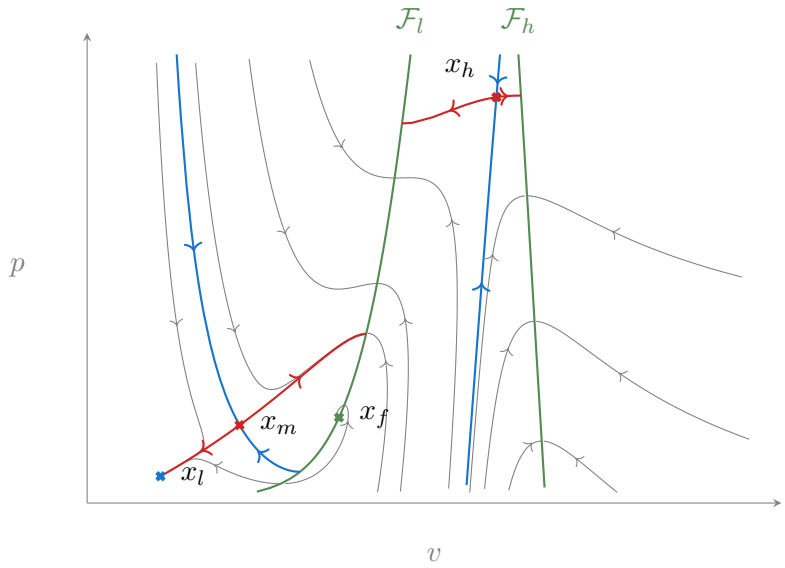

Figure 4.3 Typical phase portrait of the reduced system (4.8). Fixed points of the desingularised system (4.9) are denoted by crosses, x_l is a stable node, x_m and x_h are saddle points and x_f is a folded focus (unstable). Few trajectories (—) as well as stable (—) and unstable (—) manifolds of the saddle points are shown. Along the two lines of folds $\mathcal{F}_l$ and $\mathcal{F}_h$ the system is singular: trajectory at those points are defined only in forward or backward time; the first of these two cases corresponds to jump points. The stable manifold of x_m separates initial conditions in $\mathcal{S}_r^-$ (left of $\mathcal{F}_l$) that reach a jump point from those that converge to x_l.

Figure 4.3 shows the typical phase portrait of (4.8). The fixed point x_l is a stable node, while x_m and x_h are both saddle points. Their stable and unstable manifolds do not extend beyond $\mathcal{F}_l$ and $\mathcal{F}_h$ due to loss of existence and uniqueness along these lines. In particular, unstable manifolds terminate at jump points.

For $\varepsilon > 0$ hyperbolic fixed points persist in the slow dynamics with their stable and unstable manifolds [22, 90]. In the perturbed system (4.1) these fixed points are still hyperbolic. In particular, saddle points remain saddle, with their invariant manifolds being obtained as a combination of trajectories of the slow dynamics and fast fibres. The unstable manifold of x_m is completely contained in the slow manifold. Its stable manifold, instead, is two dimensional: It includes the stable manifold in $\mathcal{C}_\varepsilon$ as well as all fast fibres based on that curve. In the singular limit this surface tends to the stable manifold of x_m in the reduced system (4.8) and all nearby segment with constant n and p that intersect it. Similarly, x_h perturbs to a saddle with a one-dimensional stable manifold and a two-dimensional unstable manifold.

Adding a trivial equation for i to (4.1), the same is true for the family of fixed points $x_m(i)$. At least for i in a small interval, this family persists together with its two-dimensional unstable manifold and three-dimensional stable manifold. Sections of these manifolds for fixed i coincide with the invariant manifolds of the corresponding fixed point.

When i varies on larger domains the outlined phase portrait can undergo two distinct qualitative changes: Increasing i leads to a fold of the i-v curve at which x_l and x_m merge in a saddle-node bifurcation, leaving only one fixed point $x_h \in \mathcal{S}_r$. Likewise, decreasing i, x_m and x_h reach a similar fate, leaving $x_l \in \mathcal{S}_a^-$ as the only fixed point.

To obtain this second bifurcation it is necessary that one of the two fixed points crosses the line $\mathcal{F}_l$ and changes branch*. In our case x_m crosses $\mathcal{F}_l$. This passage corresponds to an exchange of stability with the folded singularity through a folded saddle-node [62]. Beyond this crossing, the folded singularity is a saddle, while x_m is a node of the reduced system. In a similar fashion increasing the applied current leads to x_h crossing $\mathcal{F}_h$, which happens once x_h is the only fixed point left. After this crossing, x_h is a stable fixed point on an attractive branch.

Finally, varying i can lead to changes in the type of folded singularity. As already mentioned $x_m \in \mathcal{F}_l$ corresponds to a folded saddle-node, thus varying i and moving x_m between branches leads to different types of folded singularity: It is a saddle when $x_m \in \mathcal{S}_r$ and a node when $x_m \in \mathcal{S}_a^-$. Both situations lead to canard trajectories [91]. Moreover, since x_f is a focus in the phase portrait described above, it has to change to a node before becoming a folded saddle-node.

*This assumes that the bifurcation does not happen exactly on $\mathcal{F}_l$.

4.4 Rest-spike bistability

Returning to the phase portrait in figure 4.3, this section analyses the global return mechanism that leads to rest-spike bistability.

Away from the slow manifold the dynamics is dominated by (4.5) and tends to one of the two attractive branches that perturb from $\mathcal{S}_a^-$ and $\mathcal{S}_a^+$. On these branches, away from fold points, the dynamics is a perturbation of the reduced system (4.8).

Close to a lines of folds, near jump points, trajectories on a stable branch of the slow manifold pass the folds and quickly reach a fibre of the opposite branch. After this fast passage the trajectory is dominated once again by the slow dynamics. Points near a stable branch of the critical manifold in a neighbourhood of a line of folds follow similar paths, with the flow contracting in the direction transverse to the manifold [92].

In the singular limit $\varepsilon = 0$ this corresponds to trajectories on the slow manifold reaching a line of folds and jumping to the opposite branch, following lines of constant n and p as shown in figure 4.2. The points at which these singular trajectories arrive correspond to the projections of $\mathcal{F}_l$ and $\mathcal{F}_h$ along fast fibres. We call these projections $\mathcal{P}_l \subset \mathcal{S}_a^-$ and $\mathcal{P}_h \subset \mathcal{S}_a^+$.

Based on this construction, the analysis of the system can be continued referring only to the v-p plane and the reduced dynamics: When a trajectory reaches a jump point it is transported to the corresponding projection keeping p fixed, as shown in figure 4.2 for a limit cycle.

Rest-spike bistability follows from how the stable and unstable manifold of x_m constrain trajectories. The role of the stable manifold is simple, it separates initial conditions on $\mathcal{S}_a^-$ that reach a jump point on $\mathcal{F}_l$ from those that remain on the critical manifold and tend to x_l. The unstable manifold, instead, determines if the system is multistable. This is the case if the unstable manifold stays away from x_l. Otherwise almost all trajectories converge to x_l. These two situations are treated separately in the following sections.

4.4.1 Multistability

In the following, x_1 denotes the intersection of the unstable manifold of x_m with $\mathcal{F}_l$, and x_{-1} the intersection of the stable manifold of x_m with $\mathcal{P}_l$. Following the singular flow from x_1 leads to $x_2 \in \mathcal{P}_h$, then to $x_3 \in \mathcal{F}_h$ and back to $\mathcal{P}_l$ at x_4 (see figure 4.4).

This section assumes the situation depicted in figure 4.4 in which the trajectory starting at x_4 reaches a jump point on $\mathcal{F}_l$ (x_5). The point x_4 and the line $p = g_p$ delimit a segment $\mathcal{I}_l \subset \mathcal{P}_l$. The reduced dynamics maps this segment to $\mathcal{F}_l$ in finite time. The map Π_l defined in this way is smooth: It can be obtained through the desingularised reduced system (4.9), and this vector field is transverse to $\mathcal{F}_l$ at all points in $\Pi_l(I_l)$. Similarly, on $\mathcal{S}_a^+$ we can define a segment $I_h \subset \mathcal{P}_h$ between x_2 and $p = g_p$, and a corresponding map $\Pi_h : \mathcal{I}_h \to \mathcal{F}_h$. Projection along fast fibres is denoted by Π_f (from $\mathcal{F}_l$ to $\mathcal{P}_h$ and from $\mathcal{F}_h$ to $\mathcal{P}_l$). Since the

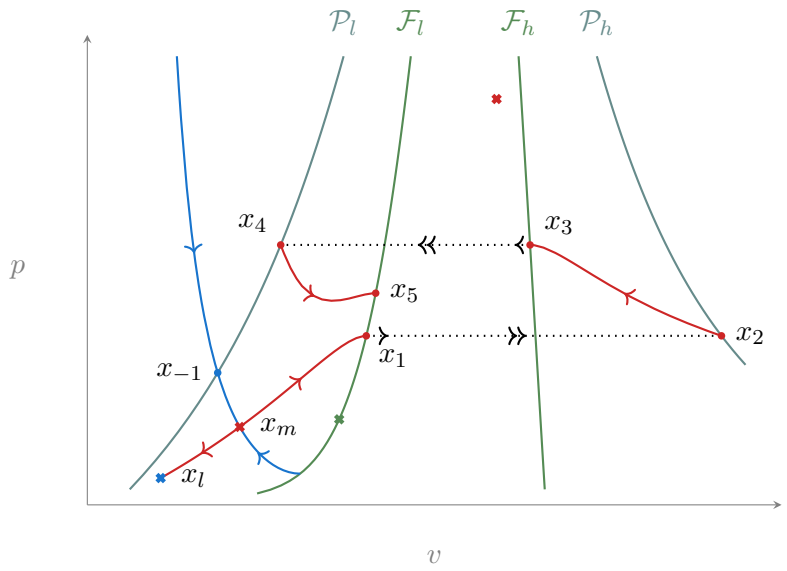

Figure 4.4 Reduced dynamics in the multistable case. The stable manifold of x_m (—) separates initial conditions that reach a jump point on $\mathcal{F}_l$ from those that converge to x_l. Jump points are mapped to their projections (e.g. x_1 to x_2 and x_3 to x_4). The unstable manifold of x_m (—) delimits an invariant set for the dynamics.

dynamics is bounded by the line $p = g_p$. We have

$$\Pi_f \circ \Pi_l(\mathcal{I}_l) \subset \mathcal{I}_h \qquad \Pi_f \circ \Pi_h(\mathcal{I}_h) \subset \mathcal{I}_l \tag{4.14}$$

which allows us to define the singular Poincaré map

$$\Pi = \Pi_f \circ \Pi_h \circ \Pi_f \circ \Pi_l : \mathcal{I}_l \to \mathcal{I}_l \tag{4.15}$$

This construction shows that the stable manifold of x_m divides the state space into two invariant sets. One is the basin of attraction of x_l, while the other one has dynamics characterized by the Poincaré map (4.15). Since this is a smooth map of an interval into itself it admits at least one fixed point that corresponds to a singular relaxation oscillation. As shown in [92], if this fixed point is hyperbolic, under the additional hypothesis that the singular trajectory intersects $\mathcal{P}_l$ and $\mathcal{P}_h$ transversally, it perturbs to a hyperbolic limit cycle for $\varepsilon > 0$. In fact the Poincaré map (4.15) is (up to conjugacy) a global version of the one used in that reference.

In general this construction guarantees only multistability, to obtain a more accurate picture a detailed characterization of the map (4.15) is necessary. While this is beyond the scope of this work, it is plausible to expect that this map has a unique and attracting hyperbolic fixed point, at least for large ranges of parameter values. The reason for this is that trajectories between $\mathcal{P}_l$ and $\mathcal{F}_l$ are attracted towards the unstable manifold of x_m, which

is transverse to $\mathcal{F}_l$, a situation that naturally leads to Π_l being a contraction with respect to some metrics. The maps Π_f can be largely ignored, parametrising all intervals using the p coordinate of their points reduces these projections to the identity. This leaves only the map Π_h, and it would be enough for this map to be non-expanding in an appropriate metric to obtain that Π is a contraction.

4.4.2 Monostability

Constructing the Poincaré map (4.15) requires that x_4 falls inside the interval defined by x_{-1} and $p = g_p$ on $\mathcal{P}_l$. Figure 4.5 shows the reduced phase plane of (4.1) when this is not the case. In this situation most trajectories on $\mathcal{S}_a^-$ and $\mathcal{S}_a^+$ are attracted by the stable fixed point x_l, the only exception being the stable manifold of x_m.

This can be seen through a construction similar to the previous one, but starting from $x_{-1} \in \mathcal{P}_l$, and following the singular flow "backward" in time as shown in figure 4.5. The first step leads to $\mathcal{F}_h$ using the inverse of Π_f; continuing with the slow flow the trajectory arrives to $\mathcal{P}_h$ and from it the inverse of the fast projection leads back to $\mathcal{S}_a^-$ on the line of folds $\mathcal{F}_l$. Finally, through the slow dynamics, the trajectory reaches $\mathcal{P}_l$, at a point that we call x_{-2}. Any compact segment in $\mathcal{P}_l$ that lies between x_{-1} and x_{-2} is mapped to the segment in $\mathcal{P}_l$ delimited by x_4 and x_{-1}. Since any point strictly inside this second segment converges to x_l, the same conclusion extends the initial points.

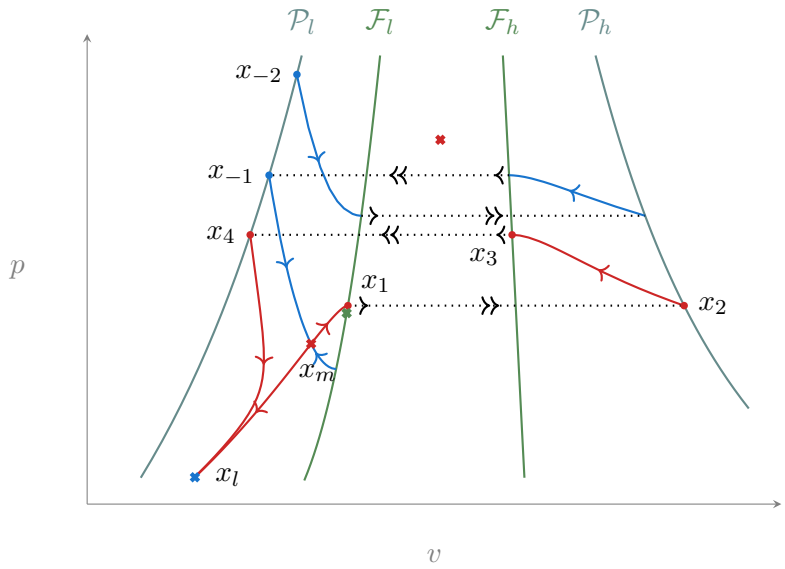

Figure 4.5 Reduced dynamics in the monostable case. The stable manifold of x_m (——) separates initial condition that arrive to a jump point on $\mathcal{F}_l$ from those that converge to x_l (not shown). The unstable manifold of x_m (——) converges to x_l after one jump. Similarly, almost all initial conditions on stable branches converge to x_l, the only exception are the ones that lie on the stable manifold of x_m.

The same argument shows that points in the portion of $\mathcal{S}_a^-$ delimited by the trajectories starting at x_{-1} and x_{-2} tend to x_l. The only exception being these boundary trajectories, they reach x_m and points on them belong to its stable manifold. The same argument can be iterated on $\mathcal{S}_a^-$ and adapted to $\mathcal{S}_a^+$, leading to the conclusion that almost all points on $\mathcal{S}_a^-$ and $\mathcal{S}_a^+$ are in the basin of attraction of x_l*. This situation persists for $\varepsilon > 0$, and since most points are attracted to stable branches of the slow manifold, we obtain that for almost all initial conditions the perturbed dynamics converges to x_l.

4.4.3 Homoclinic trajectory and bifurcation diagram

Transitions between monostability and bistability in system (4.1) are controlled by the applied current i. The phase portraits in figures 4.4 and 4.5 suggest the presence of a homoclinic trajectory, which can be obtained by decreasing the applied current from the bistable case. In the singular limit this trajectory corresponds to the condition $x_4 = x_{-1}$ and delimits the boundary of bistability. The value of applied current at which this happens will be denoted by i_H. While we cannot expect that this homoclinic trajectory persists for $\varepsilon > 0$ with i fixed, it is natural to ask whether for $\varepsilon > 0$, fixed and small, we can find an $i_H(\varepsilon)$, close to i_H, at which a homoclinic trajectory exists. There is a natural transversality condition that guarantees this property. The family of fixed points $x_m(i)$ admits a three-dimensional stable manifold and a two-dimensional unstable one. Their intersection is a homoclinic trajectory. In the singular limit, following the unstable manifold of $x_m(i)$ leads back to $\mathcal{S}_a^-$ after two jumps. Extending $\mathcal{C}_0$ to include i, $x_m(i)$ is a (normally hyperbolic) invariant set in it, with two-dimensional invariant manifolds. The continuation of the unstable one using the singular flow intersects the stable manifold in the plane $i = i_H$ after two jumps. If this intersection

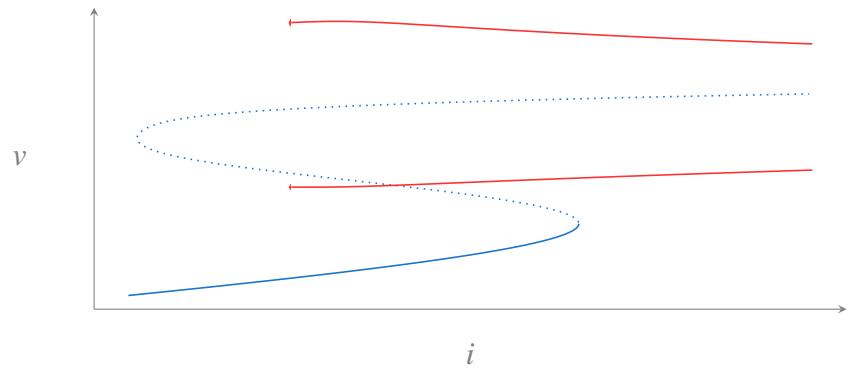

Figure 4.6 Bifurcation diagram of (4.1). Solid lines denote stable solutions, dotted correspond to unstable ones; blue lines correspond to fixed points, red lines to limit cycle, in the latter case both maximum and minimum are shown.

*This assumes that the stable manifold of x_m constructed in this way is not bounded in p. Numerical computations confirm this.

is transverse then it persists for small ε and i close to i_H. This is shown in appendix 4.A adapting the arguments used in [92] to prove existence of relaxation oscillations.

To conclude this section, figure 4.6 shows the bifurcation diagram of the system computed with AUTO-07p [16]. The numerics confirms the presence of a family of limit cycle (red curves), which terminates in a homoclinic trajectory for low values of i (the numerical continuation was stopped at period $T = 10^4$).

4.5 A common geometric picture

The bifurcation diagram of the previous section is only one among the many possible scenarios that can be modulated to obtain bursting. A natural question is if also other scenarios are compatible with the three-dimensional geometry of figure 4.2. While a detailed study of all the possibilities is beyond the scope of the present work, we wish to highlight how different types of bistability could share the same geometric structure. To do this we use ideas and techniques from [79]. As in section 4.3 we identify fixed points with the i-v curve

$$i_s(v) = i_{ion}(v, S_n(v), S_p(v)) \tag{4.16}$$

and divide them in three families $\mathcal{X}_l$, $\mathcal{X}_m$ and $\mathcal{X}_h$, separated by two folds. As noted in section 4.3, there is a value of current i_c, between the two folds, at which x_m crosses $\mathcal{F}_l$ to enter the unstable branch $\mathcal{S}_r$. The scenario studied in section 4.4 assumes $i_c < i_H$ since the homoclinic bifurcation occurs when $x_m \in \mathcal{S}_a^-$.

A first variation consists in the bistable range extending to current values for which $x_m \in M$. The transition $x_m \in F_l$ corresponds to a folded saddle-node. Beyond this $x_m \in M$ is a node of the reduced dynamics while x_f is a saddle. In this case the analysis is easily adapted from section 4.4, substituting the stable manifold of x_m with the one of x_f (now a folded saddle), and using $\Pi_f(x_f)$ in place of $x_2 = \Pi_f(x_1)$. Figure 4.7 shows the corresponding geometric construction. A classical example where this scenario occurs is the Hodgkin-Huxley model with the reversal potential of potassium increased. This situation of bistability has been studied in the early work [82]. Its planar reduction leads to the transcritical model [32]. Also in this case the boundary of bistability is a singular homoclinic trajectory. This trajectory, however, has to go through the folded singularity x_f to reach x_m on the unstable branch $\mathcal{S}_r$.

Both cases discussed so far assume that x_m and x_h collide in a fold on $\mathcal{S}_r$. Yet another scenario corresponds to this fold occurring on $\mathcal{S}_a^-$, after x_h crosses $\mathcal{F}_l$. Also this crossing leads to a folded saddle-node, after which $x_h \in \mathcal{S}_a^-$ can perturb to a stable fixed point. Local analysis around folded saddle-node shows the possibility of Hopf bifurcations [62], which are indeed found numerically. After this the system presents two stable fixed points. The relevant part of the reduced dynamics in this case is shown in figure 4.7: the stable manifold of x_m acts as separatrix between the basins of attraction of the two stable fixed points, while

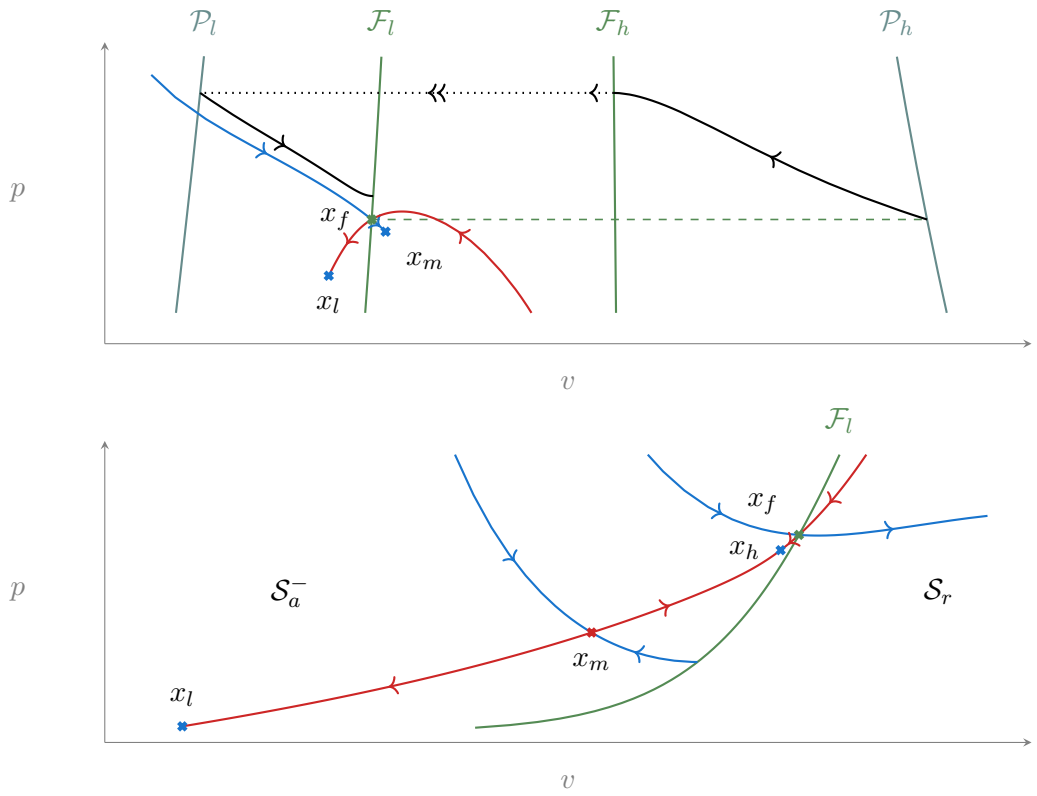

Figure 4.7 Alternative scenarios that can lead to bistability. Top: geometric construction when a folded saddle (x_f) takes the place of x_m. Bottom: bistability between two fixed points (x_l and x_h).

the one of x_f (a folded saddle) separates initial conditions that reach a jump point on $\mathcal{F}_l$ from those that remain on the critical manifold.

The examples above suggest that many possible variants for transitions between monostability and bistability are possible. We also note that many of the geometric constructions used in [29, 31, 79] have an analogue in the current geometric setting. For example, changing the relative position of rest state and limit cycle leads to oscillations in which spikes undershoot compared to rest, contrary to the case shown in figure 4.1. This flexibility is interesting in connection with the themes of the next chapter, which focuses more on how a single structure can generate multiple patterns.

4.6 Connections with phase portrait analysis

This last section of the chapter aims at clarifying the connection between the proposed three-dimensional model and the two published slow-fast phase portraits of rest-spike bistability.

The first phase portrait goes back to the seminal work of Hindmarsh and Rose [44, 45]. In one of the earliest attempts to model slow spiking and bursting, Hindmarsh and Rose proposed

to modify the FitzHugh-Nagumo model with a recovery variable that has a nonmonotonic activation function. Geometrically, this situation corresponds to a degenerate case of the planar pictures described in section 4.3 and section 4.4, in which all essential elements are contained on a line. As a result, the main elements of the three-dimensional dynamics can be captured by constraining it to a plane, resulting in a simplified two-dimensional model of rest-spike bistability. This is characterised by the classical N-shaped critical manifold, as shown in figure 4.8. The price paid for this simplification is that the flexibility of the two-dimensional slow dynamics described in section 4.5 is lost. For instance, bistability is only possible if x_l lies outside the strip delimited by $\mathcal{P}_l$ and $\mathcal{F}_l$, ruling out patterns in which the voltage of the resting state is between maximum and minimum of the spike.

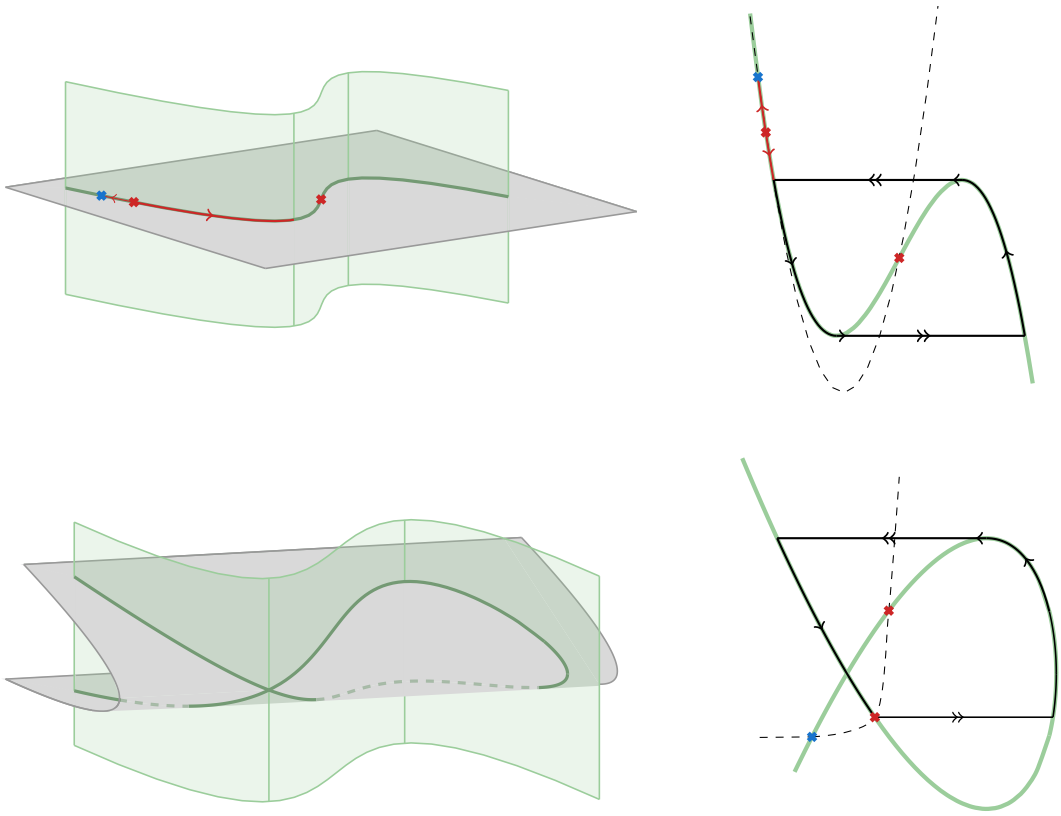

Figure 4.8 Bistable slow-fast phase portraits as reduction of a larger dimensional model. Left: critical manifolds obtained as the intersection of a higher-dimensional one (——) with a surface (gray). Right: corresponding phase plane with the critical manifold obtained (——) and a possible nullcline for the slow variable (- - -) that completes the dynamics. Top: Hindmarsh-Rose model can be obtained constraining the dynamics to a plane, the critical manifold in the phase plane is the classical N-shaped one, but presents nontrivial dynamics leading to rest-spike bistability. Bottom: the transcritical model obtained constraining the dynamics to a surface. The transcritical bifurcation is obtained when this surface is tangent to a line of folds at a point. This bifurcation is responsible for a singular homoclinic trajectory in the planar reduction.

The second rest-spike bistable phase portrait is the transcritical model of [29]. This model was obtained as a two-dimensional reduction of a conductance-based model that adds a slow calcium current to the Hodgkin-Huxley model [19]. The analysis of [29] rests on the presence of a transcritical bifurcation of the critical manifold. This bifurcation also directly relates to the mixed role of the slow variable as a source of both positive and negative feedback in the slow time-scale.

The transcritical bifurcation of the planar model [29] and the three-dimensional geometry of the present chapter can be connected considering how the planar reduction was obtained. Referring to our model (4.1) for simplicity, a planar reduction is obtained imposing an algebraic constraint between n and p, which can be interpreted as a path $n(s)$, $p(s)$ [82]. After obtaining a dynamic equation for s from a combination of $\dot{n}$ and $\dot{p}$, the reduced system is

$$\begin{aligned} \varepsilon \dot{v} &= i - i_{ion}(v, n(s), p(s)) \\ \dot{s} &= g(v, s) \end{aligned} \tag{4.17}$$

which is a slow-fast planar model. Its critical manifold is given by

$$i = i_{ion}(v, n(s), p(s)) \tag{4.18}$$

It corresponds to the intersection of the critical manifold of the larger system with the surface

$$n = n(s) \qquad p = p(s) \tag{4.19}$$

A transcritical bifurcation is obtained when

$$\begin{aligned} i_{ion} &= i \\ \frac{\partial i_{ion}}{\partial v} &= 0 \\ \frac{\partial}{\partial s}(i_{ion}(v, n(s), p(s))) &= \frac{\partial i_{ion}}{\partial n}\frac{dn}{ds} + \frac{\partial i_{ion}}{\partial p}\frac{dp}{ds} = 0 \end{aligned} \tag{4.20}$$

Geometrically these equations correspond to points on lines of folds of the critical manifold at which the two surfaces are tangent, as shown in figure 4.8. Indeed, vectors (δ_v, δ_p, δ_n) tangent to the critical manifold at a point verify

$$\frac{\partial i_{ion}}{\partial v}\delta_v + \frac{\partial i_{ion}}{\partial p}\delta_p + \frac{\partial i_{ion}}{\partial p}\delta_p = 0 \tag{4.21}$$

For the surface (4.19), being parametrised by s and v, its tangent space is generated by the two vectors

$$v_1 = \begin{pmatrix} 1 \\ 0 \\ 0 \end{pmatrix} \qquad v_2 = \begin{pmatrix} 0 \\ \frac{dp}{ds} \\ \frac{dn}{ds} \end{pmatrix} \tag{4.22}$$

At a point verifying (4.20) the two vectors (4.22) verify (4.21). Similar geometric constructions lead to the presence of a transcritical bifurcation when reducing the Hodgkin-Huxley model with increased potassium reversal potential, as well as when reducing the same model augmented with a calcium current, as done in [29].

An equivalent interpretation of how the transcritical bifurcation arises is that the path $(n(s), p(s))$ defining the surface (4.19) is tangent to the line of folds

$$i = i_{ion}(v, n, p) \qquad \frac{\partial i_{ion}}{\partial v}(v, n, p) = 0 \tag{4.23}$$

projected onto the n-p plane. This is the simplest example of how singularities can be generated from elementary catastrophes, the core idea in the path formulation of singularity theory [33, Ch.3 §12]. This is particularly interesting in view of [30], where singularity theory is used to obtain a global description of the critical manifolds of slow-fast planar systems relevant to neuronal dynamics. Two singularities play a prominent role: hysteresis, in connection with spiking, and winged cusp, for rest-spike bistability. Both these singularities can be realised as paths in the unfolding of the cusp catastrophe [33]. Interestingly, this bifurcation is often found in the fast subsystem of neuronal models (an early example being [104]), and it is typically related to the appearance and disappearance of bistability. For example, decreasing the sodium conductance in the Hodgkin-Huxley model leads to the appearance of this bifurcation and the same is achieved by reducing g_m in (4.1). The presence of this type of bifurcation in these models suggests that those singularities can arise from model reduction similarly to what happens in the transcritical case.

4.7 Conclusions

This chapter studied a simplified slow-fast model of neuronal activity that exhibits rest-spike bistability. The simplest physiological models of excitability include a fast-activating inward current and a slowly-activating outward current. This model adds a slowly-activating inward current to this basic motif. We think of this model as a core structure for the generation of multistability in more general and realistic conductance-based models. We speculate that similar results are possible using a slowly-inactivating outward current, which would have the same functional role of a slow positive feedback.

The geometry of this three-dimensional model was analysed using geometric singular perturbation theory. This geometry is rather simple, with the slow dynamics taking place on a classical N-shaped critical manifold. A saddle point on it plays a key role. Its stable manifold acts as separatrix, while its unstable manifold determines whether multiple attractors are present. Moreover, the same geometric picture captures different types of bistability, suggesting a common framework to study different phenomena important to neuronal dynamics.

The geometric picture studied in the present chapter is a starting point to analyse more complex patterns such as bursting. Often, this is qualitatively described as an oscillation between the two attractors of a rest-spike bistable system. Its generation interconnecting two subsystems builds on the picture developed in this chapter and it is the topic of the next one.

Appendix

4.A Persistence of a homoclinic trajectory

This appendix shows that under the assumption of transversality, the intersection of stable and unstable manifolds that leads to a singular homoclinic trajectory persists for $\varepsilon > 0$. This is done using the setting of [92] and in particular their results on maps defined by the flow of (4.1). We recast these results in the notation of section 4.4 and refer to the original work for details.

As in section 4.4, i_H is the value of i at which a singular homoclinic trajectory exists. We consider the reduced dynamics for this value of i, and fix a point x_u on the unstable manifold of x_m between x_m and $\mathcal{F}_l$. Similarly, we fix a point x_s on the stable manifold between $\mathcal{P}_l$ and x_m.

After a local change of coordinates we can find two neighbourhoods of these points, N_s and N_u, such that the critical manifold $\mathcal{C}_0$ corresponds to the plane $v = 0$. The intersections of these neighbourhoods with the planes $n = n_s$ and $n = n_u$ determine two surfaces Σ_s and Σ_u. Rotating n and p if necessary, we can assume that $\Sigma_u \cap \mathcal{C}_0$ intersects the unstable manifold of x_m transversally (in $\mathcal{C}_0$) and only at x_u, and similarly for $\Sigma_s \cap \mathcal{C}_0$. For fixed δ we let $N_\delta = (i_H - \delta,\, i_H + \delta)$ and consider $\Sigma_s \times N_\delta$ and $\Sigma_u \times N_\delta$. If δ is small enough, stable and unstable manifolds of $x_m(i)$ intersect transversally these extended neighbourhoods (in the critical manifold extend to include i). In the following we assume that N_s, N_u, N_δ are shrunk whenever necessary.

In section 4.3, we have characterized the stable manifold of x_m for small $\varepsilon > 0$, this is composed of a line on $\mathcal{C}_\varepsilon$ and the fibres based on it. In the limit $\varepsilon \to 0$, the singular stable manifold intersect Σ_s transversally along one of these fibres. Thus if ε and δ are small enough the same will be true for the stable manifold of $x_m(i)$ for fixed i and ε. Moreover, since at $\varepsilon = 0$, $i = i_H$ this intersection is a line of constant p, we can find a parametrization of it that has the form $p = p_s(v, i, \varepsilon)$. Similarly, the intersection of Σ_u with the unstable manifold of $x_m(i, \varepsilon)$ defines two functions $v_u(i, \varepsilon)$ and $p_u(i, \varepsilon)$.

Notice that in this section we use v and p to parametrize the two slices Σ_s and Σ_u, so that v preserves its nature of fast variable. This differs from the use of v and p to parametrize the critical manifold as done in section 4.3 and section 4.4.

We can now use the same construction of [92] to obtain a map $\Pi : \Sigma_u \to \Sigma_s$ corresponding to the action of the flow. This has the form

$$\Pi \begin{pmatrix} v \\ p \end{pmatrix} = \begin{pmatrix} R(v,p,i,\varepsilon) \\ G(v,p,i,\varepsilon) \end{pmatrix} \tag{4.24}$$

The function R is exponentially small in ε ($|R| + \|\nabla R\| < \exp(-c/\varepsilon)$) and in particular verifies

$$R(v,p,i,0) = 0 \tag{4.25}$$

G has the form

$$G = G_0(p) + \mathcal{O}(\varepsilon \ln(\varepsilon)) \tag{4.26}$$

where $G_0 : \Sigma_u \cap \mathcal{C}_0 \to \Sigma_s \cap \mathcal{C}_0$ is the map defined by the singular flow. Smooth dependence on i follows from standard results.

The only difference between this map and the Poincaré map defined in [92] is that we consider two different sections Σ_s and Σ_u rather than one.

Applying this map to $(v_u,\, p_u)$ we obtain the intersection of the unstable manifold of x_m with Σ_s

$$\Pi \begin{pmatrix} v_u \\ p_u \end{pmatrix} = \begin{pmatrix} R(v_u,p_u,i,\varepsilon) \\ G(v_u,p_u,i,\varepsilon) \end{pmatrix} \tag{4.27}$$

In this setting an intersection of stable and unstable manifolds corresponds to a solutions of

$$G(v_u,p_u,i,\varepsilon) = p_s(R(v_u,p_u,i,\varepsilon),i,\varepsilon) \tag{4.28}$$

where $v_u = v_u(i,\varepsilon)$ and $p_u = p_u(i,\varepsilon)$. Thus, we can define

$$P_u(i,\varepsilon) = G(v_u,p_u,i,\varepsilon) \qquad P_s(i,\varepsilon) = p_s(R(v_u,p_u,i,\varepsilon),i,\varepsilon) \tag{4.29}$$

and a homoclinic trajectory corresponds to $P_u - P_s = 0$.

At $\varepsilon = 0$

$$\begin{aligned} P_u(i,0) &= G_0(p_u(i,0)) \\ P_s(i,0) &= p_s(R(0,p_u(i,0),i,0),i,0) = p_s(0,i,0) \end{aligned} \tag{4.30}$$

and the existence of the singular homoclinic trajectory at $i = i_H$ means that

$$P_u(i_H,0) = G_0(p_u(i_H,0)) = p_s(0,i_H,0) = P_s(i_H,0) \tag{4.31}$$

Assuming that

$$\frac{\partial P_u}{\partial i}(i_H, 0) - \frac{\partial P_s}{\partial i}(i_H, 0) \neq 0 \tag{4.32}$$

an application of the implicit function theorem* guarantees the existence of a continuous functions $i_H(\varepsilon)$ such that $P_u(i_H(\varepsilon), \varepsilon) = P_s(i_H(\varepsilon), \varepsilon)$.

At $\varepsilon = 0$, $P_u(i, 0)$ is the intersection of the singular unstable manifold (after two jumps) with $\Sigma_s \cap \mathcal{C}_0$, while $P_s(i, 0)$ corresponds to the intersection of the stable manifold of the reduced flow and $\Sigma_s \cap \mathcal{C}_0$. Condition (4.32) corresponds to transversality of the intersection between the manifolds $p = P_s(i, 0)$ and $p = P_u(i, 0)$ in the extended neighbourhood $\Sigma_s \times N_\delta$. Since the invariant manifolds of $x_m(i)$ can be obtained applying the singular flow to these two sections, we see that condition (4.32) is equivalent to transversality of the intersection between the invariant manifolds of $x_m(i)$ on the critical manifold (where the unstable manifold has been continued past two jumps using the singular flow).

4.B Parameters

The analysis in sections 4.3 and 4.4 uses the following numerical values for the parameters of (4.1)

$$\begin{gathered} v_l = -.8, \quad gl = 2 \\ g_m = 4.4, \quad a_m = -.19, \quad b_m = .18 \\ g_n = 8.0, \quad a_n = -.16, \quad b_n = .29 \\ g_p = 2.0, \quad a_p = -.5, \quad b_p = .3 \\ \tau = 1.5 \end{gathered} \tag{4.33}$$

Parameters related to m, n and leak are approximated from those in [21] for the Morris-Lecar model in the case Hopf, after normalizing v between -1 and 1. Other parameters have been chosen to obtain the desired bistability.

*We need a relaxed version of the implicit function theorem since the dependence on ε is not smooth but only continuous, this is proven in [65].

Chapter 5

Bursting from interconnection

This chapter studies how bursting is generated by interconnecting two subsystems. Compared to other treatments of bursting here we want to highlight how the same structure can generate different bursting patterns. This fits well with the observation of the previous chapter that different rest-spike bistable diagrams can be obtained in the same geometric setting, and in turn using the same underlying structure.

Starting from the interconnection of a fast excitable system and a slower van der Pol-like oscillator, the focus is on how the two limits of the van der Pol oscillator lead to two different bursting patterns: square wave and parabolic. This complements the observation of the previous chapter on different rest-spike bistable diagrams, as well as other works on the transition between bursting and tonic spiking.

5.1 Introduction

Since the early day of neurophysiology several preparations showed a pattern consisting of packets of high-frequency spikes (bursts) followed by a period of relative inactivity. Bursting corresponds to the repetition of this pattern. Examples of bursting neurons can be found in the book [51, Ch.9] and the article [100].

In parallel with the experimental observations, a large number of researchers have developed and analysed mathematical models of bursting, ranging from high-dimensional multi-compartment conductance-based models [93] to minimalistic integrate-and-fire models [6, 87, 98]. Starting with the seminal works of Rinzel [80, 81], the main theoretical tool used in the analysis and classification of bursting is dissection of slow-fast models: The system is divided in two parts, a fast subsystem that can generate both active and rest states, and a slow one that modulates between the two. Based on this idea bursting systems started to be classified according to the bifurcations of the fast subsystem, eventually leading to the work of Izhikevich [49], who lists 16 possible types assuming a two-dimensional fast dynamics and 120 if this constraint is removed.

A difficulty with this approach is how to relate different types of bursters to experimental preparations, to the elements that are found in neurons, to the underlying biology. It is revealing in this sense to look at the first three open problems listed in the scholarpedia page about bursting [50]:

- *The complete classification of all electrophysiological types of bursters is still missing.*
- *There is no methodology of how to distinguish different topological types experimentally.*
- *The relationship between electrophysiology of a cell and the topological type of its bursting is not worked out.*

They all illustrate the difficulty of linking a mathematical theory of bursting to the biophysics of different experimental preparations. These questions go hand in hand with the problem of relating the components of a circuit to its external behaviour. They acquire increasing importance as we attempt to study how neuronal circuits, and even single neurons, can be robustly modulated. This is becoming always more important, as we accumulate evidence that neuronal systems can robustly change their state in response to external and internal stimuli, despite the presence of animal to animal variability, degenerate dynamics and homeostatic processes [66]. We believe that to address these questions it is necessary to move from the static classification of different bifurcation diagrams towards a more unifying view, in which the same elementary components generate different patterns modulating their parameters.

The present chapter tries to make a further step in this direction, continuing the line of work initiated in [19, 29, 30, 79]. In those works the elements found in many biological systems are abstracted to build simplified models or design circuits that can be easily modulated between different states. The generation of action potentials requires two key processes, a fast autocatalytic one which depolarises the cell (positive feedback), and a slower one that repolarises it (negative feedback). Those works use a repetition of this basic motif on a slower time-scale to generate bursting. A natural consequence of this structure is an easy way to transition between bursting and spiking: The latter is obtained reducing the influence of the slow positive feedback process.

Following these ideas naturally leads to models that have at least three distinct time-scales and four different variables, one for each functional role. However, the models in previous studies use only three variables, generating slow positive and negative feedback with a one-dimensional dynamics. This chapter continues the work initiated in the previous one, separating these two roles in two distinct dynamic variables. This is done proposing a model that has these four roles separated in four variables spanning three time-scales. Relaying on this slow-fast structure it is possible to analyse how different types of bursting can be generated by the resulting system.

In doing this we abandon the common three-variable structure used in most studies of bursting. Indeed, our model has a structure similar to the four-dimensional model of parabolic

bursting analysed by Rinzel and Lee [83]. Parabolic bursting is characterised by a spiking frequency that is low at the beginning and the end of the burst and higher in the middle part, resembling a parabola. At the core of its description there is the idea that bursting is obtained by the interaction of two subsystems. A fast one that generates action potentials in the presence of appropriate inputs and a slower one that generates oscillations driving the alternation of active and rest phases. As the generation of spikes uses fast positive and slow negative feedback, these same two elements, with slower dynamics, are used to generate slow waves. Thus, we can ultimately think of bursting as arising from the interaction of two oscillatory systems sharing a similar structure.

The main focus of this chapter will be on showing how this same interconnection can naturally generate another common pattern of spiking frequency, starting higher and decreasing monotonically, as typically observed in so-called square-wave bursters. Interestingly, a similar transition was already observed by Rinzel and Lee: They obtained parabolic bursting starting from a model that shows a monotonic decrease of frequency during the burst, the one developed by Plant [74] for the neuron R-15 in the abdominal ganglion of the sea slug *Aplysia Californica*[*].

The model of parabolic bursting in [83] uses a single compartment, with the two subsystems corresponding to two pairs of different currents: sodium and potassium for the fast oscillation, calcium and calcium-driven potassium for the slow oscillation. We can also think of the two subsystems as corresponding to two spatially distinct compartments of the same neuron. This structure is not uncommon in multi-compartment neuronal models. One classical example is the model of Pinsky and Rinzel [73] obtained as a reduction of the 19-compartment model proposed by Traub [94] for pyramidal cells of guinea pigs. Another example is the more recent model developed by Soto-Treviño and coworkers [88] to simulate neurons in the stomatogastric ganglion of lobsters. In both cases two compartments are used to model a single neuron. One compartment generates the action potential, the other is characterised by slower currents and generates slower waves. The former compartment is naturally identified with the standard motif of excitability, while the other contains its slower replication identified by [29, 30].

Further examples of two-compartment models exist in the context of conductance-based models. One example is the "ghostbursting" model of Doiron and co-workers [17]. Also that model suggests that different compartments can be associated to different time-scales: The ratio between conductances of fast and slow currents is much lower in the compartment modelling dendrites. However, the four elements discussed above cannot be readily found and the bursting dynamics is fairly different, suggesting that another mechanism underlies bursting generation in that model.

In the following we aim at capturing the essential elements present in the model developed by Pinsky and Rinzel, and the one by Soto-Treviño et al., favoring simplicity over verisimilitude.

[*]As a side note, experiments on this preparations show a parabolic type of bursting [86].

In this spirit, we only use two elements to obtain the basic motif, leading to a four-variable model. Moreover, we use piecewise-linear systems that admit an easy analytic treatment and are characterised by simple dynamics. The resulting model is piecewise-linear and has three distinct time-scales, a structure similar to the one studied in [23], where the authors focus on the appearance of mixed-mode-oscillations. To obtain this pattern that work considers the interconnection of two excitable subsystems in cascade. In contrast, in the model we analyse the two subsystems are in feedback, as it is common in multi-compartment models.

5.2 Structure and elements of the interconnection

The core interconnection studied in this chapter is illustrated in figure 5.1.

The first system (I) is a variation of the piecewise-linear version of the classical FitzHugh-Nagumo model (also known as McKean model [68])

$$\begin{aligned} \varepsilon \dot{v}_1 &= -k_1 v_1 + a_1 \Sigma(v_1) - w_1 + u_1 \\ \dot{w}_1 &= g_1 \Sigma(k_0(v_1 - v_0)) - w_1 \end{aligned} \tag{5.1}$$

where Σ is a piecewise-linear sigmoid-like function

$$\Sigma(x) = \begin{cases} 0 & \text{if} \quad x \leq 0 \\ x & \text{if} \quad 0 \geq x \leq 1 \\ 1 & \text{if} \quad x \geq 1 \end{cases} \tag{5.2}$$

The second equation models the dynamics of the so-called recovery variable. The dynamics is linear in the McKean model but we find it convenient to use a nonlinear expression reminiscent of the kinetics of a gating variable. For the other system (II) we use a piecewise-linear version

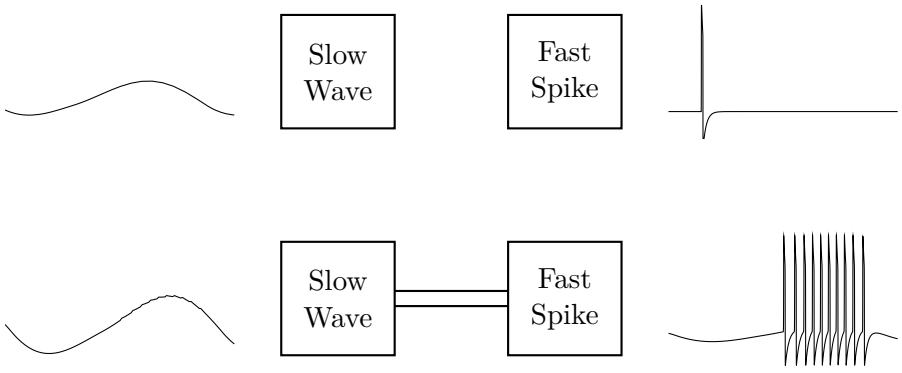

Figure 5.1 Interconnection used to generate bursting. The two systems in isolation correspond to a fast spiking one and a slower oscillatory one. When interconnected the slow waves drive bursts of action potentials.

of the van der Pol oscillator

$$\begin{aligned} \dot{v}_2 &= \lambda(-k_2 v_2 + a_2 \Sigma(v_2) - w_2 + u_2) \\ \dot{w}_2 &= \delta(g_2 v_2 - \bar{u}_2) \end{aligned} \tag{5.3}$$

In both cases the term $\Sigma(v_i)$ represents a positive feedback process while w_i corresponds to negative feedback.

Both systems contain small parameters (ε in (5.1) and δ in (5.3)) meant to represent the different time-scales present in neuronal models. These will be used to obtain singular limits of the equations. The additional parameter λ that appears in system II allows us to vary the time-scale of v_2, making it as fast as w_1 ($\lambda \approx 1$) or markedly slower ($\lambda \approx \delta$), leading to different pattern of bursting in the interconnected system. In terms of system II this passage corresponds to changing the waveform between the two limit of a relaxation oscillator and a harmonic one. In fact, the ratio λ/δ roughly corresponds to the parameter μ in the original van der Pol equation

$$\ddot{v} + \mu(v^2 - 1)\dot{v} + v = \bar{u} \tag{5.4}$$

Given this structure we think of v_2 as a voltage, with the desirable side-effect of suggesting a physical implementation for the system, even though it cannot be identified with the voltage of a compartment in a neuronal model.

Following these ideas and interpretation the natural input to system II would be a current, represented by u_2 in (5.3). However, also using the classical input to the van der Pol oscillator ($\bar{u}_2$ in (5.3)) is worth considering, since it leads to an interconnection that is simpler to analyse. Considering both possibilities leads to two interconnections, corresponding to two sets of constraints between the variables. The use of u_2 is modelled by

$$\begin{aligned} u_1 &= d_1(v_2 - v_1) + i_1 \\ u_2 &= d_2(v_1 - v_2) \\ \bar{u}_2 &= v_b \end{aligned} \tag{5.5}$$

while using $\bar{u}_2$ corresponds to

$$\begin{aligned} u_1 &= d_1(v_2 - v_1) + i_1 \\ u_2 &= 0 \\ \bar{u}_2 &= d_2(v_1 - v_2) + v_b \end{aligned} \tag{5.6}$$

This second case has a distinct advantage when $\lambda \approx 1$ and system II is a relaxation oscillator.

In both cases it is convenient to incorporate d_1v_1 and d_2v_2 in the linear term of the corresponding dynamics. Doing this (5.5) becomes

$$\begin{aligned} u_1 &= d_1v_2 + i_1 \\ u_2 &= d_2v_1 \\ \bar{u}_2 &= v_b \end{aligned} \tag{5.7}$$

while (5.6) becomes

$$\begin{aligned} u_1 &= d_1v_2 + i_1 \\ u_2 &= 0 \\ \bar{u}_2 &= d_2v_1 + v_b \end{aligned} \tag{5.8}$$

Thus, in both cases the coupling corresponds to a feedback interconnection of (5.1) and (5.3), with appropriate parameters and inputs.

Following these remarks the general form of the interconnected system is

$$\begin{aligned} \varepsilon\dot{v}_1 &= -k_1v_1 + a_1\Sigma(v_1) - w_1 + d_1v_2 + i_1 \\ \dot{w}_1 &= g_1\Sigma(k(v_1 - v_0)) - w_1 \\ \dot{v}_2 &= \lambda(-k_2v_2 + a_2\Sigma(v_2) - w_2 + u_2) \\ \dot{w}_2 &= \delta(g_2v_2 - \bar{u}_2) \end{aligned} \tag{5.9}$$

To keep these equations more compact it is convenient to introduce the functions

$$\begin{aligned} \phi_i(v_i) &= k_iv_i - a_i\Sigma(v_i) \\ w_\infty(v_1) &= g_1\Sigma(k_0(v_1 - v_0)) \end{aligned} \tag{5.10}$$

so that (5.9) becomes

$$\begin{aligned} \varepsilon\dot{v}_1 &= -\phi_1(v_1) - w_1 + d_1v_2 + i_1 \\ \dot{w}_1 &= w_\infty(v_1) - w_1 \\ \dot{v}_2 &= \lambda(-\phi_2(v_2) - w_2 + u_2) \\ \dot{w}_2 &= \delta(g_2v_2 - \bar{u}_2) \end{aligned} \tag{5.11}$$

Our objective in the remainder of the chapter is to use ideas similar to those in the previous one to understand how bursting is generated in the singular limit. Although we do not enter into the details of how trajectories persist outside of the singular limit, we remark that the piecewise-linear case makes the passage in principle easier. As noted in [76] in each zone of linearity the general theory can be specialised by requiring a linear slow manifold, making it unique. Explicit formulae to compute an approximation of these linear manifolds

are available in [59, Ch.2]. Moreover, persistence of singular trajectories involving both fast and slow parts, as a relaxation oscillation, is simplified in the present setting since there is no need for a local study around folds*.

In the following we try to keep the analysis general, but often impose relations between parameters that allow a simplified treatment. The figures shown are obtained using the values reported in appendix 5.A.

5.3 Fast system

The fastest singular limit of (5.11) is obtained for $\varepsilon = 0$ after the change of time $t = \varepsilon\tau$. In this limit only the first equation of system I (5.1) remains, making the dynamics independent from the value of λ. Slower variables can be grouped together in $j = u_1 - w_1$; using it the dynamics reduces to

$$\dot{v}_1 = j - \phi_1(v_1) \tag{5.12}$$

which is a piecewise-linear version of the usual fast limit of excitable systems. Depending on the two parameters of ϕ_1, k_1 and a_1, this system can be monostable or admit a zone of bistability. The latter case is the one we are interested in. It is realised when $a_1 > k_1$, which will always be assumed in the following.

Fixed points of (5.12) corresponds to solutions of $j = \phi_1(v_1)$. If $k_1 - a_1 < j < 0$ there are three solutions to this equation, two are stable fixed points, the other is unstable and

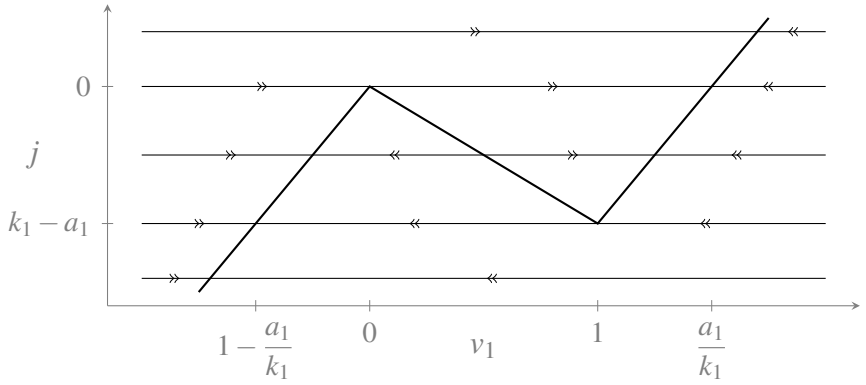

Figure 5.2 Dynamics of the fast system; the piecewise-linear curve $j = \phi_1(v_1)$ corresponds to fixed points, the linear branch in $0 < v_1 < 1$ corresponds to unstable ones, the other two branches are stable.

*This is mainly due to the fact that all critical manifolds in this chapter are normally hyperbolic everywhere. As shown in other studies [76], this limits the types of canards found in piecewise-linear systems similar to the ones studied in this chapter. Using the piecewise-linear framework, it is still possible to recover the same richness found in the smooth case introducing additional zones of linearity in the system [13, 84]. Since we are not directly interested in canard trajectories these cases are not considered in this chapter.

separates the basins of attraction of the two attractive fixed points. If j is outside the interval $[k_1 - a_1, 0]$ only one stable fixed point is present. At the two boundary values $j = k_1 - a_1$ and $j = 0$ there are two fixed points, one lies on a switching surface and is half stable and half unstable, the other is stable. If $j = 0$ the stable fixed point is at $v_1 = a_1/k_1 > 1$, while for $j = k_1 - a_1$ it is at $v_1 = 1 - a_1/k_1 < 0$. Figure 5.2 summarises this dynamics.

5.4 Slow system

As in the previous chapter, we can analyse the system referring almost exclusively to the slow limit obtained for $\varepsilon = 0$ in (5.11)

$$\begin{aligned} 0 &= -\phi_1(v_1) - w_1 + d_1 v_2 + i_1 \\ \dot{w}_1 &= w_\infty(v_1) - w_1 \\ \dot{v}_2 &= \lambda(-\phi_2(v_2) - w_2 + u_2) \\ \dot{w}_2 &= \delta(g_2 v_2 - \bar{u}_2) \end{aligned} \tag{5.13}$$

This system is constrained to the critical manifold

$$\varphi(x) := \phi_1(v_1) + w_1 - d_1 v_2 = i_1 \tag{5.14}$$

As usual, it corresponds to fixed points of the fast limit (5.12) studied in the previous section. The critical manifold can be divided in branches according to the nature of the corresponding fixed points. We will call $\mathcal{S}_a^{\pm}$ the two branches of attractive fixed points, with $\mathcal{S}_a^{+}$ being the one verifying $v_1 > 1$. $\mathcal{S}_r$ will stand for the repelling branch. These branches meet along the switching hyperplanes $v_1 = 0$ and $v_1 = 1$. Points on these hyperplanes play the same role of folds in smooth models.

We can now follow the same approach of the previous chapter. Deriving the constraint leads to an equivalent form of (5.13)

$$\begin{aligned} \frac{\partial \phi_1(v_1)}{\partial v_1}\dot{v}_1 &= d_1 \dot{v}_2 - \dot{w}_1 \\ \dot{w}_1 &= w_\infty(v_1) - w_1 \\ \dot{v}_2 &= \lambda(-\phi_2(v_2) - w_2 + u_2) \\ \dot{w}_2 &= \delta(g_2 v_2 - \bar{u}_2) \end{aligned} \tag{5.15}$$

In this case the derivative of ϕ_1 is not defined along the switching hyperplanes $v_1 = 0$ and $v_1 = 1$, making (5.15) a discontinuous system. Following the smooth case one could multiply

the vector field by $\frac{\partial \phi_1}{\partial v_1}$ obtaining

$$\begin{aligned} \dot{v}_1 &= d_1 \dot{v}_2 - \dot{w}_1 \\ \dot{w}_1 &= \frac{\partial \phi_1(v_1)}{\partial v_1}(w_\infty(v_1) - w_1) \\ \dot{v}_2 &= \frac{\partial \phi_1(v_1)}{\partial v_1}\lambda(-\phi_2(v_2) - w_2 + u_2) \\ \dot{w}_2 &= \frac{\partial \phi_1(v_1)}{\partial v_1}\delta(g_2 v_2 - \bar{u}_2) \end{aligned} \tag{5.16}$$

This changes the direction of trajectories on the repelling branch $\mathcal{S}_r$ but recovers existence and uniqueness of solutions almost everywhere (assuming Filippov's notion of solutions [24]). This is easily seen considering that on both sides of a switching hyperplane, which is parallel to $v_1 = 0$, both vector fields point towards the same side (since $\dot{v}_1$ is now continuous), so that the only possibility is crossing the hyperplane. The only exception are points at which

$$\dot{v}_1 = d_1 \dot{v}_2 - \dot{w}_1 = 0 \tag{5.17}$$

At points verifying this condition the vector field is tangent to the critical manifold. As in the smooth case these points are singular limits of canards [76]. They also appear at the boundary between zones in which the vector field points in opposite directions with respect to the switching hyperplane.

Excluding these points, reversing trajectories on $\mathcal{S}_r$ has the effect that only solutions in forward or backward time are possible for initial conditions on the switching surfaces $v_1 = 0$ and $v_1 = 1^*$. Jump points are those for which only solutions in backward time are possible. At them, singular trajectories leave the critical manifold and follow a fast fibre, arriving to a point on the opposite branch, as shown in figure 5.2. Points at which only solutions in forward time are possible correspond to points at which singular trajectories enter the slow manifold. From the viewpoint of the slow dynamics they are less interesting, since trajectories are repelled from them. The boundary between these two cases is formed by points that verify (5.17).

In the following it will be convenient to use directly (5.15), keeping in mind how singular solutions evolve once they reach a switching hyperplane. It is worth pointing out that (5.15) does not correspond to a unique singular limit as (5.13); trajectories of (5.15) are confined to level sets of

$$\varphi(x) = \phi_1(v_1) + w_1 - d_1 v_2 \tag{5.18}$$

and only when the dynamics is restricted to $\varphi(x) = i_1$ equivalence with (5.13) is obtained.

*There is also the possibility of sliding motion but this does not seem to be relevant for the original problem.

One aspect of the dynamics that is easily seen from (5.15) is that if $w_\infty(v_1)$ is constant on the stable branches $\mathcal{S}_a^\pm$ then the set $w_1 = w_\infty$ is attractive and invariant. This is the case if v_0 and k_0 in (5.10) verify $v_0 \geq 0$ and $k_0(1 - v_0) \geq 1$. Since these conditions are not unrealistic and simplify the analysis they will be assumed in the following.

Fixing one of the branches of the critical manifold, any of the variable v_1, w_1 or v_2 can be chosen and eliminated through the constraint $\varphi(x) = i_1$. As in the previous chapter, keeping v_1 as a variable allows the constraint to be solved globally. The easiest variable to eliminate is w_1. Doing so has the additional advantage that switching hyperplanes remain parallel to the axes, since v_1, v_2 and w_2 are used as coordinates. The resulting system is

$$\begin{aligned}
\frac{\partial \phi_1(v_1)}{\partial v_1}\dot{v}_1 &= d_1\dot{v}_2 - \dot{w}_1 \\
&= -w_\infty(v_1) + w_1 + d_1\lambda(-\phi_2(v_2) - w_2 + u_2) \\
&= -w_\infty(v_1) - \phi_1(v_1) + d_1 v_2 + i_1 + d_1\lambda(-\phi_2(v_2) - w_2 + u_2) \\
\dot{v}_2 &= \lambda(-\phi_2(v_2) - w_2 + u_2) \\
\dot{w}_2 &= \delta(g_2 v_2 - \bar{u}_2)
\end{aligned} \tag{5.19}$$

In these coordinates $w_1 = d_1 v_2 - \phi_1(v_1) + i_1$, and since $w_1 = w_\infty$ is invariant on the two branches $\mathcal{S}_a^\pm$, this expression gives an invariant set of (5.19) in $v_1 \notin (0,\, 1)$.

There is a further relation that can be imposed between parameters to simplify the analysis. Comparing $\phi_1(v_1) = k_1 v_1 - a_1 \Sigma(v_1)$ with $w_\infty(v_1) = g_1 \Sigma(k_0(v_1 - v_0))$ one notices that both Σ functions are constant on stable branches. Choosing these constants equal, i.e. $a_1 = g_1$, makes them cancel out, leading to the same systems on both branches. This reduces the number of linear systems that need to be considered, making the overall dynamics more symmetric.

It is useful to introduce few more functions to rewrite (5.19). In the case $\lambda \approx 1$ these are analogous to slow *i-v* curves as used in [79]

$$\begin{aligned}
\varphi_1(v_1) &= w_\infty(v_1) + \phi_1(v_1) - i_1 \\
\varphi_2(v_2, w_2) &= \phi_2(v_2) + w_2
\end{aligned} \tag{5.20}$$

Using these functions (5.19) can be rewritten in the compact form

$$\begin{aligned}
\frac{\partial \phi_1(v_1)}{\partial v_1}\dot{v}_1 &= d_1 v_2 - \varphi_1(v_1) + d_1\lambda(u_2 - \varphi_2(v_2)) \\
\dot{v}_2 &= \lambda(u_2 - \varphi_2(v_2, w_2)) \\
\dot{w}_2 &= \delta(g_2 v_2 - \bar{u}_2)
\end{aligned} \tag{5.21}$$

Using the relations imposed on v_0, k_0, a_1 and g_1, this reduces on stable branches to

$$\begin{aligned} k_1\dot{v}_1 &= d_1v_2 - k_1v_1 + i_1 + d_1\lambda(u_2 - \varphi_2(v_2, w_2)) \\ \dot{v}_2 &= \lambda(u_2 - \varphi_2(v_2, w_2)) \\ \dot{w}_2 &= \delta(g_2v_2 - \bar{u}_2) \end{aligned} \tag{5.22}$$

For this system $d_1v_2 - k_1v_1 = i_1$ is an invariant set. Indeed, defining $\xi = v_1 - \frac{d_1}{k_1}v_2$ (which is very close to being w_1) we have that

$$\dot{\xi} = \frac{i_1}{k_1} - \xi \tag{5.23}$$

On stable branches the two systems (5.21) and (5.22) are equivalent, and singular trajectories can be constructed looking at either. The only exceptions are those trajectories that pass through canards points. Since in the current setting these are exceptional trajectories, one can focus on (5.22) with appropriate reset conditions when the hyperplanes $v_1 = 0$ and $v_1 = 1$ are reached.

5.5 Parabolic bursting

The simplest case to analyse corresponds to $\lambda = \delta$. In this case the dynamics of v_2 is slower than that of w_1 and on the same time-scale of that of w_2, making the waveform of system II in isolation nearly harmonic. The type of behaviour obtained is similar, in structure and waveforms, to parabolic bursting as described in [83]. In this case (5.22) becomes

$$\begin{aligned} k_1\dot{v}_1 &= d_1v_2 - k_1v_1 + i_1 + d_1\delta(u_2 - \varphi_2(v_2, w_2)) \\ \dot{v}_2 &= \delta(u_2 - \varphi_2(v_2, w_2)) \\ \dot{w}_2 &= \delta(g_2v_2 - \bar{u}_2) \end{aligned} \tag{5.24}$$

which is again a slow-fast system. Since there is no need to refer explicitly to the fast system analysed in section 5.3, in the following fast and slow systems will refer to the two singular limits of (5.24). In the case $\lambda = \delta$, both inputs to system II (u_2 and $\bar{u}_2$) can be analysed in a similar way. Thus, we will consider the case that is more relevant for neuronal dynamics: $u_2 = d_2v_1$ and $\bar{u}_2 = v_b$.

5.5.1 Fast system

The fast system is obtained from (5.24) in the limit $\delta = 0$. This leads to the one dimensional system

$$k_1\dot{v}_1 = d_1v_2 + i_1 - k_1v_1 \tag{5.25}$$

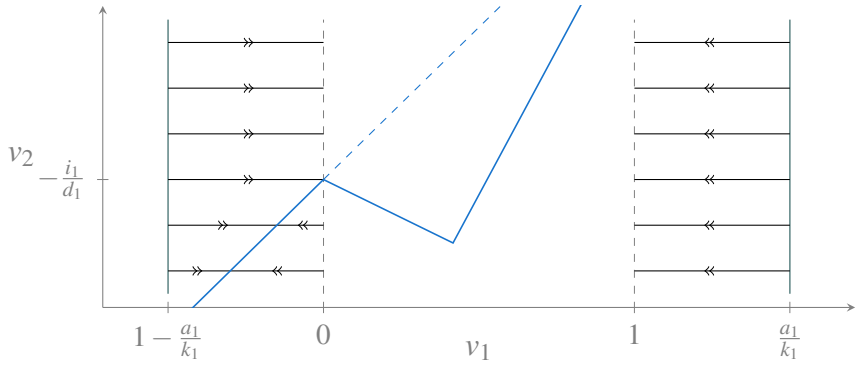

Figure 5.3 Dynamics of the fast system (5.25); the blue continuous line corresponds to $d_1 v_2 = \varphi_1(v_1)$, the dashed continuation corresponds to pseudo fixed points in $v_2 > -i_1/d_1$ ($\bar{v}_1$).

which has a fixed point at

$$\bar{v}_1 = \frac{d_1 v_2 + i_1}{k_1} \tag{5.26}$$

If this fixed point is on one of the two stable branches then it is attractive. This is not possible if

$$0 < \bar{v}_1 < 1 \quad \Leftrightarrow \quad -\frac{i_1}{d_1} < v_2 < \frac{k_1 - i_1}{d_1} \tag{5.27}$$

In this case we call $\bar{v}_1$ a pseudo fixed point, since in part of the state space the dynamics behaves as if it were there, but it is not a fixed point of the whole system. Indeed, when (5.27) is verified the dynamics tends towards $\bar{v}_1$ until it reaches one of the switching hyperplanes, at which point it jumps to the other branch. Repeating this process between the two stable branches generates a (singular) limit cycle corresponding to continuous spiking, as shown in figure 5.3. Assuming $v_2 > -\frac{i_1}{d_1}$ and starting at $v_1 = 1 - \frac{a_1}{k_1} < 0$ the trajectory goes towards $\bar{v}_1 \in [0, 1]$. Once it reaches $v_1 = 0$ it jumps on the other branch at $v_1 = \frac{a_1}{k_1} > 1$, at which point v_1 starts decreasing (always going towards $\bar{v}_1$), until it arrives to $v_1 = 1$. When this happens the trajectory jumps on the initial branch at $v_1 = 1 - \frac{a_1}{k_1}$ and the cycle repeats.

Thanks to the simplicity of the system, the period of one spike can be computed explicitly (at least in the singular limit $\varepsilon = 0$). This corresponds to the sum of the times the trajectory spends on each branch.

To compute it, we rewrite the fast system (5.25) using $\bar{v}_1$

$$\dot{v}_1 = \bar{v}_1 - v_1 \tag{5.28}$$

Its solution with initial condition v_i is

$$v_1(t) = \bar{v}_1 + (v_i - \bar{v}_1)\mathrm{e}^{-t} \tag{5.29}$$

and the time it takes to reach v_f is

$$T = \log\left(\frac{v_i - \bar{v}_1}{v_f - \bar{v}_1}\right) \tag{5.30}$$

This expression is valid if $v_i > v_f > \bar{v}_1$ or $v_i < v_f < \bar{v}_1$. This is the case for

$$\begin{aligned} v_i^- &= 1 - \frac{a_1}{k_1} < 0 = v_f^- \qquad (\mathcal{S}_a^-) \\ v_i^+ &= \frac{a_1}{k_1} > 1 = v_f^+ \qquad (\mathcal{S}_a^+) \end{aligned} \tag{5.31}$$

These values correspond to the initial and final point of the periodic trajectory on each branch. The time a trajectory spends on a branch is obtained substituting these values in (5.30), leading to

$$\begin{aligned} T^+ &= \log\left(\frac{k_1\bar{v}_1 + a_1 - k_1}{k_1\bar{v}_1}\right) = \log\left(1 + \frac{a_1 - k_1}{d_1 v_2 + i_1}\right) \\ T^- &= \log\left(\frac{a_1 - k_1\bar{v}_1}{k_1(1 - \bar{v}_1)}\right) = \log\left(\frac{a_1 - d_1 v_2 - i_1}{k_1 - d_1 v_2 - i_1}\right) \\ T_s &= T^+ + T^- \end{aligned} \tag{5.32}$$

The argument of the logarithm in (5.30) is easily seen to be monotonic in $\bar{v}_1$ since

$$\frac{d}{du}\left(\frac{v_i - u}{v_f - u}\right) = \frac{v_i - v_f}{(v_f - u)^2} \tag{5.33}$$

In particular, T is monotonically increasing if $v_i > v_f$, while it is monotonically decreasing if $v_f > v_i$. In both cases, it tends to infinity as $\bar{v}_1 \to v_f$ (from the appropriate side). Since $v_i^+ > v_f^+$ the time spent on T^+ increases as $\bar{v}_1$ increases, while T^- decreases as $\bar{v}_1$ increases. The total time T_s is the sum of these two terms. When $\bar{v}_1$ is close to v_f^- (v_2 close to $-\frac{i_1}{d_1}$) the term T^- dominates the sum, so that T_s is initially decreasing. Similarly, when v_2 is close to $\frac{k_1 - i_1}{d_1}$ the period tends to increase. The frequency $1/T_s$ for values of the parameters reported in appendix 5.A is shown in figure 5.4.

5.5.2 Slow system

For each value of the slow variables v_2 and w_2 the fast system (5.25) has a unique steady state, which can be a fixed point or a limit cycle. Thus, we can define a slow system, at least formally, considering the average effect of the fast variable v_1 on the slow variables v_2 and

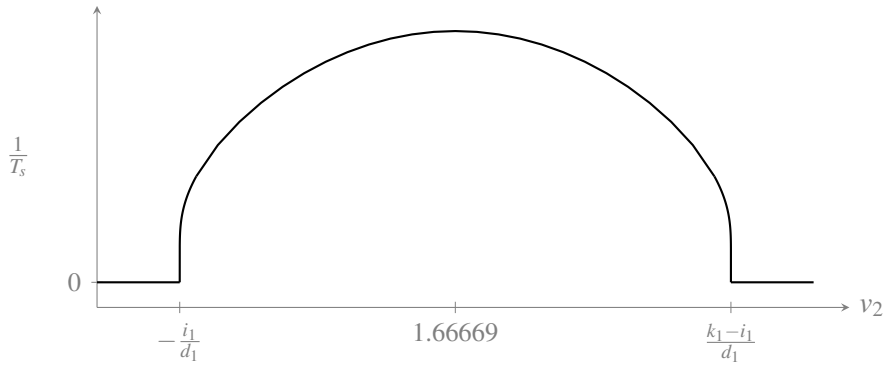

Figure 5.4 Spiking frequency as a function of v_2.

w_2 when v_1 is at steady state. In the case of fixed points this corresponds to setting v_1 at the value it takes at the fixed point. In correspondence of limit cycles, instead, we take the average of the dynamics of the slow variables over the limit cycle. In the latter case, since v_1 enters linearly in the equations for the slow variables, it is enough to compute the average of the trajectory over one cycle and substitute it in the equations.

Referring to (5.28), the integral of the trajectory between two points can be computed as

$$\begin{aligned}\int_0^T v_1(t)\,dt &= \int_{v_i}^{v_f} \frac{v}{\bar{v}_1 - v}\,dv \\ &= \int_{v_i}^{v_f} \frac{\bar{v}_1}{\bar{v}_1 - v} - 1\,dv \\ &= \bar{v}_1 \log\left(\frac{v_i - \bar{v}_1}{v_f - \bar{v}_1}\right) + v_i - v_f \\ &= \bar{v}_1 T + (v_i - v_f)\end{aligned} \tag{5.34}$$

where the last passage uses the expression for T in (5.30). Since $v_i^+ - v_f^+ = v_f^- - v_i^-$, the average over a cycle simplifies to

$$\frac{1}{T_s}\int_0^{T_s} v_1(t)\,dt = \frac{1}{T^+ + T^-}(\bar{v}_1 T^+ + v_i^+ - v_f^+ + \bar{v}_1 T^- + v_i^- - v_f^-) = \bar{v}_1 \tag{5.35}$$

Thus, in this case, the average of v_1 corresponds to the pseudo fixed point $\bar{v}_1$.

In conclusion, the slow system is obtained substituting $\bar{v}_1$ for v_1 in the equations for the slow variables. The resulting system has the same structure of system II in isolation, with

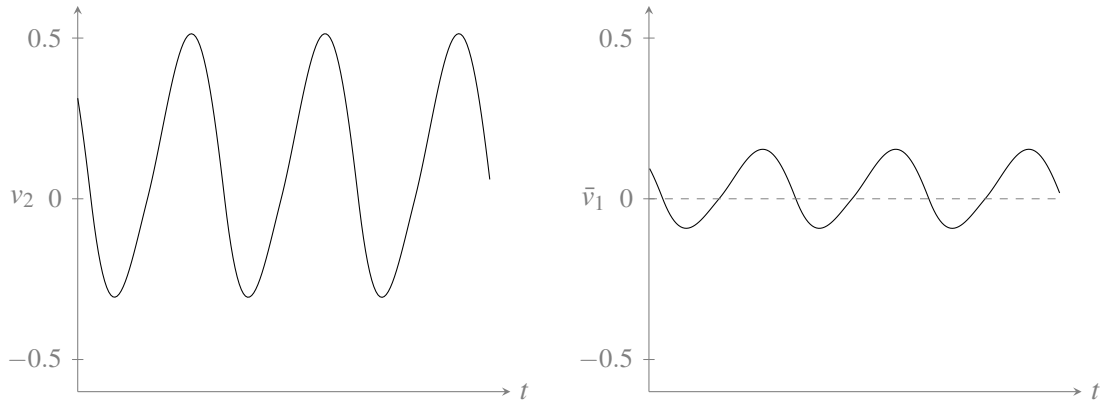

Figure 5.5 Slow wave in the averaged system. Left v_2, right $\bar{v}_1$. Approximations of trajectories of the full system can be obtained substituting spikes when $0 < \bar{v}_1 < 1$.

only the coefficient of v_2 different

$$\begin{aligned}\dot{v}_2 &= d_2\bar{v}_1 - \varphi_2(v_2, w_2)\\ &= d_2\frac{i_1}{k_1} + \frac{d_1 d_2}{k_1}v_2 - \varphi_2(v_2, w_2)\\ &= (\frac{d_1 d_2}{k_1} - k_2)v_2 + a_2\Sigma(v_2) - w_2 + d_2\frac{i_1}{k_1}\\ \dot{w}_2 &= g_2 v_2 - v_b\end{aligned} \tag{5.36}$$

Thus, it is possible to use our understanding of a van der Pol oscillator to analyse it. In particular, oscillations are possible only if $a_2 > k_2 - \frac{d_1 d_2}{k1}$, while if this quantity is negative the slow system (5.36) relaxes to a fixed point. A periodic motion obtained in the former case is shown in figure 5.5.

An approximation of the trajectories of the full system is obtained substituting spikes whenever v_2 is such that the corresponding attractor is a limit cycle. A simple graphical way to do this is to consider the trajectory of $\bar{v}_1$ and substitute spikes whenever $0 < \bar{v}_1 < 1$. The result is an approximation of the trajectory of v_1. Although a rigorous justification of this procedure is beyond the scope of this work, results on averaging in singularly perturbed systems [75, 103] and numerical results suggest that this approach is effective. Thanks to this approximation it is also possible to understand how the frequency varies during a burst. Indeed, the burst starts and terminates when $\bar{v}_1$ passes by the boundary value $\bar{v}_1 = 0$. Comparing figures 5.4 and 5.5 we see that the frequency of spiking increases and decreases with v_2, leading to the frequency variation typical of parabolic bursting, as shown in figure 5.6.

The construction above gives a natural way to understand the influence of different parameters on the behaviour of the system. The parameter i_1 is particularly interesting because it tends to have a very definite effect. Comparing how it enters in (5.26), (5.27) and (5.36) one notices that its effect on the slow dynamics is only a translation of w_2. At

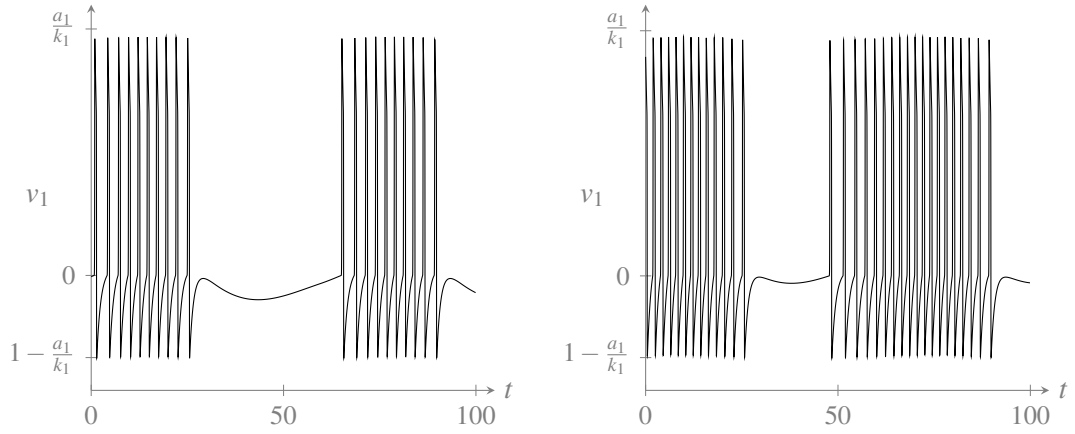

Figure 5.6 Bursting in (5.9) for $\lambda = \delta$; the two traces corresponds to different values of i_1, increasing it increases the duty cycle without altering other characteristics of the waveform.

the same time it controls the boundary value of v_2 at which the fast system starts spiking, equivalently, it translates $\bar{v}_1$ as a function of v_2. Thus, it can be used to control the duty cycle of the burst without altering other aspects of the waveform, as shown in figure 5.6. This simplicity comes at the price of a partial lost of similarity to neuronal systems. Indeed, a system similar to the FitzHugh-Nagumo model would be a more realistic choice for system II with a similar level of complexity. This would lead to a different slow system (5.36), with the dynamics of w_2 depending on w_2 itself. If this were the case, increasing i_1 would eventually lead to a fixed point in the slow system that could correspond to continuous spiking.

The role of other parameters can be understood in similar ways, although not all of them have such a definite effect. However, most parameters enter in only one of the two singular limits (5.25) and (5.36), making it easier to understand their influence. For instance, referring to (5.36), it is easily seen that a_2 can control if the slow system oscillates or relaxes to a stable fixed points, which, in turn, controls if the interconnection spikes or bursts.

5.6 Square-wave bursting

In this section we consider how system (5.11) can generate square-wave bursting. This pattern is obtained using $\delta \ll \lambda \approx 1$, which corresponds to the dynamics of v_2 being similar, in terms of time-scales, to the one of w_1. In this case the dynamics of w_2 is slower than that of v_2, making system II a relaxation oscillator.

The dynamics on stable branches of the critical manifolds is given by

$$\begin{aligned} k_1\dot{v}_1 &= d_1 v_2 - k_1 v_1 + i_1 + d_1(u_2 - \varphi_2(v_2, w_2)) \\ \dot{v}_2 &= u_2 - \varphi_2(v_2, w_2) \\ \dot{w}_2 &= \delta(g_2 v_2 - \bar{u}_2) \end{aligned} \tag{5.37}$$

In this configuration there is a clear advantage in using $u_2 = 0$ and $\bar{u}_2 = d_2 v_1 + v_b$. This leads to the fast limit being a cascade interconnection, with system II driving system I (in this section fast and slow systems refer to the two singular limits of (5.37)). This simplification comes at the price of a possible loss of similarity with neuronal models. However, the case of diffusive coupling leads to qualitatively similar dynamics, although it does not allow a similar analytic treatment.

5.6.1 Fast system as a cascade

In the simpler case $u_2 = 0$ the equations reduce to

$$\begin{aligned} k_1 \dot{v}_1 &= d_1 v_2 - k_1 v_1 + i_1 + d_1(u_2 - \varphi_2(v_2, w_2)) \\ \dot{v}_2 &= -\varphi_2(v_2, w_2) \\ \dot{w}_2 &= \delta(g_2 v_2 - d_2 v_1 - v_b) \end{aligned} \tag{5.38}$$

As in the previous section we analyse in sequence the two singular limits.

Fast sytsem

The fast limit of (5.38) is

$$\begin{aligned} k_1 \dot{v}_1 &= d_1 v_2 - k_1 v_1 + i_1 - d_1 \varphi_2(v_2, w_2) \\ \dot{v}_2 &= -\varphi_2(v_2, w_2) = -\phi_2(v_2) - w_2 \end{aligned} \tag{5.39}$$

The dynamics of v_2 is one dimensional. Its behaviour is the usual one found in the fast limit of excitable systems, for example the one studied in section 5.3. If a_2 in (5.10) is large enough ϕ_2 is N-shaped. In this case, depending on w_2, the system can have one, two or three fixed points.

Fixing v_2 at a steady-state value $\bar{v}_2$, the equation for v_1 becomes

$$k_1 \dot{v}_1 = d_1 \bar{v}_2 - k_1 v_1 + i_1 \tag{5.40}$$

This is the same as (5.25) studied in section 5.5.1. As in that case, $\bar{v}_1 = (d_1 \bar{v}_2 + i_1)/k_1$ defines a fixed point. This cannot be reached if it lies on the unstable branch $\mathcal{S}_r$

$$0 < \bar{v}_1 < 1 \quad \Leftrightarrow \quad -\frac{i_1}{d_1} < \bar{v}_2 < \frac{k_1 - i_1}{d_1} \tag{5.41}$$

in which case the corresponding steady state is a limit cycle.

The complete two-dimensional dynamics is obtained combining these two and can be represented on the v_1-v_2 plane as in figure 5.7. When the dynamics of v_2 is monostable it converges to a fixed value. In this case v_1 converges to the corresponding attractor, leading

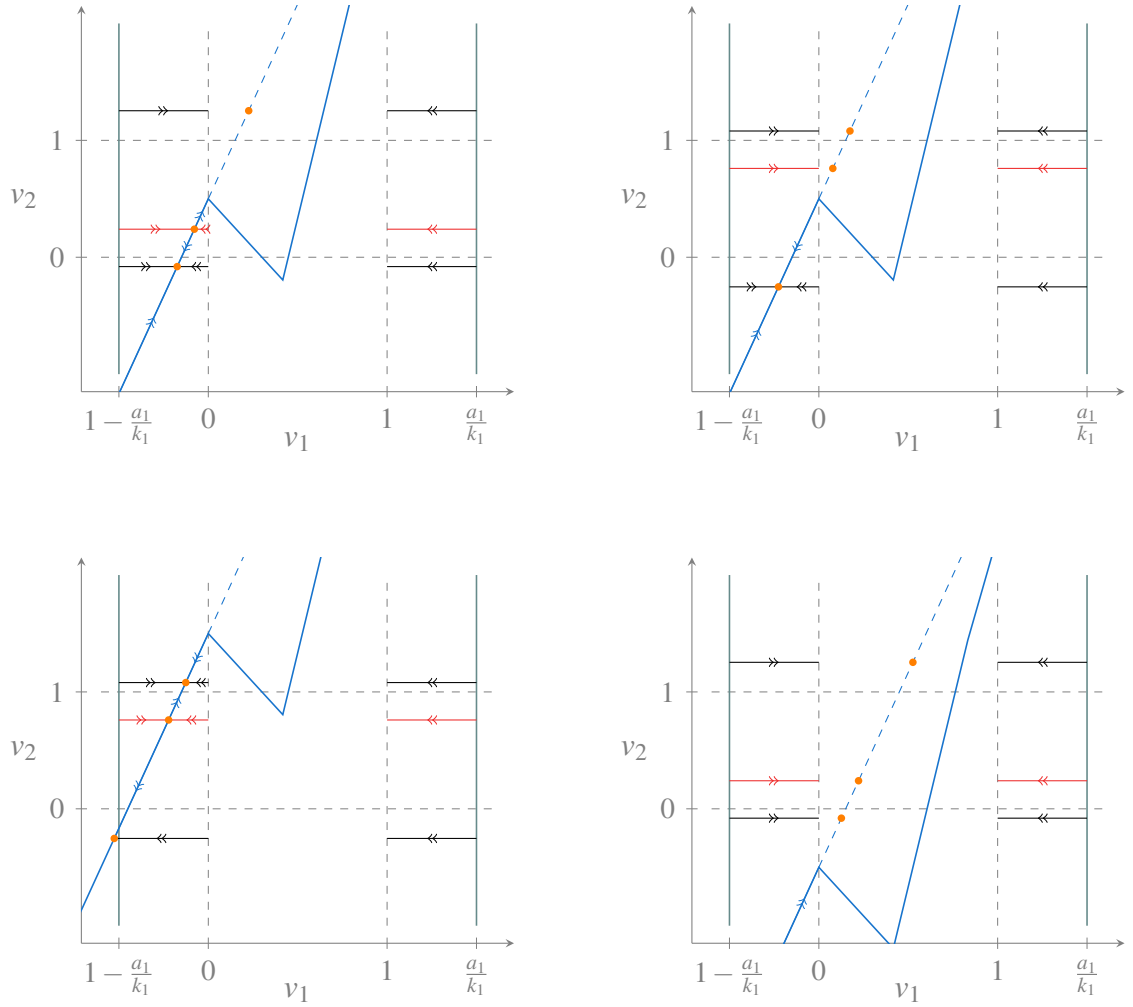

Figure 5.7 Bistability in the fast system on $\mathcal{S}_a^{\pm}$ induced by driving system I with the fast part of system II. The blue continuous line is $d_2 v_1 = \varphi_1(v_1)$, the blue dashed line is the invariant line $d_1 v_2 - k_1 v_1 = i_1$ (the two lines coincide on $\mathcal{S}_a^-$). Orange points correspond to (pseudo) fixed points; red trajectories correspond to unstable fixed points of system II and form separatrices in state space.

to a unique steady state for the fast system (5.39). When the dynamics of v_2 is bistable the three fixed points correspond to three steady states. The unstable fixed point leads to a separatrix in state space. The other two fixed points generate two attractors of the fast system (5.39).

Figure 5.7 shows the different possible combinations of limit cycles and fixed points for steady states of (5.39). They can all be obtained varying i_1 and w_2. The effect of these two parameters is easily understood referring to figure 5.7. The equation

$$w_2 = -\phi_2(\bar{v}_2) \tag{5.42}$$

shows that w_2 determines the values $\bar{v}_2$; these correspond to the horizontal lines on which (pseudo) fixed points lie. The applied current i_1 translates the line

$$d_1 v_2 - k_1 v_1 = i_1 \tag{5.43}$$

The intersection of this line with $v_2 = \bar{v}_2$ determines the value of $\bar{v}_1$. Finally, the position of these fixed points determines the type of attractor.

The relation between $\bar{v}_1$ and these two parameters can also be obtained directly composing steady states:

$$w_2 = -\phi_2(\bar{v}_2) = -\phi_2\left(\frac{k_1 \bar{v}_1 - i_1}{d_1}\right) \tag{5.44}$$

Assuming ϕ_2 N-shaped, then once again we see that the value of w_2 determines the number of fixed points of v_2, $\bar{v}_2$, which in turn determine the values $\bar{v}_1$ that verify (5.44). Given this structure, boundaries of bistability can be computed looking only at the dynamics of v_2. They correspond to parameter values at which v_2 has a half-stable fixed point on $v_2 = 0$ or $v_2 = 1$.

For periodic solutions it is possible to compute the frequency of spiking. This computation follows the same lines of what done in the previous section, with a relation to $\bar{v}_2$ similar to the one in figure 5.4. A useful observation in the present setting is that along stable branches of steady states the relation between $\bar{v}_2$ and w_2 is monotonically decreasing. Thus, the relation between spiking frequency and the only slow variable w_2 is inverted compared to the one between frequency and $\bar{v}_2$. In particular, if the family of stable periodic solutions arrives to $\bar{v}_2 = -i_1/d_1$, near this value increasing w_2 decreases the spiking frequency.

Slow system

Contrary to the case of section 5.5, it is not possible to define a global slow system in this case because of the presence of mulitstability. However, restricting our attention to only one branch of solutions, it is possible to understand the effect of the slow dynamics. This follows the same reasoning of the previous section: We consider the average effect of the fast variables v_1 and v_2 on the dynamics of the only slow variable w_2.

On a family of fixed points this amounts to assume that all fast variables are at their steady-state value, leading to the constrained system

$$
\begin{aligned}
w_2 &= -\phi_2\left(\frac{k_1\bar{v}_1 - i_1}{d_1}\right) \\
\dot{w}_2 &= g_2\bar{v}_2 - d_2\bar{v}_1 - v_b \\
&= g_2\frac{k_1\bar{v}_1 - i_1}{d_1} - d_2\bar{v}_1 - v_b \\
&= \frac{g_2k_1 - d_1d_2}{d_1}\bar{v}_1 - (v_b + g_2\frac{i_1}{d_1}) \\
&= \frac{g_2k_1 - d_1d_2}{d_1}(\bar{v}_1 - \frac{d_1v_b + g_2i_1}{g_2k_1 - d_1d_2})
\end{aligned}
\tag{5.45}
$$

This is a one-dimensional system whose behaviour is determined by the value of $\frac{d_1v_b+g_2i_1}{g_2k_1-d_1d_2}$. If this quantity is chosen so that $\dot{w}_2$ is never zero along the whole branch of fixed points, then the slow dynamics will just drift in a monotonic fashion.

Along a family of limit cycles we proceed as in the previous section, averaging fast variables. The same reasoning of section 5.5 leads to the conclusion that also along family of periodic solutions the slow drift can be quantified using (5.45). As already remarked attempting a rigorous justification of this averaging procedure is beyond the scope of this work, although other results [75, 103] and numerical simulations support its validity.

Comparing (5.45) with (5.37) reveals that this is the same slow system one would obtain from (5.37) ignoring reset conditions. As in the previous case this is a consequence of the specific structure of the system and choice of parameters, as well as the symmetry of the dynamics on the two stable branches. Thanks to these simplifications the slow drift along a family of solution can be easily quantified.

Combining slow dynamics and the characterisation of steady states (5.44) it is possible to understand the dynamics (5.38). In particular, if ϕ_2 is N-shaped the fast system (5.39) has two stable branches of steady states. Correspondingly, the slow dynamics (5.45) resembles the one of a relaxation oscillator, and if appropriate parameters are chosen it can lead to bursting.

The most relevant case is the one summarised in figure 5.8, in which the line $\bar{v}_1 = 0$ intersects the the unstable branch of the fast-system steady states, corresponding to the line (5.44). In this case one family of attractors is composed of fixed points, while the other corresponds to limit cycles.

We want to choose v_b so that the only fixed point of the slow system (5.45) is on the unstable branch of steady states. From (5.44), the unstable branch of steady state corresponds to the condition

$$
0 < \frac{k_1\bar{v}_1 - i_1}{d_1} < 1 \qquad \Leftrightarrow \qquad \frac{i_1}{k_1} < \bar{v}_1 < \frac{d_1 + i_1}{k_1}
\tag{5.46}
$$

The only fixed point of the slow system is given by (5.45)

$$\bar{v}_1 = \frac{d_1 v_b + g_2 i_1}{g_2 k_1 - d_1 d_2} \tag{5.47}$$

Using these two conditions allows us to choose v_b as desired.

Assuming further that*

$$g_2 k_1 - d_1 d_2 > 0 \tag{5.48}$$

we see that the slow dynamics (5.45) is such that w_2 decreases along the family of stable fixed points ($\bar{v}_1 < \frac{d_1 v_b + g_2 i_1}{g_2 k_1 - d_1 d_2}$) while it increases along the family of stable limit cycles ($\bar{v}_1 > \frac{d_1 v_b + g_2 i_1}{g_2 k_1 - d_1 d_2}$). Referring to figure 5.8 this shows that on each family the slow dynamics drifts towards the end of the branch.

The last points that would require further attention are the transition at the end of these two branches. Avoiding a detailed study of these transitions, it is intuitively clear what happens: Trajectories near these points behave like the analogous case in a standard relaxation oscillator, they are dominated by the fast dynamics (5.39) and quickly reach the other branch of attractors.

To summarise, a trajectory of (5.38) is quickly attracted by one of the two branches of stable steady states; it follow it until the end, at which point the trajectory jumps towards the opposite branch. Repeating this process generates a periodic motion corresponding to bursting.

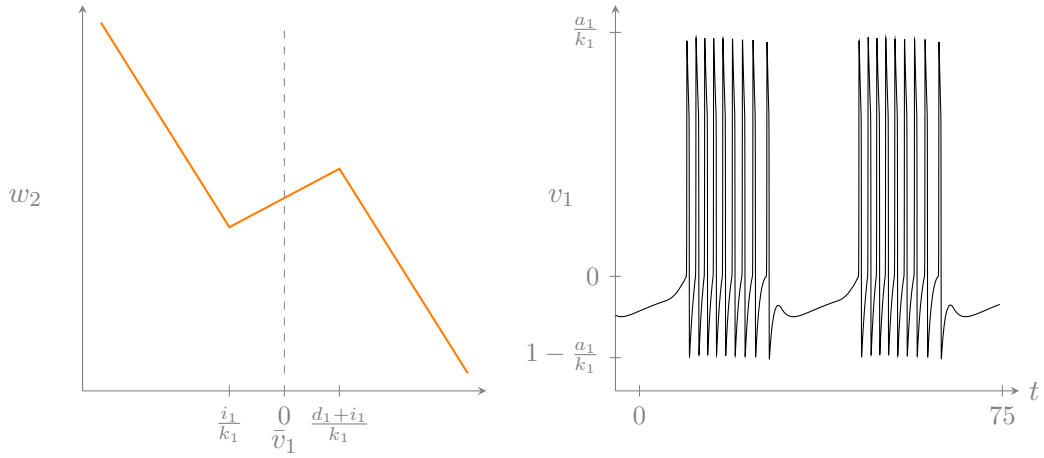

Figure 5.8 Bursting in (5.9) for $\lambda = 1$. Left: steady-state characteristic (5.44), points in $\bar{v}_1 < 0$ correspond fixed points, those in $\bar{v}_1 > 0$ correspond limit cycles; the three zones of linearity correspond to different stability properties with points on lines of negative slope being stable attractors. Right: time course of v_1.

*This condition is automatic if we consider the original interconnection (5.6).

Along the branch of limit cycles the dynamics of w_2 is monotonically increasing, leading to a decrease in spiking frequency during the burst, the same pattern observed in square wave bursting. Indeed, the dynamics just described is not too different from the description of square wave bursting in other models, for example [30]. An example waveform is shown in figure 5.8.

5.6.2 Diffusive coupling

Using u_2 rather than $\bar{u}_2$ as input to system II is equivalent to diffusive coupling between the two systems as in multi-compartment neuronal models. Using it the dynamics (5.37) becomes

$$\begin{aligned} \frac{\partial \phi_1(v_1)}{\partial v_1}\dot{v}_1 &= d_1 v_2 - \varphi_1(v_1) + d_1(d_2 v_1 - \varphi_2(v_2, w_2)) \\ \dot{v}_2 &= d_2 v_1 - \varphi_2(v_2, w_2) \\ \dot{w}_2 &= \delta(g_2 v_2 - v_b) \end{aligned} \tag{5.49}$$

On stable branches it reduces to

$$\begin{aligned} k_1\dot{v}_1 &= d_1 v_2 - k_1 v_1 + i_1 + d_1(d_2 v_1 - \varphi_2(v_2, w_2)) \\ \dot{v}_2 &= d_2 v_1 - \varphi_2(v_2, w_2) \\ \dot{w}_2 &= \delta(g_2 v_2 - v_b) \end{aligned} \tag{5.50}$$

Letting δ go to zero in this system yields the fast limit

$$\begin{aligned} k_1\dot{v}_1 &= d_1 v_2 - k_1 v_1 + i_1 + d_1(d_2 v_1 - \varphi_2(v_2, w_2)) \\ \dot{v}_2 &= d_2 v_1 - \varphi_2(v_2, w_2) \end{aligned} \tag{5.51}$$

Which can be studied with ideas similar to the ones of the previous section and the previous chapter, which rest on isolating invariant zones on the v_1-v_2 plane.

Fixed points of (5.51) can be studied graphically, as shown in figure 5.9, since they correspond to intersections of the two lines

$$\begin{aligned} d_1 v_2 &= \varphi_1(v_1) \\ d_2 v_1 &= \varphi_2(v_2, w_2) \end{aligned} \tag{5.52}$$

On the stable branches $\mathcal{S}_a^{\pm}$ the first equation reduces to the equation for the invariant line $k_1 v_1 - d_1 v_2 = i_1$.

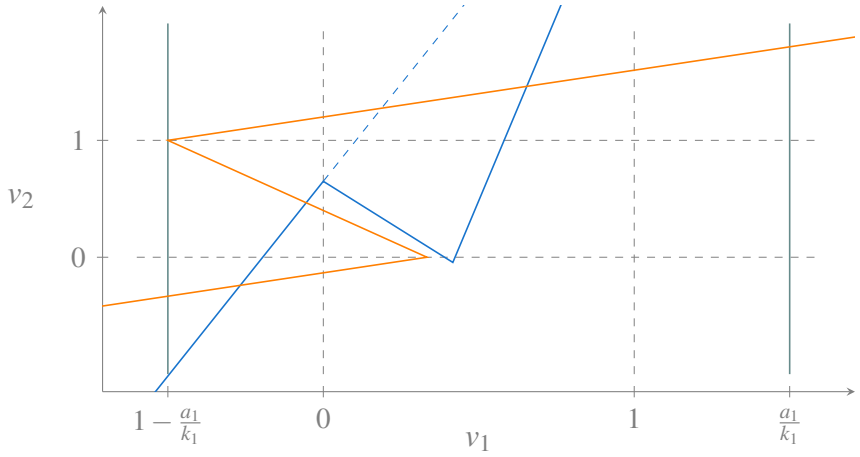

Figure 5.9 Fixed points of the fast system (5.51) as intersection of the steady-state curves (5.52). The blue curve, $d_1 v_2 = \varphi_1(v_1)$, is translated (vertically) by i_1, while the orange curve, $d_2 v_1 = \varphi_2(v_2, w_2)$, is translated (horizontally) by w_2; the dashed blue line is the continuation of the invariant line $k_1 v_1 - d_1 v_2 = i_1$, its intersection with $d_2 v_1 = \varphi_2(v_2, w_2)$ determines pseudo fixed points of the linear systems on stable branches.

Stability properties of the fixed points are best understood using $\xi = v_1 - \frac{d_1}{k_1} v_2$ in place of v_1, since the corresponding system is triangular

$$\begin{aligned} k_1 \dot{\xi} &= i_1 - k_1 \xi \\ \dot{v}_2 &= d_2 \xi + \frac{d_1 d_2}{k_1} v_2 - \phi_2(v_2) - w_2 \end{aligned} \tag{5.53}$$

Its eigenvalues can be easily computed. One of them is always -1, reflecting the presence of the attractive invariant line $\xi = i_1/k_1$. The other one is $\frac{d_1 d_2 - \kappa k_1}{k_1}$ where κ is the coefficient of v_2 in ϕ_2, which depends on v_2 itself since the function is piecewise-linear. Considering that $d_2 > 0$ we have for the sign of the second eigenvalue

$$\frac{d_1 d_2 - \kappa k_1}{k_1} \gtrless 0 \quad \Leftrightarrow \quad \frac{d_1}{k_1} \gtrless \frac{\kappa}{d_2} \tag{5.54}$$

This corresponds to a condition on the slope of the two lines $k_1 v_1 - d_1 v_2 = i_1$ and $\varphi_2(v_2, w_2) = d_2 v_1$ at the point they intersect. For example, in figure 5.9, of the two fixed points on $\mathcal{S}_a^-$ the one in $v_2 < 0$ is stable while the other is unstable.

Having understood the structure of (pseudo) fixed points, the next step is to understand the structure of steady states, which can include limit cycles. A natural approach is to follow the same path of the previous section and the previous chapter, and determine a separatrix that divides two invariant zones. Attempting this leads to transcendental equations that do not seem to admit an easy analytic treatment. However, numerical experiments reveal a structure similar to the one of the previous case and the one treated in the previous chapter.

For a range of values of w_2 the fast system (5.51) is bistable and different combinations of fixed points and limit cycles are possible. This bistability corresponds to an N-shaped steady-state characteristic with respect to the slow variable w_2, as in figure 5.8. Once this is established the analysis continues as before, leading to bursting as a relaxation oscillation between a branch of fixed points and a branch of limit cycles.

5.7 Tonic spiking

Finally, a short comment on how tonic spiking can be generated in the coupled system (5.11). Based on the analysis of the previous sections, it can be obtained if the slow dynamics evolves towards a spiking limit cycle. In the same spirit of [30, 79], this can be achieved varying the coefficient associated with the source of slow positive feedback: a_2. In terms of the dynamics of system II this corresponds to reducing the action of the active component in a van der Pol oscillator, leading to a system with a unique fixed point.

In the case $\lambda = \delta$ this corresponds to an averaged system (5.36) which has only one family of stable fixed points. Choosing v_b so that the slow dynamics has a fixed point with $\bar{v}_1$ between 0 and 1 achieves the desired effect. The frequency of the corresponding attractor can be approximated using the computation of the period in section 5.5.

In the case $\lambda = 1$ changing a_2 leads to a monotonic ϕ_2 and consequently to a fast system on $S_a^{\pm}$ that is not bistable. In this case it is possible to identify a unique stable steady state for each value of w_2, obtaining a global averaged system. Setting up this system so that it tends to a fixed point that corresponds to spiking achieves the desired behaviour.

5.8 Conclusion

The purpose of this chapter was to show how the interconnection of two systems, with different time-scales but similar structures, permits the generation of different types of bursting whose properties can be modulated. We think of this interconnection as the analogue of the one studied in chapter 3 in the context of resonant systems. In that sense this chapter is the counterpart of that one in the context of excitable systems. Here we aimed to study how the simplest excitable systems can be interconnected to obtain bursting, and how parameters in each of them influence the dynamics of the interconnection.

In both chapters we used techniques which are typical of the corresponding field, at times enriching them with external influences. Results of this chapter in particualar highlight possibilities for further progress in this context. Our use of averaging was mostly empirical, its effectiveness calls for a more thorough analysis of this procedure. A critical point we have ignored is that the families of limit cycles we considered do not necessarily have bounded period, but can terminate in a homoclinic trajectory. Another question related to this procedure is the computation of the number of spikes in a burst. The fact that we could

understand duty cycle of the burst and frequency variation of the spikes suggests that also the number of spikes in a burst could be approximated with similar methods.

In terms of neuronal dynamics, a key message of this chapter is that both parabolic and square-wave bursting, two patterns usually studied in isolation, can be generated by a common structure. These results naturally complements the ones of the previous chapter about the possibility of obtaining multiple types of rest-spike bistable bifurcation diagrams and the works on the transition between bursting and tonic spiking mentioned in the last section. Taken together we think of all these efforts as a way to build a unified view of neuronal activity, in which different patterns are generated modulating a unique structure. This is a natural starting point to study neuromodulation in single neurons and a step towards understanding how modulation affects networks.

Appendix

5.A Parameter values

Throughout the chapter all figures were obtained using the following parameters

$$\begin{gathered} k_1 = 1 \quad a_1 = 1.5 \quad d_1 = .3 \\ g_1 = 1.5 \quad k_0 = 2 \quad v_0 = .5 \\ k_2 = .75 \quad a_2 = 1 \quad d_2 = .3 \quad g_2 = 1 \end{gathered} \tag{5.55}$$

In all simulations $\epsilon = 1e-2$, in section 5.5 $\delta = \lambda = 1e-1$ while in section 5.6 $\delta = 5e-2$ ($\lambda = 1$). The change in δ was used to keep the period of bursting similar in the two sections.

Chapter 6

Conclusions

The purpose of this thesis was to study two basic interconnections that arise in the analysis and design of physical systems characterised by resonant or excitable behaviour. The Duffing oscillator is the canonical model of nonlinear resonance. The interconnection of two of these oscillators was studied in chapter 3, in the context of vibration absorption. The archetype mathematical model of excitability is the FitzHugh-Nagumo model, also known as the Bonhoeffer-van der Pol model. Chapter 5 studied how to generate bursting interconnecting two such models. We see those two interconnections as the starting point of any interconnection theory of oscillatory systems and more generally non-equilibrium systems.

In chapter 3, the main focus was the analysis of detached resonance curves: families of solutions isolated from a main one. In contrast to earlier numerically-based parametric studies, the use of singularity theory identifies an organising centre for the appearance of these solutions. Their algebraic characterisation in terms of isolas, simple bifurcations and asymmetric cusps can be further studied quantitatively using numerical techniques. Thanks to this it was possible to characterise the appearance of this adverse dynamics with respect to all design parameters, a first step towards an improved design of the absorber.

A natural continuation of this work consists in using the characterisations of singularity theory to obtain constructive principles that can be exploited during design. A development in this direction is presented in the follow-up work [36], not included in this dissertation. This work studied the appearance of detached resonance curves in one-degree-of-freedom systems using their characterisation through singularity theory. After the analytical study of these solutions, it is noted how they can be related directly to the damping element: They correspond to amplitudes that are maxima, minima and zero crossings of an averaged version of the damping. While that observation was made a posteriori in that study, it can also be derived combining averaging and singularity theory, as shown in appendix 6.A. This gives a first illustration of how further efforts starting from singularity theory can lead to constructive principles for the design of nonlinear resonances.

Chapters 4 and 5 studied how to generate bursting from the interconnection of two subsystems. The first step was studying rest-spike bistability in chapter 4, augmenting the classical motif of excitability with a source of slow positive feedback. The analysis of the resulting model was largely reduced to phase-plane analysis, allowing the study of this bistability from a geometric viewpoint. Building upon this study, chapter 5 analysed the interconnection of two piecewise-linear systems, one fast and excitable, the other slower and similar to a van der Pol oscillator. This interconnection naturally generates bursting. The primary objective of the chapter was to show how different patterns of activity, usually studied in isolation, can all be generated by the same interconnection.

In building these systems our main drive came from ideas connected to positive and negative feedback in different time-scales. A natural challenge is to leverage these concepts to arrive to quantitative methods that would allow us to deal with more realistic models of neuronal activity, often characterised by a large number of ion channels. While some attempts in this direction have been made [18], we still lack a methodology to study quantitatively how different patterns of activity are influenced by the different currents present in large models.

An important topic that emerges from this thesis is the interconnection of excitable and resonant systems. This is a context in which ideas from the different chapters of this thesis could be combined. To develop this topic, it is natural to start from applications that can furnish concrete examples and at the same time would benefit from a deeper understanding of this mixed interconnection.

Neuro-motor control and robotics are natural application areas, especially in the context of locomotion. The interaction of mechanical elements with the neuronal circuits that control them is of interest in biology and an inspiration in robotics. This interaction naturally calls for an interconnection theory between resonance and excitability. Such a theory would also furnish an architecture to implement control algorithms based on impulses and resonance, two concepts often used when design legged robots.

The auditory systems is another source of applications to study interconnections of the two classes of systems considered in this thesis. The interplay between mechanical and electrical phenomena observed in the cochlea [77, Ch.13] makes it a perfect ground to study the interaction between frequency responses and excitable behaviours.

Overall, resonance and excitability account for a variety of oscillatory phenomena encountered in engineering applications. Our hope is that this thesis will contribute to asses the value of an interconnection approach to both analysis and design of these applications, opening the way to a systems and control theory of non-equilibrium dynamics.

Appendix

6.A Detached resonance curves in one-degree-of-freedom systems

This appendix shows how the relation between damping and DRCs noticed in [36] can be formally derived using averaging and singularity theory. The result does not improve on the developments of [36] but it illustrates how singularity theory can lead to constructive principles.

We consider a weakly-nonlinear one-degree-of-freedom system (in Hamiltonian form)

$$\begin{aligned} \dot{q} &= \frac{\partial H}{\partial p} \\ \dot{p} &= -\frac{\partial H}{\partial q} - \varepsilon \left(F(q,p)p - 2f\cos(\phi) \right) \\ \dot{\phi} &= 1 + \varepsilon\beta \end{aligned} \tag{6.1}$$

where $H = \frac{1}{2}(q^2 + p^2) + \varepsilon H_1(q)$ is the energy. Passing to action-angle coordinates

$$\begin{aligned} I = \frac{1}{2}(q^2+p^2), \qquad \theta = \operatorname{atan}\left(\frac{p}{q}\right) \\ q = \sqrt{2I}\cos(\theta), \qquad p = \sqrt{2I}\sin(\theta) \\ \psi = \theta + \phi \\ R(I,\theta) = F\left(\sqrt{2I}\cos(\theta), \sqrt{2I}\sin(\theta)\right)\sqrt{2I}\sin(\theta) \end{aligned} \tag{6.2}$$

and averaging the resulting equations [85] leads to

$$\begin{aligned} \dot{I} &= -\varepsilon\sqrt{2I}(G_1(I) - f\sin(\psi)) \\ \dot{\psi} &= \varepsilon\left(\beta - \frac{\partial \bar{H}_1}{\partial I} - \frac{1}{\sqrt{2I}}\left(G_2(I) - f\cos(\psi)\right)\right) \\ \dot{\phi} &= 1 + \varepsilon\beta \end{aligned} \tag{6.3}$$

Each term in (6.3) is an average:

i) Conservative terms

$$\frac{1}{2\pi}\int_0^{2\pi}\frac{\partial H_1}{\partial I}(I,\psi-\phi)\,d\phi=\frac{1}{2\pi}\frac{\partial}{\partial I}\int_0^{2\pi}H_1 d\,\theta=\frac{\partial \bar{H}_1}{\partial I} \tag{6.4}$$

where $\bar{H}_1$ is the average of H_1 with respect to θ.

ii) Dissipative terms

$$\begin{aligned}\frac{1}{2\pi}\int_0^{2\pi}\sin(\psi-\phi)R(I,\psi-\phi)\,d\phi&=\frac{1}{2\pi}\int_0^{2\pi}\sin(\theta)R(I,\theta)\,d\theta=:G_1(I)\\ \frac{1}{2\pi}\int_0^{2\pi}\cos(\psi-\phi)R(I,\psi-\phi)\,d\phi&=\frac{1}{2\pi}\int_0^{2\pi}\cos(\theta)R(I,\theta)\,d\theta=:G_2(I)\end{aligned} \tag{6.5}$$

iii) Forcing terms

$$\begin{aligned}\frac{1}{2\pi}\int_0^{2\pi}2f\cos(\phi)\sin(\psi-\phi)\,d\phi&=f\sin(\psi)\\ \frac{1}{2\pi}\int_0^{2\pi}2f\cos(\phi)\cos(\psi-\phi)\,d\phi&=f\cos(\psi)\end{aligned} \tag{6.6}$$

Periodic solutions correspond to fixed points of (6.3)

$$\begin{aligned}G_1(I)&=f\sin(\psi)\\ G_2(I)+\sqrt{2I}\left(\frac{\partial \bar{H}_1}{\partial I}-\beta\right)&=f\cos(\psi)\end{aligned} \tag{6.7}$$

Squaring and summing we remove dependence from ψ and obtain

$$g(I,\beta,f)=G_1(I)^2+\left(G_2(I)+\sqrt{2I}\left(\frac{\partial \bar{H}_1}{\partial I}-\beta\right)\right)^2-f^2=0 \tag{6.8}$$

Imposing the conditions for isola/simple bifurcation we get

$$\begin{aligned}\frac{\partial g}{\partial \beta}&=-2\left(G_2(I)+\sqrt{2I}\left(\frac{\partial \bar{H}_1}{\partial I}-\beta\right)\right)\sqrt{2I}=0\\ \frac{\partial g}{\partial I}&=2G_1(I)\frac{dG_1(I)}{dI}+2\left(G_2(I)+\sqrt{2I}\left(\frac{\partial \bar{H}_1}{\partial I}-\beta\right)\right)(...)=0\end{aligned} \tag{6.9}$$

The term (...) has been omitted as it does not influence the result: Solving the first equation gives

$$\beta=\frac{\partial \bar{H}_1}{\partial I}+\frac{G_2(I)}{\sqrt{2I}} \tag{6.10}$$

and leaves for the second one

$$G_1(I)\frac{dG_1(I)}{dI} = 0 \tag{6.11}$$

This equation contains part of the geometrical interpretation obtained through energy balance in [36], indeed $G_1(I)$ corresponds to the averaged damping in that work and we have that isolas and simple bifurcations correspond to zeros and stationary points of $G_1(I)$.

To differentiate between isola and simple bifurcation we need to compute the determinant of the Hessian matrix obtained from (6.8). The computation in the general case can be carried out with a computer algebra system (in this case Sympy [69]). Despite the length of the full expressions, the determinant of the Hessian evaluated at $\beta = \frac{\partial \bar{H}}{\partial I} + \frac{G_2(I)}{\sqrt{2I}}$ has a surprisingly simple expression:

$$\det(d^2 g) = 8I\left(\left(\frac{dG_1(I)}{dI}\right)^2 + G_1(I)\frac{d^2G_1(I)}{dI^2}\right) \tag{6.12}$$

Recall that if $\det(d^2 g) > 0$ the singularity is an isola, while $\det(d^2 g) < 0$ corresponds to simple bifurcations. Since $I > 0$, assuming $\det(d^2 g) \neq 0$ (singularity is not more degenerate than isola or simple bifurcation) we obtain the following:

- If the singularity is due to zero crossing ($G_1 = 0$) then $\det(d^2 g) > 0$ and we always have isolas.
- If the singularity is due to a stationary point ($dG_1/dI = 0$) and the averaged damping is positive then a maximum ($d^2G_1/dI^2 < 0$) corresponds to a simple bifurcation and minimum ($d^2G_1/dI^2 > 0$) to an isola.
- If the singularity is due to a stationary point ($dG_1/dI = 0$) and the averaged damping is negative the situation is the opposite than the previous point.

This characterisation slightly generalises the geometrical interpretation of DRCs presented in [36]. It also illustrates how starting from the descriptive characterisation of a phenomenon through singularity theory it is possible to arrive to constructive principles for the generation of that phenomenon.

References

[1] Abbott, L. F. and Kepler, T. B. (1990). Model neurons: From Hodgkin-Huxley to hopfield. In Garrido, L., editor, *Statistical Mechanics of Neural Networks*, volume 368, pages 5–18. Springer Berlin Heidelberg, Berlin, Heidelberg.

[2] Aman, M., Sporer, M. E., Gstoettner, C., Prahm, C., Hofer, C., Mayr, W., Farina, D., and Aszmann, O. C. (2019). Bionic hand as artificial organ: Current status and future perspectives. *Artificial Organs*, 43(2):109–118.

[3] Balakotaiah, V. and Luss, D. (1981). Analysis of the multiplicity patterns of a CSTR. *Chemical Engineering Communications*, 13(1-3):111–132.

[4] Balakotaiah, V. and Luss, D. (1984). Global analysis of the multiplicity features of multi-reaction lumped-parameter systems. *Chemical Engineering Science*, 39(5):865–881.

[5] Brennan, M. J. and Kovacic, I. (2011). Examples of Physical Systems Described by the Duffing Equation. In Kovacic, I. and Brennan, M. J., editors, *The Duffing Equation*, pages 25–53. John Wiley & Sons, Ltd, Chichester, UK.

[6] Brette, R. and Gerstner, W. (2005). Adaptive exponential integrate-and-fire model as an effective description of neuronal activity. *Journal of Neurophysiology*, 94(5):3637–3642.

[7] Buschmann, T. and Trimmer, B. (2017). Bio-inspired Robot Locomotion. In Hooper, S. L. and Büschges, A., editors, *Neurobiology of Motor Control: Fundamental Concepts and New Directions*, pages 443–472. John Wiley & Sons, Inc., Hoboken, NJ, USA.

[8] Cirillo, G. I., Habib, G., Kerschen, G., and Sepulchre, R. (2017). Analysis and design of nonlinear resonances via singularity theory. *Journal of Sound and Vibration*, 392:295–306. arXiv: 1606.04077.

[9] Cirillo, G. I. and Sepulchre, R. (2019). The Geometry of Rest-Spike Bistability. *arXiv:1904.12161 [math, q-bio]*. arXiv: 1904.12161.

[10] Coombes, S. and Bressloff, P. C., editors (2005). *Bursting: the genesis of rhythm in the nervous system*. World Scientific Pub, Hackensack, NJ. OCLC: ocm61130877.

[11] Craighead, H. G. (2000). Nanoelectromechanical Systems. *Science*, 290(5496):1532–1535.

[12] Den Hartog, J. P. (1985). *Mechanical vibrations*. Dover books on engineering. Dover Publications, New York.

[13] Desroches, M., Fernández-García, S., Krupa, M., Prohens, R., and Teruel, A. E. (2018). Piecewise-Linear (PWL) Canard Dynamics: Simplifying Singular Perturbation Theory in the Canard Regime Using Piecewise-linear Systems. In Carmona, V., Cuevas-Maraver, J., Fernández-Sánchez, F., and García-Medina, E., editors, *Nonlinear Systems, Vol. 1*, pages 67–86. Springer International Publishing, Cham.

[14] Desroches, M. and Jeffrey, M. R. (2011). Canards and curvature: the 'smallness of ε ' in slow–fast dynamics. *Proceedings of the Royal Society A: Mathematical, Physical and Engineering Sciences*, 467(2132):2404–2421.

[15] Detroux, T., Habib, G., Masset, L., and Kerschen, G. (2015). Performance, robustness and sensitivity analysis of the nonlinear tuned vibration absorber. *Mechanical Systems and Signal Processing*, 60-61:799–809.

[16] Doedel, E. J., Oldeman, B. E., Champneys, A. R., Dercole, F., Fairgrieve, T. F., Kuznetsov, Y., Paffenroth, R. C., Sandstede, B., Wang, X. J., and Zhang, C. H. (2007). AUTO-07p: Continuation and bifurcation software for ordinary differential equations. Technical report.

[17] Doiron, B., Laing, C., Longtin, A., and Maler, L. (2002). Ghostbursting: A Novel Neuronal Burst Mechanism. *Journal of Computational Neuroscience*, 12(1):5–25.

[18] Drion, G., Franci, A., Dethier, J., and Sepulchre, R. (2015). Dynamic Input Conductances Shape Neuronal Spiking. *eNeuro*, 2(1):ENEURO.0031–14.2015.

[19] Drion, G., Franci, A., Seutin, V., and Sepulchre, R. (2012). A Novel Phase Portrait for Neuronal Excitability. *PLoS ONE*, 7(8):e41806.

[20] Duffing, G. (1918). *Forced oscillations with variable natural frequency and their technical significance (Erzwungene schwingungen bei veränderlicher eigenfrequenz und ihre technische bedeutung)*. Number 41/42 in Sammlung Vieweg. Braunschweig, F. Vieweg & Sohn,.

[21] Ermentrout, B. and Terman, D. H. (2010). *Mathematical Foundations of Neuroscience*. Number 35 in Interdisciplinary applied mathematics. Springer New York, New York.

[22] Fenichel, N. (1979). Geometric singular perturbation theory for ordinary differential equations. *Journal of Differential Equations*, 31(1):53–98.

[23] Fernández-García, S., Krupa, M., and Clément, F. (2016). Mixed-Mode Oscillations in a piecewise linear system with multiple time scale coupling. *Physica D: Nonlinear Phenomena*, 332:9–22.

[24] Filippov, A. F. (1988). *Differential Equations with Discontinuous Righthand Sides*. Springer Netherlands.

[25] FitzHugh, R. (1961). Impulses and Physiological States in Theoretical Models of Nerve Membrane. *Biophysical Journal*, 1(6):445–466.

[26] Forni, F. and Sepulchre, R. (2016). Differentially Positive Systems. *IEEE Transactions on Automatic Control*, 61(2):346–359.

[27] Forni, F. and Sepulchre, R. (2019). Differential Dissipativity Theory for Dominance Analysis. *IEEE Transactions on Automatic Control*, 64(6):2340–2351.

[28] Frahm, H. (1911). Device for damping vibrations of bodies.

[29] Franci, A., Drion, G., and Sepulchre, R. (2012). An Organizing Center in a Planar Model of Neuronal Excitability. *SIAM Journal on Applied Dynamical Systems*, 11(4):1698–1722.

[30] Franci, A., Drion, G., and Sepulchre, R. (2014). Modeling the Modulation of Neuronal Bursting: A Singularity Theory Approach. *SIAM Journal on Applied Dynamical Systems*, 13(2):798–829.

[31] Franci, A., Drion, G., and Sepulchre, R. (2018). Robust and tunable bursting requires slow positive feedback. *Journal of Neurophysiology*, 119(3):1222–1234.

[32] Franci, A., Drion, G., Seutin, V., and Sepulchre, R. (2013). A Balance Equation Determines a Switch in Neuronal Excitability. *PLoS Computational Biology*, 9(5):e1003040.

[33] Golubitsky, M. and Schaeffer, D. G. (1985). *Singularities and groups in bifurcation theory: Volume I.* Number 51 in Applied Mathematical Sciences. Springer New York, New York, NY.

[34] Govaerts, W. J. F. (2000). *Numerical Methods for Bifurcations of Dynamical Equilibria.* Society for Industrial & Applied Mathematics (SIAM), Philadelphia, PA.

[35] Grenat, C., Baguet, S., Lamarque, C. H., and Dufour, R. (2019). A multi-parametric recursive continuation method for nonlinear dynamical systems. *Mechanical Systems and Signal Processing*, 127:276–289.

[36] Habib, G., Cirillo, G. I., and Kerschen, G. (2018). Isolated resonances and nonlinear damping. *Nonlinear Dynamics*, 93(3):979–994.

[37] Habib, G., Detroux, T., Viguié, R., and Kerschen, G. (2015). Nonlinear generalization of Den Hartog's equal-peak method. *Mechanical Systems and Signal Processing*, 52-53:17–28.

[38] Habib, G. and Kerschen, G. (2015). Suppression of limit cycle oscillations using the nonlinear tuned vibration absorber. *Proceedings of the Royal Society A: Mathematical, Physical and Engineering Sciences*, 471(2176):20140976.

[39] Habib, G. and Kerschen, G. (2016). A principle of similarity for nonlinear vibration absorbers. *Physica D: Nonlinear Phenomena*, 332:1–8.

[40] Habib, G., Kerschen, G., and Stepan, G. (2017). Chatter mitigation using the nonlinear tuned vibration absorber. *International Journal of Non-Linear Mechanics*, 91:103–112.

[41] Hayes, M., Kaper, T. J., Kopell, N., and Ono, K. (1998). On the Application of Geometric Singular Perturbation Theory to Some Classical Two Point Boundary Value Problems. *International Journal of Bifurcation and Chaos*, 08(02):189–209.

[42] Hill, T., Neild, S., and Wagg, D. (2017). Comparing the direct normal form method with harmonic balance and the method of multiple scales. *Procedia Engineering*, 199:869–874.

[43] Hille, B. (2001). *Ion channels of excitable membranes.* Sinauer Associates Inc., Sunderland, Mass., 3rd edition.

[44] Hindmarsh, J. L. and Rose, R. M. (1982). A model of the nerve impulse using two first-order differential equations. *Nature*, 296(5853):162–164.

[45] Hindmarsh, J. L. and Rose, R. M. (1984). A model of neuronal bursting using three coupled first order differential equations. *Proceedings of the Royal Society of London. Series B. Biological Sciences*, 221(1222):87–102.

[46] Hodgkin, A. L. and Huxley, A. F. (1952). A quantitative description of membrane current and its application to conduction and excitation in nerve. *The Journal of Physiology*, 117(4):500–544.

[47] Holmes, P. and Rand, D. (1976). The bifurcations of duffing's equation: An application of catastrophe theory. *Journal of Sound and Vibration*, 44(2):237–253.

[48] Iwasaki, T. (2008). Multivariable harmonic balance for central pattern generators. *Automatica*, 44(12):3061–3069.

[49] Izhikevich, E. M. (2000). Neural excitability, spiking and bursting. *International Journal of Bifurcation and Chaos*, 10(06):1171–1266.

[50] Izhikevich, E. M. (2006). Bursting. *Scholarpedia*, 1(3):1300.

[51] Izhikevich, E. M. (2007). *Dynamical systems in neuroscience: the geometry of excitability and bursting*. Computational neuroscience. MIT Press, Cambridge, Mass.

[52] Johnston, D. and Wu, S. M.-s. (1995). *Foundations of cellular neurophysiology*. MIT Press, Cambridge, Mass.

[53] Jones, E., Oliphant, T., Peterson, P., and others (2001). SciPy: open source scientific tools for Python.

[54] Kepler, T. B., Abbott, L. F., and Marder, E. (1992). Reduction of conductance-based neuron models. *Biological Cybernetics*, 66(5):381–387.

[55] Kerschen, G., Kowtko, J. J., Mcfarland, D. M., Bergman, L. A., and Vakakis, A. F. (2007). Theoretical and Experimental Study of Multimodal Targeted Energy Transfer in a System of Coupled Oscillators. *Nonlinear Dynamics*, 47(1):285–309.

[56] Keyfitz, B. L. (1986). Classification of one-state-variable bifurcation problems up to codimension seven. *Dynamics and Stability of Systems*, 1(1):1–41.

[57] Koch, C. (1999). *Biophysics of computation: information processing in single neurons*. Computational neuroscience. Oxford University Press, New York.

[58] Kokotović, P. and Arcak, M. (2001). Constructive nonlinear control: a historical perspective. *Automatica*, 37(5):637–662.

[59] Kokotović, P., Khalil, H. K., and O'Reilly, J. (1999). *Singular Perturbation Methods in Control: Analysis and Design*. Classics in applied mathematics. Society for Industrial and Applied Mathematics (SIAM), Philadelphia, PA.

[60] Kovacic, I. and Brennan, M. J. (2011). Background: On Georg Duffing and the Duffing Equation. In Kovacic, I. and Brennan, M. J., editors, *The Duffing Equation*, pages 1–23. John Wiley & Sons, Ltd, Chichester, UK.

[61] Krupa, M. and Szmolyan, P. (2001). Relaxation Oscillation and Canard Explosion. *Journal of Differential Equations*, 174(2):312–368.

[62] Krupa, M. and Wechselberger, M. (2010). Local analysis near a folded saddle-node singularity. *Journal of Differential Equations*, 248(12):2841–2888.

[63] Kuehn, C. (2014). *Multiple time scale dynamics*. Springer, New York.

[64] Lifshitz, R. and Cross, M. C. (2010). Nonlinear Dynamics of Nanomechanical and Micromechanical Resonators. In *Reviews of Nonlinear Dynamics and Complexity*, pages 1–52. Wiley-Blackwell.

[65] Loomis, L. H. and Sternberg, S. (2013). *Advanced Calculus*. World Scientific.

[66] Marder, E., O'Leary, T., and Shruti, S. (2014). Neuromodulation of Circuits with Variable Parameters: Single Neurons and Small Circuits Reveal Principles of State-Dependent and Robust Neuromodulation. *Annual Review of Neuroscience*, 37(1):329–346.

[67] Mauro, A., Conti, F., Dodge, F., and Schor, R. (1970). Subthreshold Behavior and Phenomenological Impedance of the Squid Giant Axon. *The Journal of General Physiology*, 55(4):497–523.

[68] McKean, H. P. (1970). Nagumo's equation. *Advances in Mathematics*, 4(3):209–223.

[69] Meurer, A., Smith, C. P., Paprocki, M., Čertík, O., Kirpichev, S. B., Rocklin, M., Kumar, A., Ivanov, S., Moore, J. K., Singh, S., Rathnayake, T., Vig, S., Granger, B. E., Muller, R. P., Bonazzi, F., Gupta, H., Vats, S., Johansson, F., Pedregosa, F., Curry, M. J., Terrel, A. R., Roučka, Š., Saboo, A., Fernando, I., Kulal, S., Cimrman, R., and Scopatz, A. (2017). SymPy: symbolic computing in Python. *PeerJ Computer Science*, 3:e103.

[70] Morris, C. and Lecar, H. (1981). Voltage oscillations in the barnacle giant muscle fiber. *Biophysical Journal*, 35(1):193–213.

[71] Nagumo, J., Arimoto, S., and Yoshizawa, S. (1962). An Active Pulse Transmission Line Simulating Nerve Axon. *Proceedings of the IRE*, 50(10):2061–2070.

[72] Peeters, M., Viguié, R., Sérandour, G., Kerschen, G., and Golinval, J. C. (2009). Nonlinear normal modes, Part II: Toward a practical computation using numerical continuation techniques. *Mechanical Systems and Signal Processing*, 23(1):195–216.

[73] Pinsky, P. F. and Rinzel, J. (1994). Intrinsic and network rhythmogenesis in a reduced Traub model for CA3 neurons. *Journal of Computational Neuroscience*, 1(1-2):39–60.

[74] Plant, R. E. (1981). Bifurcation and resonance in a model for bursting nerve cells. *Journal of Mathematical Biology*, 11(1):15–32.

[75] Pontryagin, L. S. and Rodygin, L. V. (1960). Approximate solution of a system of ordinary differential equations involving a small parameter in the derivatives. *Doklady Akademii Nauk SSSR*, 131(2):255–258.

[76] Prohens, R., Teruel, A., and Vich, C. (2016). Slow–fast n-dimensional piecewise linear differential systems. *Journal of Differential Equations*, 260(2):1865–1892.

[77] Purves, D., editor (2019). *Neuroscience*. Oxford University Press, New York Oxford, sixth international edition edition.

[78] Rhoads, J. F., Shaw, S. W., and Turner, K. L. (2010). Nonlinear Dynamics and Its Applications in Micro- and Nanoresonators. *Journal of Dynamic Systems, Measurement, and Control*, 132(3).

[79] Ribar, L. and Sepulchre, R. (2019). Neuromodulation of Neuromorphic Circuits. *IEEE Transactions on Circuits and Systems I: Regular Papers*, 66(8):3028–3040.

[80] Rinzel, J. (1896). A formal classification of bursting mechanisms in excitable systems. In *Proceedings of the International Congress of Mathematicians*, Berkley.

[81] Rinzel, J. (1985a). Bursting oscillations in an excitable membrane model. In Sleeman, B. D. and Jarvis, R. J., editors, *Ordinary and Partial Differential Equations*, number 1151, pages 304–316. Springer Berlin Heidelberg, Berlin, Heidelberg.

[82] Rinzel, J. (1985b). Excitation dynamics: insights from simplified membrane models. In *Federation Proceedings*, volume 44, pages 2944–2946.

[83] Rinzel, J. and Lee, Y. S. (1987). Dissection of a model for neuronal parabolic bursting. *Journal of Mathematical Biology*, 25(6):653–675.

[84] Rotstein, H. G., Coombes, S., and Gheorghe, A. M. (2012). Canard-Like Explosion of Limit Cycles in Two-Dimensional Piecewise-Linear Models of FitzHugh–Nagumo Type. *SIAM Journal on Applied Dynamical Systems*, 11(1):135–180.

[85] Sanders, J. A., Verhulst, F., and Murdock, J. A. (2007). *Averaging methods in nonlinear dynamical systems*. Number 59 in Applied mathematical sciences. Springer, New York, 2nd ed edition.

[86] Sieling, F. H. and Butera, R. (2011). Aplysia R15 neuron. *Scholarpedia*, 6(10):4181.

[87] Smith, G. D., Cox, C. L., Sherman, S. M., and Rinzel, J. (2000). Fourier Analysis of Sinusoidally Driven Thalamocortical Relay Neurons and a Minimal Integrate-and-Fire-or-Burst Model. *Journal of Neurophysiology*, 83(1):588–610.

[88] Soto-Treviño, C., Rabbah, P., Marder, E., and Nadim, F. (2005). Computational Model of Electrically Coupled, Intrinsically Distinct Pacemaker Neurons. *Journal of Neurophysiology*, 94(1):590–604.

[89] Strutt, Baron Rayleigh, J. W. (1877). *The theory of Sound*.

[90] Szmolyan, P. (1991). Transversal heteroclinic and homoclinic orbits in singular perturbation problems. *Journal of Differential Equations*, 92(2):252–281.

[91] Szmolyan, P. and Wechselberger, M. (2001). Canards in R^3. *Journal of Differential Equations*, 177(2):419–453.

[92] Szmolyan, P. and Wechselberger, M. (2004). Relaxation oscillations in R^3. *Journal of Differential Equations*, 200(1):69–104.

[93] Traub, R. D. (1982). Simulation of intrinsic bursting in CA3 hippocampal neurons. *Neuroscience*, 7(5):1233–1242.

[94] Traub, R. D., Wong, R. K., Miles, R., and Michelson, H. (1991). A model of a CA3 hippocampal pyramidal neuron incorporating voltage-clamp data on intrinsic conductances. *Journal of Neurophysiology*, 66(2):635–650.

[95] Vakakis, A. F., Gendelman, O. V., Bergman, L. A., McFarland, D. M., Kerschen, G., and Lee, Y. S. (2009). *Nonlinear Targeted Energy Transfer in Mechanical and Structural Systems*. Number 156 in Solid Mechanics and Its Applications. Springer Netherlands, Dordrecht.

[96] van der Pol, B. (1926). LXXXVIII. On "relaxation-oscillations". *The London, Edinburgh, and Dublin Philosophical Magazine and Journal of Science*, 2(11):978–992.

[97] van der Pol, B. and van der Mark, J. (1928). LXXII. The heartbeat considered as a relaxation oscillation, and an electrical model of the heart. *The London, Edinburgh, and Dublin Philosophical Magazine and Journal of Science*, 6(38):763–775.

[98] Van Pottelbergh, T., Drion, G., and Sepulchre, R. (2018). Robust Modulation of Integrate-and-Fire Models. *Neural Computation*, 30(4):987–1011.

[99] von Helmholtz, H. L. F. (1863). *On the sensations of tone as a physiological basis for the theory of music.*

[100] Wang, X.-J. and Rinzel, J. (2003). Oscillatory and bursting properties of neurons. In Arbib, M., editor, *Handbook of brain theory and neural networks*, pages 686–691. MIT Press, 2nd edition.

[101] Wechselberger, M., Mitry, J., and Rinzel, J. (2013). Canard Theory and Excitability. In Kloeden, P. E. and Pötzsche, C., editors, *Nonautonomous Dynamical Systems in the Life Sciences*, Lecture Notes in Mathematics, pages 89–132. Springer International Publishing, Cham.

[102] Wiser, J. and Golubitsky, M. (2015). Bifurcations in Forced Response Curves. *SIAM Journal on Applied Dynamical Systems*, 14(4):2013–2029.

[103] Yadi, K. (2014). Averaging on slow and fast cycles of a three time scale system. *Journal of Mathematical Analysis and Applications*, 413(2):976–998.

[104] Zeeman, E. C. (1973). Differential Equations for the Heartbeat and Nerve Impulse. In Waddington, C. H., editor, *Towards a Theoretical Biology*, number 4, pages 8–67. Edinburgh University Press, Aldine-Atherton, Chicago.

[105] Zhang, Y. and Golubitsky, M. (2011). Periodically Forced Hopf Bifurcation. *SIAM Journal on Applied Dynamical Systems*, 10(4):1272–1306.